UNIVERSITY OF CALIFORNIA SAN DIEGO

Silicon-rich nitride as a highly nonlinear and reconfigurable photonic integrated platform for efficient on-chip applications.

A Dissertation submitted in partial satisfaction of the requirements for the degree Doctor of Philosophy

in

Electrical Engineering (Photonics)

by

Dmitrii Belogolovskii

Committee in charge:

Yeshaiahu Fainman, chair
Nikola Alic
Prabhakar Bandaru
Zhaowei Liu
Yu-Hwa Lo
Abdoulaye Ndao

2024

The Dissertation of Dmitrii Belogolovskii is approved, and it is acceptable in quality and form for publication on microfilm and electronically.

University of California San Diego

2024

TABLE OF CONTENTS

LIST OF FIGURES

SECTION 1

SECTION 2

LIST OF TABLES

SECTION 1

SECTION 2

SECTION 3

ACKNOWLEDGEMENTS

I thank my advisors Prof. Fainman and Prof. Ndao, for providing an opportunity to pursue research in the field of integrated photonics, and guidance throughout the process. I would also like to express my gratitude towards Dr. Alic for mentoring, guidance and providing equipment crucial for my research. I thank all the members of my committee, and our research group, for their assistance.

Chapter 1, in part, is a reprint of the material published in Advanced Photonics Research. The dissertation author was first author of this paper, with co-authors Nikola Alic, Andrew Grieco, and Yeshaiahu Fainman.

Chapter 2, in part, is a reprint of the material published in Advanced Optical Materials. The dissertation author was the first author of this paper, with co-authors Yeshaiahu Fainman, Andrew Grieco, and Nikola Alic.

Chapter 3, in part is currently in submission to a peer-reviewed journal. The dissertation author was the first author of this paper, with co-authors Md Masudur Rahman, Karl Johnson, Vladimir Fedorov, Nikola Alic, Abdoulaye Ndao, Paul K. L. Yu, and Yeshaiahu Fainman.

VITA

2017 Bachelor of Science, Moscow Institute of Physics and Technology (State University), Applied Mathematics and Physics (Department of Physical and Quantum Electronics)

2019 Master of Science, Moscow Institute of Physics and Technology (State University), Phystech-school of electronics, photonics and molecular physics (Photonics Division)

2024 Doctor of Philosophy, University of California San Diego, Electrical Engineering (Photonics)

PUBLICATIONS

- **Belogolovskii, D.**, Rahman, M. M., Johnson, K., Fedorov, V., Alic, N., Ndao, A., Yu, P. K. L. & Fainman, Y. Large bidirectional refractive index change in silicon-rich nitride via visible light trimming (2024), *in submission*.

- **Belogolovskii, D.**, Fainman, Y. & Alic, N. Dynamics of Nonlinear Optical Losses in Silicon-Rich Nitride Nano-Waveguides. Adv. Optical Mater. 12, 2401299 (2024).

- **Belogolovskii, D.**, Alic, N., Grieco, A. & Fainman, Y. Silicon-Rich Nitride Refractive Index as a Degree of Freedom to Maximize Nonlinear Wave Mixing in Nanowaveguides. Adv. Photonics Res. 5, 2400017 (2024).

- Friedman, A., **Belogolovskii, D.**, Grieco, A. & Fainman, Y. Optical bistability in PECVD silicon-rich nitride. Opt. Express 30, 45340–45349 (2022).

- Jiang, S., **Belogolovskii, D.**, Deka, S. S., Pan, S. H. & Fainman, Y. Experimental demonstration of mode selection in bridge-coupled metallo-dielectric nanolasers. Opt. Lett. 46, 6027–6030 (2021).

- Fainman, Y., Yang, M., Gao, C., Lin, H. H., Friedman, A. & **Belogolovskii, D.** Nonlinear optical properties of inhomogeneous thin films. Proc. SPIE PC12228, Ultrafast Nonlinear Imaging and Spectroscopy X PC122280I (2022).

- Jiang, S., **Belogolovskii, D.**, Deka, S. S., Pan, S. H. & Fainman, Y. Experimental demonstration of mode selection in metallo-dielectric nanolasers coupled via a bridge. In Conference on Lasers and Electro-Optics, Technical Digest Series (Optica Publishing Group, 2022), paper STu4E.2.

- Friedman, A., **Belogolovskii, D.**, Grieco, A. & Fainman, Y. A systematic evaluation of Silicon-rich Nitride Electro-optic Modulator design and tradeoffs. arXiv (2023).

ABSTRACT OF THE DISSERTATION

Silicon-rich nitride as a highly nonlinear and reconfigurable photonic integrated platform for efficient on-chip applications.

by

Dmitrii Belogolovskii

Doctor of Philosophy in Electrical Engineering (Photonics)

University of California San Diego, 2024

Professor Yeshaiahu Fainman, Chair

Silicon nitride (Si_xN_y) fabricated via plasma-enhanced chemical vapor deposition (PECVD) has emerged as a highly promising platform for CMOS-compatible integrated photonics. The stoichiometric form, Si_3N_4, offers key advantages such as ultra-low optical losses (< 1 dB/cm), a wide optical transparency range, and the absence of two-photon absorption (TPA) in the telecommunication spectral band. These characteristics make Si_3N_4 highly suitable for applications requiring high optical power, including broadband nonlinear wave mixers, modulators, and optical switches. Additionally, Si_3N_4 has a high optical damage threshold, enabling efficient nonlinear optical devices. Despite being an amorphous material, Si_3N_4 also exhibits second-order nonlinear effects.

However, Si_3N_4 has its own limitations, including a low third-order nonlinear susceptibility, a small refractive index contrast with the SiO_2 cladding, and a larger effective mode area, which collectively reduce the efficiency of nonlinear wave mixing. To address these limitations, silicon-rich nitride (SRN), achieved by increasing silicon concentration, has been explored as a material with enhanced nonlinearities. SRN has enabled efficient demonstrations of nonlinear processes such as FWM, supercontinuum generation, intermodal frequency generation, and the strong DC Kerr effect.

This thesis explores the impact of the SRN refractive index on key waveguide parameters, including optical nonlinearities, linear and nonlinear losses, and mode confinement. Our findings reveal a trade-off: increasing the refractive index enhances optical nonlinearities but also raises optical losses. Notably, we demonstrate that nonlinear losses become the primary limitation for four-wave mixing (FWM) efficiency at high optical power when the SRN refractive index exceeds 3. We identify free carrier absorption (FCA) as the dominant source of nonlinear losses and show that its dynamics are strongly influenced by the refractive index of SRN.

Furthermore, we demonstrate significant bidirectional optical trimming of the SRN refractive index using visible light. This ability to precisely tune the refractive index is crucial for phase-sensitive devices, such as demultiplexers, as highlighted in this thesis. These findings establish SRN as a highly reconfigurable and versatile platform for photonic applications.

INTRODUCTION

This section provides an overview of the key findings of this thesis, focusing on how the refractive index of SRN influences nonlinearities, linear and nonlinear losses, FWM efficiency, FCA relaxation and recombination times, as well as its bidirectional trimming capability.

We have explored SRN to find the best recipe for various optical nonlinear applications such SHG, four wave mixing, electric field induced second harmonic (EFISH) generation and electro-optic modulation. Specifically, FWM is implemented in over a hundred SRN waveguides prepared by plasma-enhanced chemical vapor deposition PECVD in a wide range of SRN refractive indices varying between 2.5 and 3.2 (measured in the C-band). It is determined that SRN with a refractive index of about 3 maximizes the FWM efficiency for continuous-wave operation, indicating that the refractive index of SRN is indeed a crucial optimization parameter for nonlinear optics applications. The FWM efficiency is limited by large nonlinear optical losses observed in SRN waveguides with indices larger than 2.7, which are not related to two photon absorption. Finally, the third order susceptibility χ_3 and the nonlinear refractive index n_2 are estimated for multiple SRN refractive indices, and, specifically, the nonlinearities as large as $\chi_3 = (12.6 \pm 1.4) \times 10^{-19}$ m^2/V^2 and $n_2 = (7.6 \pm 0.8) \times 10^{-17}$ m^2/W are estimated in a waveguide with an SRN refractive index of 3.2.

In addition, free carrier absorption (FCA) is established to be the cause of nonlinear losses in plasma-enhanced chemical vapor deposition (PECVD) silicon-rich nitride (SRN) waveguides. To validate this hypothesis, a photo-induced current is measured in SRN thin films with refractive indices varying between 2.5 to 3.15 when a C-band laser light is illuminating the SRN films at various powers, indicating the generation of free carriers. Furthermore, nonlinear loss dynamics is, for the first time, measured and characterized in detail in SRN waveguides by utilizing high peak power C-band complex shape optical pulses for estimation of free carrier generation (FCG) and free carrier recombination (FCR) lifetimes and their dynamics. Both FCG and FCR are found to decrease with an increase in the refractive index of SRN, and, specifically, the FCR lifetimes are found (92±7) ns, (39±3) ns, and (31±2) ns for the SRN indices of

2.7, 3 and 3.15, respectively. Lastly, nonlinear losses in high refractive index SRN waveguides are demonstrated to be minimized and altogether avoided when the pulse duration reduced below the free carrier generation lifetime, thus providing a way of taking a full advantage of the large inherent SRN nonlinear properties.

Finally, phase-sensitive integrated photonic devices are highly susceptible to minor manufacturing deviations, resulting in significant performance inconsistencies. This variability has limited the scalability and widespread adoption of these technologies. Here, we present a major advancement achieved through visible light (405 nm and 520 nm) trimming of plasma-enhanced chemical vapor deposition (PECVD) silicon-rich nitride (SRN) waveguides. Our method achieves precise, bidirectional refractive index tuning with a single laser source in CMOS-compatible SRN samples with refractive indices of 2.4 and 2.9 (measured at 1550 nm). Utilizing a cost-effective setup for real-time resonance tracking in micro-ring resonators, we attain resonant wavelength shifts as fine as 10 pm. Additionally, we report a record-setting red shift of 49.1 nm and a substantial blue shift of 10.6 nm, corresponding to refractive index changes of approximately 0.11 and -2×10^{-2}. We demonstrate that the origin of both blue and red shifts is thermal annealing. These results highlight SRN's exceptional capability for permanent optical tuning, establishing a foundation for stable, precisely controlled performance in phase-sensitive integrated photonic devices.

In the following we provide details on these three advancements.

CHAPTER 1 - SILICON-RICH NITRIDE REFRACTIVE INDEX AS A DEGREE OF FREEDOM TO MAXIMIZE NONLINEAR WAVE MIXING IN NANOWAVEGUIDES

1. Introduction

Silicon nitride (Si_xN_y) on insulator grown by plasma-enhanced chemical vapor deposition (PECVD) is of great interest as a CMOS-compatible integrated photonics platform. Indeed, the benefits of stoichiometric Si_3N_4 include very low optical losses (< 1 dB/cm) [1, 2, 3], absence of two-photon absorption (TPA) in the telecommunication spectral band [4, 5, 6], and a broad optical transparency window [7]. Furthermore, Si_3N_4 possesses a high optical damage threshold that is well suited for high power applications [8], enabling efficient optical nonlinear devices such as broadband nonlinear wave mixers, optical switches, modulators, and others. Even though the material is amorphous, second-order nonlinear effects have been observed in Si_3N_4 caused by surface nonlinearities due to symmetry breaking of a bulk material [9], bulk nonlinearities [10], and a coherent photogalvanic effect [11]. Unsurprisingly, there has been a growing number of successful demonstrations of Si_3N_4 based nonlinear devices, such as second harmonic generation (SHG) in resonant gratings and ring resonators [12, 13], SHG in an electrically poled waveguide [14], photoinduced SHG due a to photogalvanic effect [15, 16, 17, 18, 19, 20], coherent supercontinuum generation [21], four-wave mixing (FWM) [22], comb generation [23], difference frequency generation (DFG) [24], electric-field poled microresonator modulator [25], and others.

On the other hand, Si_3N_4 has a significant advantage over the c-Si on insulator platform (SOI) in some applications since c-Si suffers from large TPA in the C-band, free carrier absorption (FCA), a smaller transparency window starting at a wavelength of 1.2 μm, and no second order nonlinear susceptibility χ_2 [26]. However, Si_3N_4 has a much lower third order nonlinear susceptibility χ_3 [20, 27], as well as lower refractive index difference between the waveguide core and SiO_2 cladding, resulting in a lower mode waveguide core overlap and larger effective mode area, leading to lower efficiency of nonlinear wave mixing processes. To mitigate these drawbacks, it has been reported that increasing Si concentration in SRN leads to a higher refractive index and the corresponding nonlinearities. Indeed, some efficient SRN nonlinear processes, such as FWM [28], supercontinuum generation [29], intermodal frequency generation

[30], strong DC Kerr effect [31], and many others, have been demonstrated to date. However, in addition to the desirable increase in the nonlinear response, the increase in Si concentration also leads to the increase in optical losses and TPA in SRN [4, 28], which obviously requires a careful material design tradeoff. Notably, a reduction in optical losses has been accomplished by depositing low pressure chemical vapor deposition (LPCVD) SRN instead [1, 2], but it requires much higher temperature of deposition, which makes it incompatible with CMOS processing. An alternative approach is to use the SiD_4 precursor gas instead of SiH_4, which leads to a reduction of optical losses in an SRN waveguide due to absence of Si-H and N-H bonds in C-band, but the SiD_4 gas is not always available [1, 32, 33]. It is also possible to optimize a PECVD recipe by varying high frequency (HF) to lower frequency (LF) RF power ratio to break hydrogen bonds and reduce optical losses [34], but it may also alter other optical parameters. Overall, an SRN refractive index becomes an important degree of freedom for nonlinear mixing device efficiency optimization.

In this paper we experimentally investigate a wide-range (varying between 2.5 and 3.2) SRN refractive index effect on the nonlinear mixing efficiency in the C-band. Furthermore, we use FWM efficiency to retrieve the material χ_3 for each of the SRN samples, as well as to identify the optimal device SRN refractive index in terms of nonlinear efficiency optimization. Specifically, the characterization included the effects of both linear and nonlinear optical losses on the FWM efficiency, which have been determined as a function of waveguide geometry and optical power, respectively. While FWM in SRN waveguides was implemented previously, it was almost universally demonstrated for only a single SRN refractive index in each published study, for different wavelengths or SRN deposition recipes, making the comparison between different results from published studies rather difficult. This work, however, provides a comprehensive rigorous study of the SRN platform in which the samples with widely ranging parameters were fabricated in the same controlled conditions, including the same fabrication flow and equipment, thus allowing a proper systematic comparison between a large number of samples made of SRN films with different refractive indices. Lastly, we also provide a novel report on the observation of nonlinear optical

losses in high index PECVD SRN waveguides not caused by TPA, and how such losses affect the efficiency of FWM at higher power. Thus, the novel results of this study have important design ramifications for researchers working on SRN-based components and devices.

The manuscript is organized as follows: The fundamentals of the underlying theory and methodology are contained in Section 2, samples fabrication and the characterization are described in Section 3, and the experimental results are detailed in Section 4. Finally, the findings and conclusions of this study are summarized and discussed in Section 5.

2. Degenerate FWM Theory

The efficiency of degenerate FWM in a waveguide under the assumption of undepleted pump approximation and absence of nonlinear losses can be described by [35]

$$\mu = \frac{P_i}{P_s} = \left|\gamma P_p L_{eff}\right|^2 \Gamma, \tag{1}$$

where

$$\gamma = \frac{\omega n_2}{c A_{eff}} = \frac{3\omega\chi_3}{4\varepsilon_0 c^2 A_{eff} n_{eff}^2} \tag{2}$$

$$L_{eff}^2 = L^2 \exp(-\alpha L)\left|\frac{1-\exp(-\alpha L - i\Delta k L)}{\alpha L + i\Delta k L}\right|^2 \tag{3}$$

$$\Delta k = 2k_p - k_i - k_s \tag{4}$$

$$k_j = \frac{2\pi n_{eff,j}}{\lambda_j}, j = i, p, s \tag{5}$$

$$\Gamma = \frac{\left|\iint_A \chi_3 E^4 dxdy\right|^2}{\iint_{-\infty}^{+\infty}|\chi_3 E^3|^2 dxdy \iint_{-\infty}^{+\infty}|E|^2 dxdy}, \tag{6}$$

where indices *i*, *p*, *s* represent the idler, pump, and signal, P_j is the optical power, γ is a nonlinear effective coefficient, n_2 is a nonlinear refractive index, ω is the optical frequency of pump, χ_3 is the third

order nonlinear susceptibility, ε_0 is the vacuum permittivity, c is the speed of light, A_{eff} is the effective mode area, n_{eff} is the modal effective index, α is the optical loss coefficient, L is the waveguide length, k_j is the wave vector, k is the mode phase mismatch, λ_j is the wavelength, Γ stands for the modal overlap integral, A represents an SRN integration area limited by the core width and height, E is the mode electric field in the transverse plane. We ignore the SiO_2 cladding contribution to FWM in SRN waveguides since χ_3 of SiO_2 is much smaller than that of SRN used in our study even for the lowest SRN refractive index.

As follows from the FWM efficiency given by Equation (1)-(6), the increase in the mixing efficiency requires some combination of lower optical losses, increase in χ_3 and mode confinement in the waveguide, or, conversely, decrease the effective mode area and dispersion. In waveguides with non-zero dispersion and considerable loss, the FWM efficiency is generally governed by the relevant characteristic lengths: The maximum length due to optical losses $L_{loss} \approx 1/\alpha$, or a coherence length $L_{coh} = \pi/k$. As it will be shown later in the manuscript, in the setup used in our measurements, the losses were the limiting factor, imposing a limit on the devices' length of a few millimeters, while the dispersion set a limit on the scale of centimeters for the chosen wavelengths for the pump, signal and idler. Therefore, in our case the FWM efficiency can be most appropriately expressed as follows:

$$\mu \sim \left(\frac{\chi_3}{\alpha A_{eff} n_{eff}^2} \right)^2, \tag{7}$$

showing the equivalent importance of χ_3 and optical losses. Additionally, we would also like to point out that the reduction in the effective area may be equally important in this respect, which can be achieved in waveguides with a high SRN refractive index.

3. Experimental Design and Sample Fabrication

To facilitate the wide-ranging characterization, over a hundred waveguides were fabricated having four different lengths (0.3, 2.4, 4.4, 6.5 mm), with refractive indices in the range of (2.5 – 3.2) and with varying waveguide widths. To fabricate our samples, we used SOI wafers with a 3 µm buried oxide (BOX) layer and a 220 nm Si device layer, which was removed by TMAH wet etching (note that this step can be

avoided if Si wafers with only a SiO_2 layer on the top are available). Then, an SRN thin film was deposited in a Plasmalab PECVD, with a stage temperature set to 350 °C, while using SiH_4 and N_2 precursor gases. The ratio of gases was varied to change the refractive index of the SRN thin films, as shown in **Figure 1.1**. The thin film thickness and refractive index were measured by a J.A. Woollam M-2000D ellipsometer. Next, the HSQ e-beam resist was spun on the sample, before being patterned by e-beam lithography. After being developed, the sample was etched in a Plasmalab P100, and HSQ was removed by 6:1 BOE. The final step consisted of depositing a SiO_2 cladding in a Plasmalab PECVD. The light coupling in and out of the waveguides was enabled by fully etched linearly apodized grating couplers (GC) with long 300 μm tapers. Coupling efficiency (CE) maximization was enabled by simulations in Ansys (Lumerical), including calculations of GC-optimal parameters such as the filling factor, linear apodization factor, and others [36]. Unlike edge couplers that require dicing, which adds an extra step of fabrication, fully etched GC can be done in one step of e-beam lithography along with waveguides, simplifying the fabrication flow. Additionally, in our practice edge couplers suffered from significant edge roughness caused by dicing in our facility, which led to relatively low CE of -10 dB per edge coupler. Therefore, the Bosch process was necessary to deep etch the edges to make them smoother, which would increase CE, but also would complicate the fabrication flow, which must have been avoided since many samples needed to be fabricated. At the same time, GC were found quite efficient, yielding CE as high as -4.5 dB per GC, while -3 dB was a theoretical maximum due to a symmetry of the fully etched GC. They had a spectral bandwidth of 40 nm, large enough to efficiently couple in and out the pump, signal, and idler with a wavelength gap of 5 nm. We used SM fibers to couple light in and out of a sample as unlike tapered fibers, they can handle higher power without optical damage.

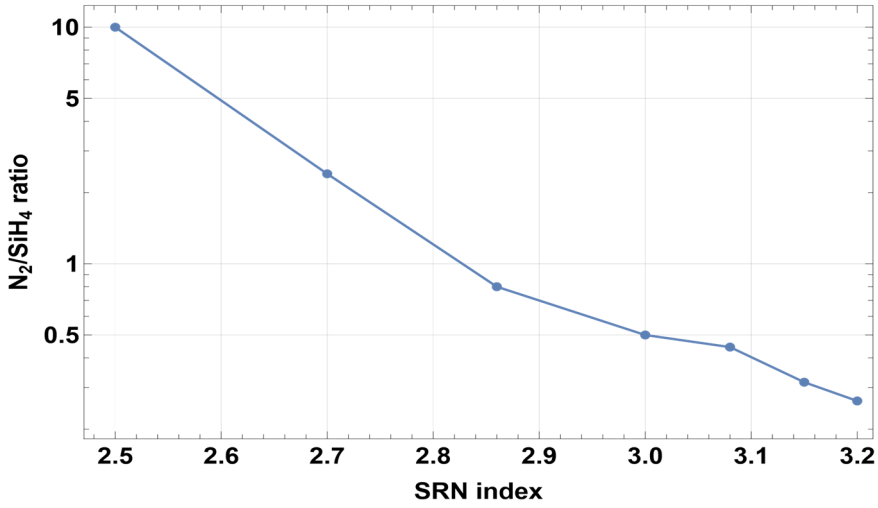

Figure 1.1: N_2/SiH_4 gas ratio utilized to deposit PECVD SRN films with a corresponding refractive index measured at 1550 nm.

To measure the FWM-generated idler, we combined the pump and the signal (both operated in the CW regime) and coupled them to an SRN waveguide, which is shown in **Figure 1.2**(a) as an optical microscope image. A C-band tunable narrowband (~100 kHz) Agilent 81980A laser was used as a signal source, while a tunable narrowband (~100 kHz) Agilent 81642A laser amplified by an IPG Photonics EAD-3C EDFA was used as a pump source. The EDFA noise was removed by a bandpass filter (BF). Polarization controllers (PC) were used to set the waves' polarization to the TE state. The signal and pump were combined through a beam combiner (BC) and coupled to a sample under test. The generated idler together with the residual pump and signal were coupled out and measured by a Yokogawa AQ6375 optical spectrum analyzer (OSA). The setup block diagram is shown in Figure 1.2(b).

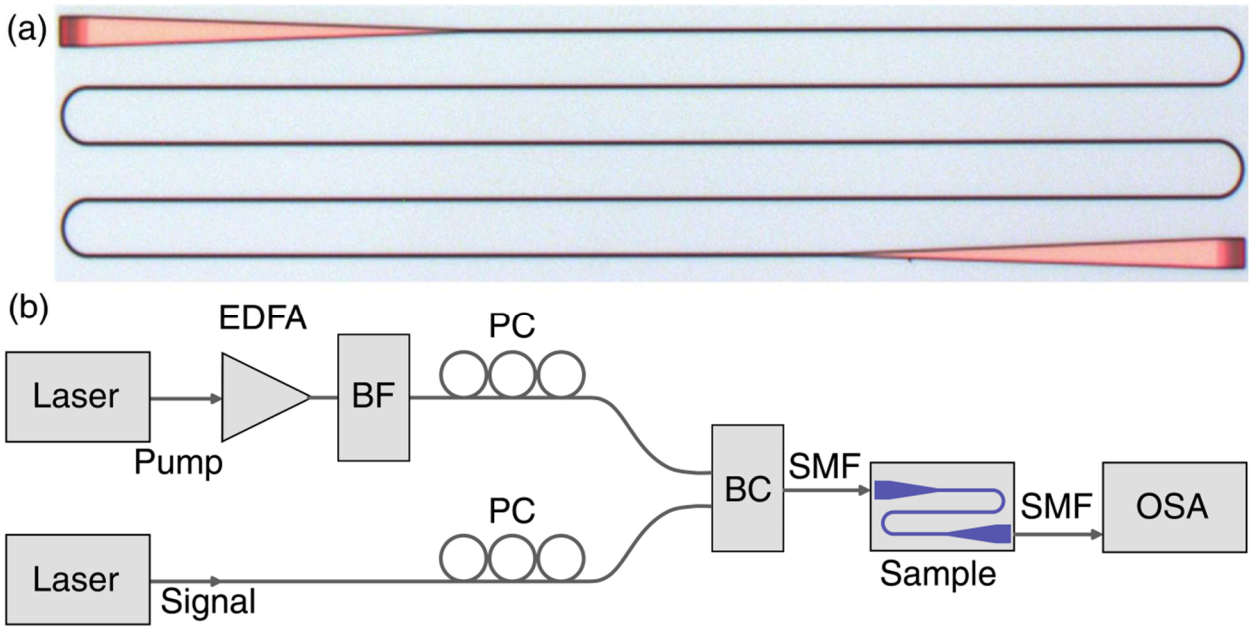

Figure 1.2: (a) Optical microscope image of a typical SRN waveguide fabricated in a serpentine shape for a compact design, (b) block diagram of the experimental apparatus used to perform FWM in SRN waveguides and its characterization. EDFA: Erbium-doped fiber amplifier, BP: Bandpass filter, PC: Polarization controller, BC: 3 dB beam combiner, SMF: Single mode fiber coupler, OSA: Optical spectrum analyzer.

The wavelength difference between the pump and the signal was set to 5 nm, large enough to avoid suppression of the small-power idler by the high-power pump caused by a dynamic range limit of the OSA, while small enough to avoid phase mismatch caused by the dispersion in a long waveguide and fit within the spectral bandwidth of the GC. The negligible level of FWM in the silica patch cords used was independently verified by removing the SRN sample from the setup, whereby, no idler was distinguishable on the OSA above the -67 dBm noise level, matching the theoretical estimation.

A waveguide geometry for all samples was chosen such that each SRN index waveguide remained single mode (SM) to avoid high-order mode interference, while maintaining the mode overlap integral Γ approximately constant (≈0.5) for each SRN sample considered. In particular, to satisfy the latter condition, the thickness of the waveguides was maintained around 350 nm, while the corresponding widths varied from 375 nm (for the index of 3.2), to 550 nm (for the index 2.5). The BOX layer was maintained at 3 µm and the top cladding at 1 µm for all samples. **Table 1.1** summarizes the SRN waveguide parameters simulated in Lumerical (Ansys) for different SRN refractive indices and geometry, where n is the SRN

refractive index, w is the waveguide core width, d is the waveguide core thickness, A_{eff} is the effective mode area, n_{eff} is the effective index of a SRN waveguide, Γ is the overlap integral defined by Equation (6).

Table 1.1: Waveguide parameters retrieved from Lumerical (Ansys) simulations based on an SRN index and waveguide core geometry for a TE mode.

n	w, nm	d, nm	A_{eff}, μm^2	n_{eff}	Γ
2.5	550	383	0.43	1.87	0.49
2.7	500	386	0.36	2	0.51
2.86	480	390	0.32	2.13	0.54
2.96	400	377	0.32	2.06	0.43
3	440	337	0.29	2.13	0.5
3.08	424	351	0.28	2.2	0.51
3.15	375	343	0.28	2.13	0.42
3.2	375	337	0.27	2.17	0.45

4. Results

4.1 FWM

With the objective of determining the most optimal refractive index of SRN for FWM, we fabricated more than a hundred SRN devices with different refractive indices and waveguide lengths and captured the corresponding spectra on the OSA with a typical example (for a refractive index of 3.15) shown in **Figure 1.3**(a). Based on the generated idler power and GC CE, we calculated the idler power on a chip at the end of a waveguide, and the pump power and signal power at the beginning of a waveguide. Based on Equation (1)-(6), the FWM efficiency of each device was calculated for each waveguide length. The maximum efficiency was then retrieved from the FWM efficiency dependence on a waveguide length by fitting, as illustrated in Figure 1.3(b) for an SRN waveguide sample having a refractive index of 3.15.

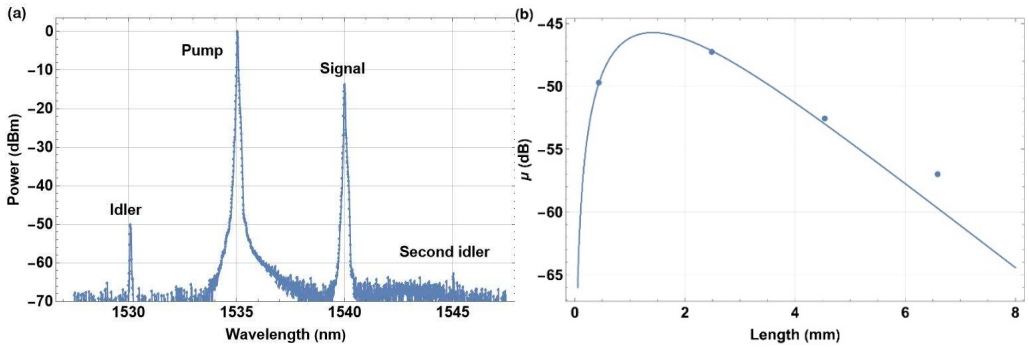

Figure 1.3: FWM implemented in a 3.15 SRN index waveguide at on-chip pump power of about 40 mW, (a) FWM spectrum measured by the OSA, (b) FWM efficiency dependence on a waveguide length.

Considering that the shortest waveguide length was approximately the same as that of the tapers (300 μm), it was important to calculate the FWM in the tapers as well. For that, the taper was split into small sections, and the parameters such as shown in Table 1 were calculated for each section. Then the idler generation in each section was calculated based on Equation (1)-(6). The total power of the idler generated in the two tapers was approximately the same as that in a 300 μm SRN waveguide. Consequently, the SRN FWM efficiencies throughout the manuscript have been rigorously presented by subtracting FWM powers generated by tapers.

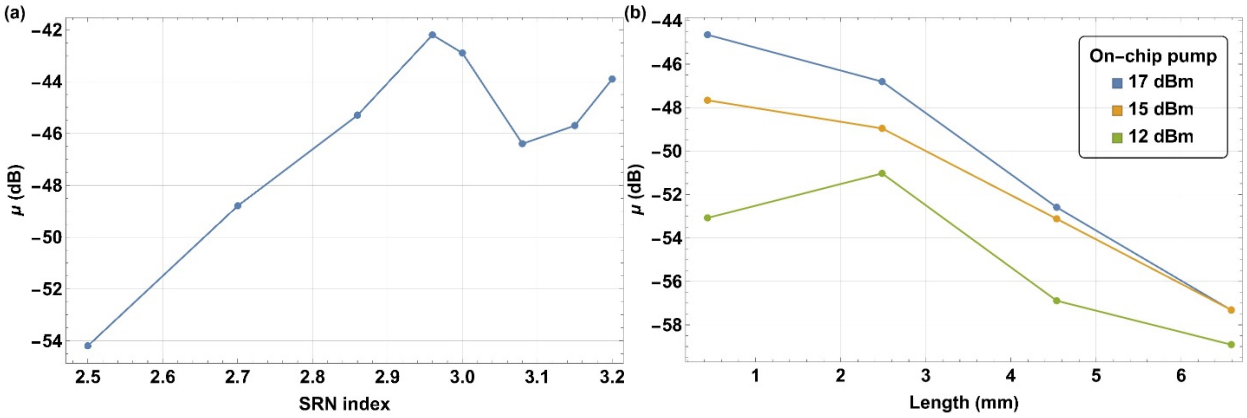

Figure 1.4: (a) FWM efficiency as a function of an SRN index, (b) FWM in a 3.2 SRN index waveguide as a function of on-chip pump power for four different lengths.

Figure 1.4(a) summarizes the measurements of the FWM efficiency μ, where its dependence on an SRN index of refraction is presented. As it can be seen in Figure 1.4(a), the efficiency steadily grows starting with a refractive index of 2.5 and peaks for the value of 2.96. Further increase in the index lowers the efficiency due to higher optical losses, even though χ_3 continues to increase. It is also important to note that in waveguides with indices greater than 2.7 FWM efficiency increases slower than P_p^2, indicating the presence of nonlinear losses. The latter effect is exemplified in Figure 1.4(b) for the SRN sample refractive index of 3.2 SRN waveguides.

As implied by the results shown in Figure 1.4(b), in the shortest waveguide (300 μm) the pump power reduction from 17 dBm to 12 dBm, leads to a 10 dB of efficiency decrease, which follows the expected P_p^2 dependence. However, in longer waveguides (2.3 mm – 6.5 mm) this is no longer the case.

For example, a 5 dBm of pump power reduction in the longest waveguide of 6.5 mm, leads to only 2 dB of efficiency decrease, indicating strong nonlinear losses in this case. Hence, it is anticipated that if pump power continues to increase, the peak of FWM efficiency from Figure 1.4(a) will shift to a lower index due to higher nonlinear optical losses in a larger index of SRN. Note that these experiments are valid for CW optical fields operation. As it will be shown later, the nonlinear losses are not related to TPA.

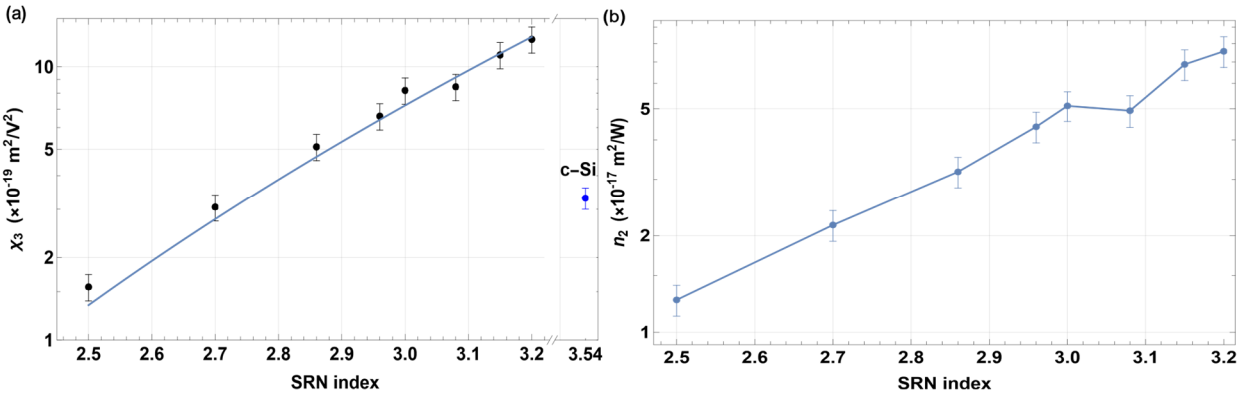

Figure 1.5: (a) Estimated χ_3 as a function of an SRN index (black dots) fitted by the Miller's rule curve (blue curve), and estimated χ_3 of c-Si, (b) n_2 dependence on SRN index. The fitting curve was retrieved from Wolfram Mathematica, the error bars represent the standard deviation error based on 3-5 measurements per SRN index.

Based on the calculated FWM efficiency and theoretical Equation (1)-(6), the sample's χ_3 was extracted as a function of an SRN index that was fitted by a curve described by the Miller's $\chi_3 \sim \chi_1^4$, rule, both results are shown in **Figure 1.5**(a). As seen in Figure 1.5(a), the measured χ_3 generally follows the Miller's rule well, only slightly deviating from it at lower SRN indices (those lower than 2.7). The maximum $\chi_3 = (12.6 \pm 1.4) \times 10^{-19}$ m^2/V^2 was estimated for the 3.2 index, while the minimum one of $\chi_3 = (1.56 \pm 0.17) \times 10^{-19}$ m^2/V^2 corresponded to the 2.5 index, which is about 8 times lower. As a countercheck, we also measured $\chi_3 = (3.3 \pm 0.4) \times 10^{-19}$ m^2/V^2 in a c-Si waveguide by the exact same method as for SRN waveguides, shown in Figure 1.5(a) as a separate point. The obtained parameter from the c-Si tests agrees very well with other reported results for the same material [26], indirectly confirming the validity of our SRN measurements. Notably the χ_3 value for the index 3.2 is almost 4 times as large as that of c-Si. Finally, the n_2 dependence on the refractive index is shown in Figure 1.5(b). The waveguide parameters, including the effective indices, were taken from Table 1. As it can been seen in Figure 1.5(b), the trend is similar to

that for the χ_3 as expected based on Equation (2), showing that $n_2 = (1.26 \pm 0.14) \times 10^{-17}$ m^2/W for the lowest 2.5 SRN index, while it is $n_2 = (7.6 \pm 0.8) \times 10^{-17}$ m^2/W for the largest 3.2 SRN index. Here we also provide **Table 1.2** that presents n_2 or χ_3 measured by different research groups by various methods, such as z-scan, FWM, DC Kerr effect, or self-phase modulation (SPM), and compare them with some of our results [6, 28, 31, 37].

Table 1.2: n_2 and χ_3 measured in various compositions of SRN in C-band by different research groups.

Reference	n	n_2 [$\times 10^{-17}$ m^2/W]	χ_3 [$\times 10^{-19}$ m^2/V^2]	Method
[37]	3.1	2.8	-	SPM
[6]	3.1	2.93	-	z-scan
[31]	3	-	6	DC Kerr
[28]	2.7	0.2	-	FWM
[28]	2.5	0.16	-	FWM
This work	3.1	5.0	8.5	FWM
This work	2.7	2.2	3.1	FWM
This work	2.5	1.25	1.56	FWM

4.2 Optical Losses in SRN Waveguides

In this subsection, we shall examine in more detail the observed sharp drop of the FWM efficiency for SRN samples having a refractive index higher than 2.96. Specifically, we measured an optical loss coefficient at both low and high powers using the cutback method. First, with the objective of avoiding nonlinear losses, light transmission was measured in each waveguide at low on-chip power of 500 μW, whereas optical losses were calculated based on the light transmission change as a function of a waveguide length, as shown in Figure **1.6**(a). An optical loss coefficient as a function of an SRN waveguide index and core width is shown in Figure 1.6(b).

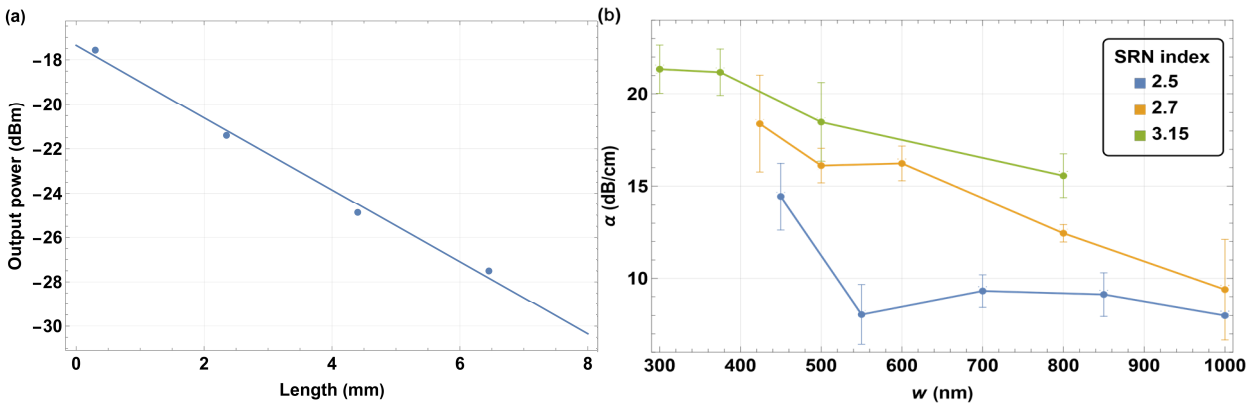

Figure 1.6: (a) Output power as a function of a waveguide length in a 3.15 index SRN waveguide with a core width of 600 nm, fitted by a linear function in Wolfram Mathematica to retrieve an optical loss coefficient, (b) optical loss coefficient α as a function of a width of an SRN waveguide core w for various SRN indices, measured at low optical power for a TE mode, the error bars represent the standard deviation error from the fitting.

As is apparent from Figure 1.6(b), optical losses in the low-power (i.e. linear) regime increase with a higher SRN index and a smaller waveguide core width, a result that is consistent with previous research reports on the subject [28]. Here we note that it is widely accepted in the literature that optical losses are predominantly caused by Si-H and N-H bonds in SRN films, as well as scattering due to surface roughness of sidewalls and top surface roughness of the waveguide core [1, 2, 3, 38, 39]. Note that chemical-mechanical polishing (CMP) can be used to smooth out the top surface roughness to reduce scattering losses [1, 3, 39], although CMP was not done in our experiments since it was not available to us. Consequently, large scattering losses prevail in smaller waveguide cores due to waveguide modes being pushed out of the waveguide core, which leads to a stronger electrical field of a mode being present on the rough sidewalls of a waveguide. Although, even if a mode is well confined in a larger waveguide, losses still remain high for a larger SRN index which indicates that SRN material losses also increase for SRN films with a higher refractive index. Optical losses as high as 21 dB/cm were measured in a 3.15 index SRN in a SM waveguide with a 375 nm core width, while 8 dB/cm losses were measured in a 2.5 index SRN in a SM waveguide with a 550 nm core width. Overall, measured optical losses are higher in PECVD SRN waveguides than in typical c-Si waveguides.

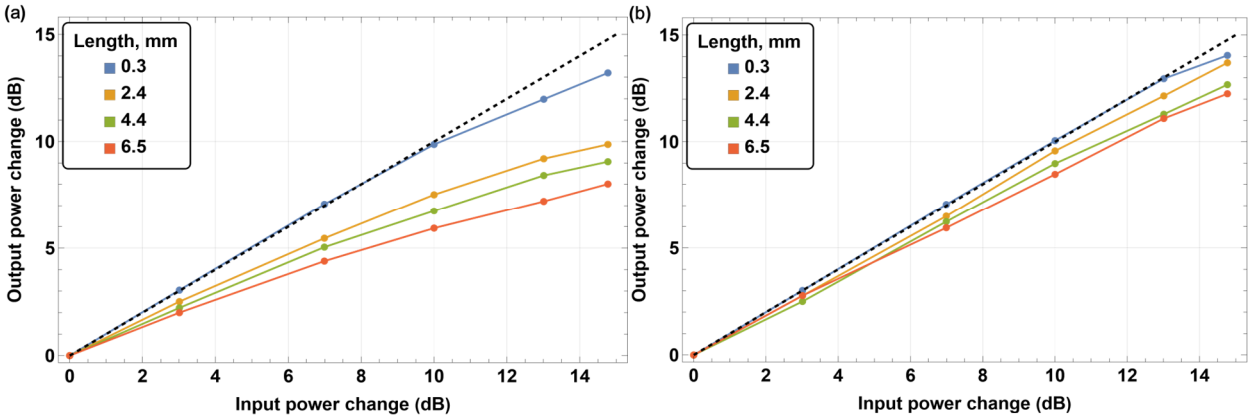

Figure 1.7: Measured output power increase as a function of on-chip power increase in a waveguide for an (a) SRN index of 3.2, (b) SRN index of 2.7, the dashed black line indicates no nonlinear loss.

As noted previously, optical losses also increase with an increase in the pump power in SRN waveguides for indices greater than 2.7. To observe the effect, the on-chip power was increased from about 1.5 mW to 40 mW (nearly a 15 dB increase) to measure transmission as a function of power. The results are shown in Figure 1.**7** for SRN indices of 2.7 and 3.2, where a measured output power change is plotted as a function of an on-chip input power change for various lengths of SRN waveguides.

Figure 1.7 shows that the transmission of the pump power in SRN samples having refractive indices of 2.7 and 3.2 deviates from a linear dependence (indicated by the dashed line), which suggests the presence of nonlinear losses in the material. The transmission is reduced for higher coupled power in SRN for both indices for longer waveguide lengths, indicating that the effect is caused by SRN waveguides rather than GCs, tapers, or other components in the setup. While nonlinear losses were seen in all our SRN waveguides with indices 2.7-3.2, no nonlinear losses were observed in c-Si waveguides and 2.5 index SRN waveguides. Furthermore, transmission of the signal power also reduces if high pump power is present in the same waveguide, the effect gets stronger for a larger SRN index at higher pump power in longer waveguides, similarly to the pump. For instance, at pump power of 40 mW coupled to an SRN waveguide with a refractive index of 3.2 and a length of 6.5 mm we observed extra 10 dB of signal loss. Consequently, it significantly reduces the efficiency of FWM as the pump, signal and idler power get reduced.

While the particular mechanism for increased nonlinear losses is not entirely understood, it does not seem to be related to TPA, as explained next (even though some previous publications reported TPA in a high index SRN [28]). Specifically, in order to examine the source of the cause of these losses, we measured high power light transmission in the waveguides with a refractive index of 3 with core widths varying between 440 nm and 5000 nm. Indeed, such a large difference is necessary to reduce the peak intensity in the larger waveguides in order to minimize (or eliminate) the potential for TPA. In these measurements the transmission in the larger waveguides did not change significantly, indicating that the nonlinear loss mechanism depends on average power rather than peak intensity, thereby precluding the occurrence of TPA. Furthermore, this result also excludes other nonlinear processes that depend on peak intensity, such as stimulated Brillouin scattering (SBS).

To better characterize the observed nonlinear losses, we introduce the nonlinear loss coefficient β in Equation (8), that follows the same equation as a TPA coefficient for a given waveguide geometry:

$$\frac{dI}{dz} = -\beta I^2 \tag{8}$$

where I is the optical intensity of a mode propagating in a z direction. Based on the results demonstrated in Figure 1.7 we calculated an output optical intensity as a function of an SRN waveguide length and fitted it in Wolfram Mathematica with the solution from the Equation (8), while taking into consideration an overlap integral in an SRN waveguide core. The result is shown in Figure **1.8**(a) for an SRN index of 3.2. From the fitting we estimated the nonlinear coefficients of multiple indices of SRN waveguides and presented the results in Figure 1.8(b).

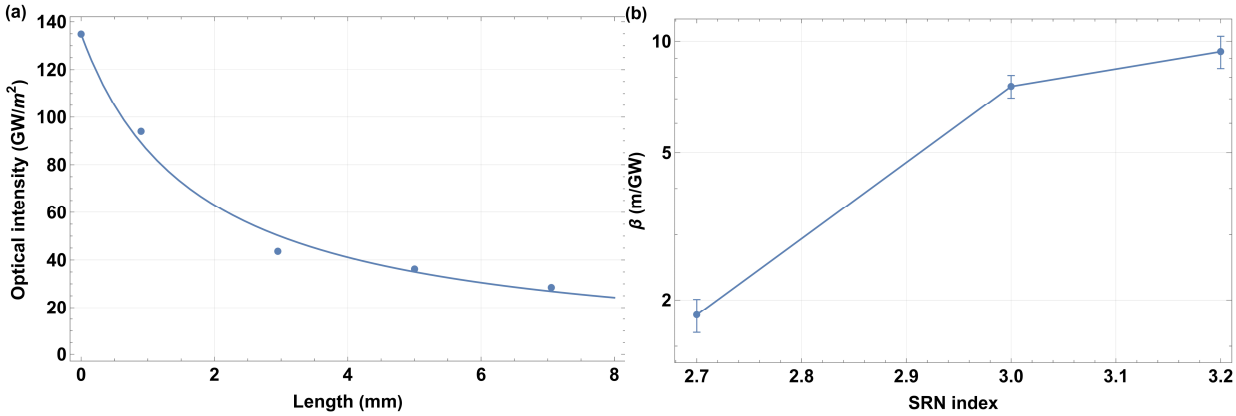

Figure 1.8: (a) Fitted output optical intensity on chip as a function of a waveguide length for an SRN index of 3.2 at 40 mW power, (b) estimated β coefficient for different SRN indices, the error bars are retrieved from fitting in Wolfram Mathematica as the standard deviation error.

It follows from Figure 1.8(a) that the loss coefficient β indeed follows a linear dependence on optical intensity assumed in Equation (8), similarly to TPA. However, the estimated coefficient β is significantly higher than the TPA coefficient β_{TPA} reported in c-Si. Explicitly, β_{TPA} = 0.015 m/GW in c-Si in the C-band is ~2 orders of magnitude lower than $\beta = (1.82 \pm 0.17)$ m/GW estimated for the 2.7 index SRN waveguide in our measurements [26]. Furthermore, it is important to note that unlike in the case of TPA, β depends on geometry of a waveguide. Therefore, the comparison with TPA here is only reasonable for comparable geometry of waveguides. Nevertheless, the direct comparison clearly demonstrates that SRN waveguides with a refractive index higher than 2.7 exhibit significantly higher nonlinear losses than c-Si for CW signals.

A detailed study of the nonlinear loss dynamics is beyond the scope of this manuscript and will be published elsewhere. Suffice it to say that the effect can be reduced and even eliminated with an appropriate short-pulse excitation. As an illustration, Figure **1.9** demonstrates the propagation of a pulsed 1550 nm wavelength laser source, with 200 fs pulses and 10 MHz repetition rate. The pulses were generated by an FPL-02CFTUSD12 Calmar laser.

As observed in Figure 1.9, even at high peak power of 5 W coupled to a 440 nm wide SRN waveguide with a refractive index of 3, no nonlinear losses can be observed, and the transmitted power follows a linear dependence on the coupled power. The last result indicates that not only is it possible to

suppress the nonlinear losses with a proper excitation, but, more importantly, it also precludes the TPA as their source, even at very high peak power.

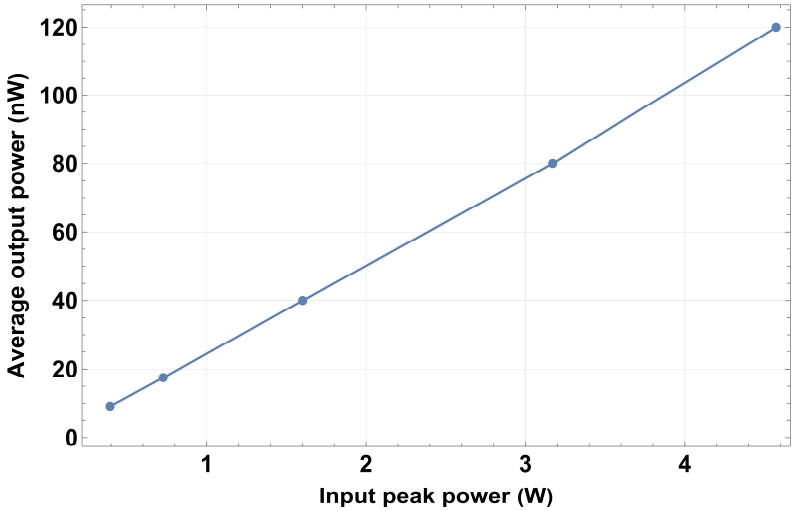

Figure 1.9: Measured average output power as a function of on-chip peak power in a 440 nm index 3 SRN waveguide for 200 fs pulses with a 10 MHz repetition rate.

5. Conclusion

In conclusion, we have presented a comprehensive study of the nonlinear optical properties of silicon-rich nitride single mode waveguides. Our investigation was primarily based on four-wave mixing efficiency characterization. Specifically, we have demonstrated that the refractive index in SRN waveguides represents an important degree of freedom that can be used to optimize the nonlinear wave mixing. Most importantly, novel results have revealed the existence of a trade-off between the nonlinear response of SRN and optical losses, including nonlinear losses at higher power. In fact, a refractive index of around 3 (at 1550 nm) of SRN waveguides maximized the efficiency of FWM for CW operation in the C-band. On top of that, we have measured the maximum $n_2 = (7.6 \pm 0.8) \times 10^{-17}$ m^2/W and $\chi_3 = (12.6 \pm 1.4) \times 10^{-19}$ m^2/V^2 in a refractive index 3.2 SRN waveguide, which is almost 4 times larger than that in c-Si. However, it was also observed that an SRN waveguide with a refractive index of 3.2 suffers from higher optical losses, limiting the maximum useful length of an SRN waveguide device. The optical losses, caused by both sidewall scattering and an SRN waveguide core absorption, can be reduced by increasing a waveguide core thus minimizing scattering losses. We have also observed and characterized nonlinear

optical losses in SRN waveguides (with a refractive index higher than 2.7) at higher CW power, and we have shown that the nonlinear losses are not related to TPA as it is possible to altogether eliminate the nonlinear losses by utilizing high peak power short pulses (200 fs).

Thus, we have established the importance of measuring optical losses at high CW optical power in order to optimize an SRN fabrication recipe and ensure the optimal operation of nonlinear devices in this platform due to the existence of nonlinear losses.

Acknowledgements

Chapter 1, in part, is a reprint of the material published in Advanced Photonics Research. The dissertation author was first author of this paper, with co-authors Nikola Alic, Andrew Grieco, and Yeshaiahu Fainman.

CHAPTER 2 - DYNAMICS OF NONLINEAR OPTICAL LOSSES IN SILICON-RICH NITRIDE NANOWAVEGUIDES

1. Introduction

Silicon-rich nitride (SRN) on insulator is a promising integrated photonics platform for nonlinear optics due to its large optical nonlinear response, which increases with higher concentration of Si [1]. Specifically, the third order susceptibility χ_3 of SRN grown by plasma-enhanced chemical vapor deposition (PECVD) with a refractive index of 3.2 (at 1550 nm) is around 12.6×10^{-19} m^2 V^{-2}, which is about 4 times larger than that of crystalline silicon (c-Si) [1]. A particularly remarkable property of SRN is the ability to change its linear and nonlinear optical properties in a wide range by changing Si content in SRN thin film deposition and post-processing parameters. Specifically, changing these parameters allows optimization of the refractive index, optical nonlinearities, optical losses (including nonlinear optical losses), and optical transparency window, and thereby maximizing the efficiency of the SRN nonlinear response such as, for example, wave mixing [1, 2, 3]. Another beneficial property of SRN is its larger refractive index, allowing the light to be confined tighter in a waveguide, which is crucial for nonlinear wave mixing as it reduces the waveguide's effective mode area, thus, improving the overlap between the mode and nonlinear media. Indeed, the aforementioned set of circumstances enables efficient nonlinear processes in SRN devices such as four-wave mixing (FWM) [1, 2], supercontinuum generation [4, 5, 6], DC Kerr effect [7], nonlinear Kerr switching [8], intermodal frequency generation [9], second harmonic generation [10]. Another advantage of the SRN platform is a relatively large electric field breakdown of around 100 V/μm [7], much larger than that of c-Si, around 40 V/μm [11]. It increases the efficiency of the devices that require application of strong electric field, such as electric field induced second harmonic generator (EFISHG) or linearized Kerr effect electro-optic modulator. Such devices were demonstrated on the c-Si and Si_3N_4 platforms [11, 12, 13], and they are yet to be demonstrated on the SRN platform. Additionally, the thermo-optic coefficient of SRN also increases for higher refractive indices [14], which led to demonstrations of efficient thermo-optic SRN devices such as bi-stable optical switcher [15], thermo-optic phase shifter [16], and optical phased array [17], to name a few.

On the other hand, the seemingly outstanding potential for nonlinear optics applications of SRN is quenched by the existence of nonlinear optical losses that have been observed and described in SRN in our prior work [1]. Indeed, nonlinear losses in SRN were reported in multiple instances, and it was suggested that these are due to the two-photon absorption (TPA) process [18, 19]. However, there are several mechanisms that can be the cause of nonlinear losses in optical waveguides, including TPA (and multi-photon absorption in general) [18], free carrier absorption (FCA) [20], stimulated Brillouin scattering (SBS) [21, 22], stimulated Raman scattering (SRS) [23], self-phase modulation (SPM) [24, 25], cross-phase modulation (XPM) [26], FWM [1, 2], and others. In fact, the effects that can give rise to nonlinear losses are distinguishable by the particular way they affect light propagation in waveguides. For instance, all the mentioned processes have very different generation and relaxation dynamics, with TPA being characterized as ultra-fast, due to its dynamics being only limited by electron transition times, thus allowing it to be observed even when short femtosecond optical pulses are utilized [27]. Conversely, nonlinear processes such as SPM, XPM and FWM induce a spectral change in a propagating optical signal, hence their contribution can be confirmed by changes in the optical spectrum of the transmitted or reflected light [1, 2, 24, 25, 26]. On the other hand, FCA can have very diverse dynamics depending on the material properties, waveguide geometry, and optical power, owing to the variety of different mechanisms of the free carrier generation and recombination processes. Specifically, Auger, Shockley-Read-Hall (nonradiative), radiative, surface recombination processes are responsible for free carrier absorption, while TPA and defects (with energy states in a bandgap serving as recombination-generation (R-G) centers) are responsible for free carrier generation [20, 28, 29, 30], affecting the FCA dynamics substantially. In addition, it is important to emphasize that FCA does not lead to any spectral change of a propagating optical signal at a given optical frequency/wavelength, making it impossible to be identified by a mere measurement of the signal transmission spectrum [28]. Therefore, it can be problematic, at best, to confirm that any observed nonlinear loss is caused by FCA. Nonetheless, there are different ways to identify this loss mechanism. For example, the latter can be accomplished by measuring the loss dependence on the wavelength of light and comparing it to the predictions of the Drude model [31, 32, 33], which specifically predicts higher losses

for longer wavelengths. Alternatively, FCA dynamics can be characterized to estimate the recombination lifetime to determine the presence of particular recombination mechanisms such as Auger, or Shockley-Read-Hall recombination [29, 34]. In fact, FCA is commonly observed in c-Si and amorphous silicon (a-Si) waveguides in C-band. Here TPA generates free carriers, leading to nonlinear optical losses that limit applications of Si in nonlinear optics [30, 35, 36, 37]. In addition, we previously observed nonlinear losses in SRN waveguides with refractive indices larger than 2.7 in C-band for the continuous wave (CW) operation [1]. However, we established that such losses are not caused by TPA as demonstrated by the observation of linear transmission of high peak power short optical pulses (5 W, 200 fs) at the repetition period of 100 ns [1]. Those results clearly established that the cause of the losses had a generation lifetime longer than 200 fs. We also determined that such losses cannot be due to SBS, SRS, SPM, XPM, FWM nonlinear processes mentioned above [1].

In this manuscript, we conduct a comprehensive investigation into the cause of the nonlinear losses observed in PECVD SRN waveguides and present detailed results on their dynamics. Furthermore, we provide evidence that the observed nonlinear optical losses in our SRN waveguides are caused by FCA. Specifically, we measured electrical current in SRN thin films across a range of refractive indices from 2.5 to 3.2 to determine the presence of free carriers. During the measurements, C-band laser light was incident on the films while a DC electric field was applied. In this setup, indeed, we observed a photo-induced current (photocurrent), which was found to increase exponentially with the SRN waveguide refractive index, indicating the generation of free carriers under light illumination. This finding, to the best of our knowledge, is a novel result. In addition, we introduce a novel approach for measuring both generation and recombination dynamics of the nonlinear losses induced by FCA in SRN waveguides. This approach is based on a single complex shape optical signal pulse source, as opposed to the common pump-probe approach where both optical pump pulse and signal are used [34]. Notably, free carrier generation and recombination dynamics were characterized for various SRN waveguides across a range of refractive indices and optical powers, and the new finding reveals that as the SRN refractive index increases, both

generation and recombination lifetimes decrease. Most importantly, it was demonstrated that nonlinear losses can be minimized or altogether avoided by utilizing optical pulses shorter than the generation lifetime, while ensuring that the repetition period of the pulses is longer than the recombination lifetime. Thus, this approach enables the exploitation of the large nonlinear properties of SRN while avoiding nonlinear losses. Here we also want to note that our PECVD SRN deposition recipe is unique to our group, therefore the obtained results may be different for various SRN preparation methods (such as low-pressure chemical vapor deposition (LPCVD), inductively coupled plasma chemical vapor deposition (ICPCVD), PECVD, etc.) and specific recipes used by other research groups.

The manuscript is organized as follows: The photocurrent experiment conducted in SRN thin films is analyzed and described in Section 2, characterization and analysis of the nonlinear loss dynamics observed in SRN waveguides is presented in Section 3, whereas the discussion of the findings and conclusions are summarized in Section 4.

2. Photo-Induced Current in SRN Thin Films

2.1 Fabrication and Setup

The primary purpose of this section is to demonstrate that the observed nonlinear optical losses in SRN waveguides in C-band are caused by FCA due to photo-induced free carriers generated in SRN. Indeed, in this case photocurrent ought to be observed in a high refractive index SRN thin film when C-band laser light is incident on the film, due to the generated free carriers. Furthermore, a proper approach should consist of measuring the photocurrent in SRN film samples with varying refractive indices in order to ensure that the photocurrent increases with the refractive index, similarly to the trend observed in the associated nonlinear optical losses in SRN waveguides. With that objective, five different SRN film samples with different indices (2.5, 2.65, 2.85, 2.95, and 3.15) were fabricated and characterized. In particular, Figure 2.1(a, b) demonstrate two different fabrication flows implemented for our SRN samples. Specifically, in the first approach described in Figure 2.1(a), a Heidelberg MLA 150 photolithography equipment was used to expose an electrode pattern, followed by Au sputtering in a Denton 635 sputter

system, after which the lift-off was implemented in a Remover PG. Finally, SRN thin film and SiO_2 cladding were deposited in an Oxford Plasmalab PECVD system on the top of the sample. It is also worth mentioning that covers were placed on the top of the samples, specifically in the electrode pads' locations, to protect them from SRN and SiO_2 cladding deposition. This allowed electrode probes to be attached to the corresponding pads, enabling the application of a DC electric field. Notably, the fabrication flow shown in Figure 2.1(a) simplified the fabrication process. Indeed, the adopted approach made possible to use the same dose and defocus of the photolithography process, regardless of an SRN thin film refractive index and its thickness, since the film was deposited after the photolithography exposure of an electrode pattern. Note that an optimal dose and defocus would be different for each SRN index if the photolithography was done after SRN thin film deposition. Furthermore, the gap between the electrode tips (electrode gap) was varied in size between 12 µm, 15 µm, and 20 µm to diversify the photocurrent measurement results not to rely on a single measurement per sample. Meanwhile, the electrode length was 50 µm for all samples. The electrode gaps were intentionally made small to enhance the applied DC electric field and, thus, to increase the photocurrent, which was expected to be small in the first place. The thicknesses of electrodes and SRN films were designed to be about 700 nm - thick enough to generate the detectable photocurrent, while avoiding thin film cracking due to stress. Additionally, an alternative fabrication approach, shown in Figure 2.1(b), was implemented to specifically demonstrate the effect of rapid thermal annealing (RTA) on the photocurrent in the fabricated SRN samples (as detailed in Section 2.2). In fact, it was found critical to anneal SRN deposited on a SiO_2 substrate before fabricating the electrodes, since otherwise the electrode tips would bump into each other after annealing, as a consequence of SRN films being compressed during the annealing at high temperatures. In the adopted approach, the photocurrent is still generated in an SRN film even with the presence of SiO_2 between the electrode tips, since the DC electric field permeates the material underneath the electrodes, where there is a contact with an SRN thin film. The electrode gaps and SRN thin film thicknesses for the annealed samples (from Figure 2.1(b)) were consistent with those described in Figure 2.1(a), while the thickness of Au electrodes was 400 nm. Finally, Figure 2.1(c) shows a microscope image of the electrode tips for the approach presented in Figure 2.1(b).

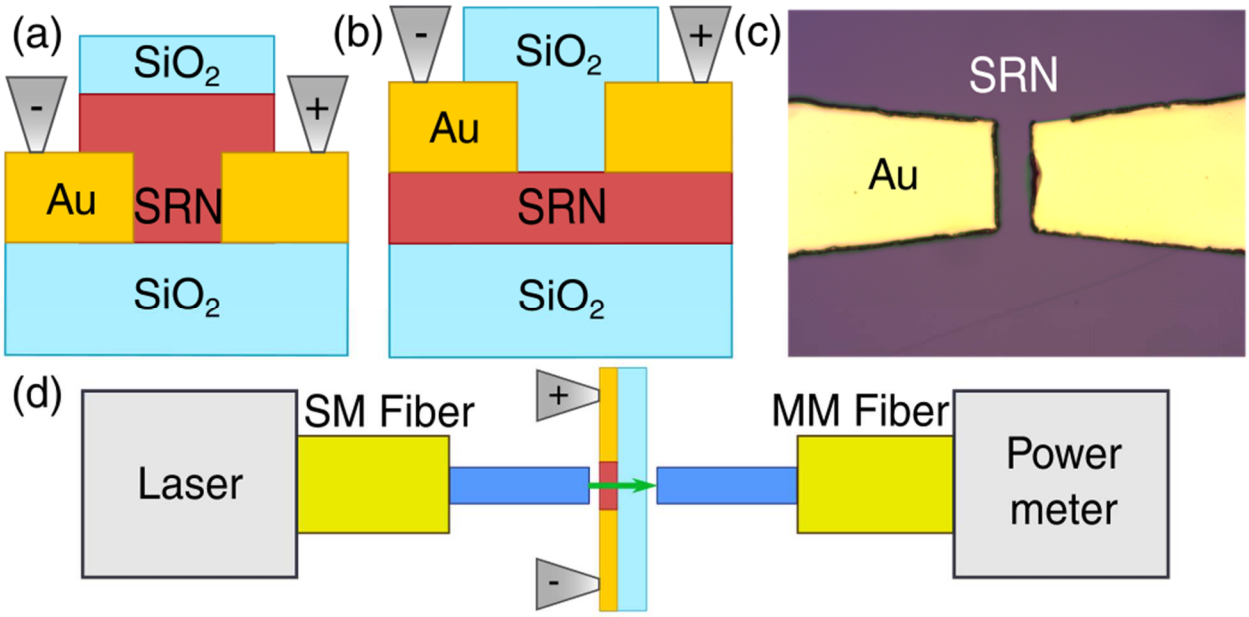

Figure 2.1: Schematic of a fabricated SRN sample with electrodes where (a) SRN thin film was deposited on Au electrodes, (b) SRN thin film was deposited on SiO_2 substrate, then Au electrodes were fabricated on top of SRN film; (c) image of electrode tips fabricated on SRN film, the electrode gap is 20 μm; (d) setup for photocurrent measurement depicting a sample with electrodes (grey) attached, SM fiber patch cable (yellow) with a bare fiber (blue) on the left to couple light onto the sample surface (green arrow), and MM fiber patch cable with a MM bare fiber on the right to couple light out.

The setup used to characterize the photocurrent as a function of the SRN index is shown in Figure 2.1(d). A laser (Agilent 81980A), emitting at 1540 nm, was used to illuminate the sample and generate the free carriers. The light was coupled to a single mode (SM) patch cable (mode field diameter ~10 μm) with a bare fiber tip pointing towards the SRN sample. Since the gap between the fiber tip and the sample surface was on the order of 10 μm, a beam divergence could be neglected since the Rayleigh length was estimated at 50 μm. Therefore, the beam size was maintained at ~10 μm, as was necessary to fit the SRN aperture located between the electrode tips. At the opposite end of the SRN sample, light was collected by a multi-mode (MM) 50 μm core fiber which facilitated the alignment of the SM fiber relative to the SRN aperture and, thus, maximization of measured photocurrent. A Keithley 2400 source meter was used to apply the DC electric field across the SRN film and measure the generated photocurrent, wherein needle electrodes, connected to the source, were attached to the electrode pads deposited on the SRN samples. The fibers, samples, needle electrodes were placed on positioning stages to allow accurate alignment of all the components.

2.2. Experimental results

DC voltage of 210 V was applied to the electrode pads to generate and measure the electric current in the SRN samples. Notably, a non-negligible current was observed in the SRN samples even in the absence of laser light. However, a markedly stronger current was detected when the laser was engaged (its power was set to 14 dBm), indicating a presence of strong photocurrent. Under the described conditions it is natural to introduce a total current I, consisting of a sum of the current when there is no light I_0, and the photocurrent I_{ph}, when the sample is exposed to laser light, such that:

$$I = I_0 + I_{ph} \tag{1}$$

Figure 2.2(a) shows I and I_0 measured as a function of an SRN refractive index when the DC voltage of 210 V was applied to the electrodes having the gaps of 20 μm and 12 μm. It is apparent that the current dependence on the SRN index is exponential (i.e. linear in the semi-logarithmic scale) for both electrode gaps, indicating a significant increase in the free carrier concentration in SRN films with a higher index. Note that the experiment was conducted in a dark room to minimize current generation from the ambient light. In particular, Figure 2.2(b) demonstrates the total current as a function of an SRN refractive index for the electrode gap of 12 μm fitted by a linear function in Wolfram Mathematica. Based on the fitting, we derived the following formulae for the total current dependence on the SRN refractive index: $I = 10^{-(18.9\pm1.4)+(7.1\pm0.5)n_{srn}}$ for the gap of 20 μm, and $I = 10^{-(19.7\pm1.4)+(7.5\pm0.5)n_{srn}}$ for the gap of 12 μm, where n_{srn} is the SRN refractive index, and the presented error bars are based on 95% confidence intervals. As can be observed in Figure 2.2(a), overall, a stronger current is generated when the electrode gap is smaller due to the consequent larger electric field between the electrodes' tips, as dictated by the Ohm's law. This also demonstrates why it was important to keep the SRN area between the electrodes as small as possible – namely to increase the generated photocurrent so that it can be detected even at lower refractive indices of SRN.

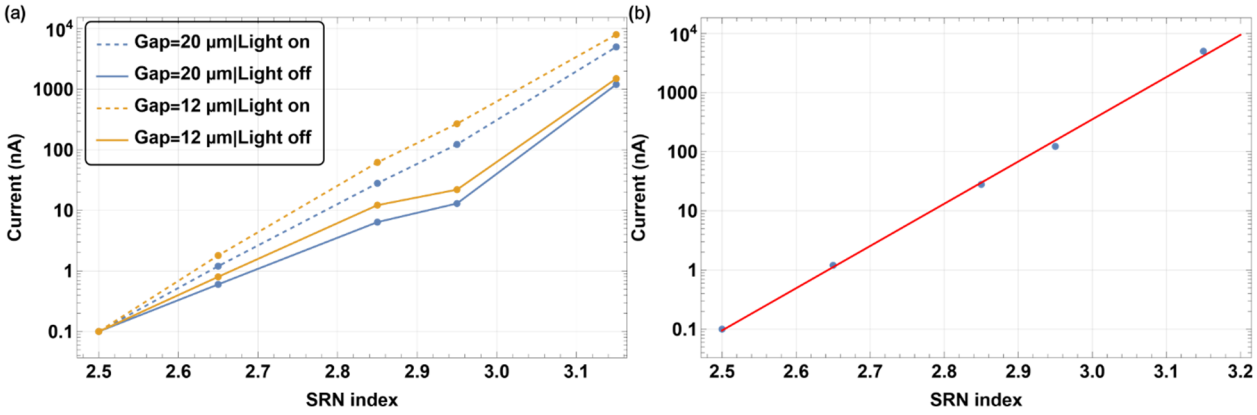

Figure 2.2: (a) Current as a function of an SRN refractive index at 210 V DC. Dashed lines represent the total current I when 14 dBm of power is on (Light on), while solid lines represent the current when there is no light I_0 (Light off); blue is for the electrode gap of 20 μm, orange is for 12 μm, (b) total current as a function of an SRN refractive index for the electrode gap of 12 μm (dashed orange line from (a)) fitted by a linear function in Wolfram Mathematica.

Notably, both I_0 and I_{ph} appear to be negligible for the lowest SRN index of 2.5. This observation agrees well with the premise that the nonlinear losses observed in SRN waveguides are due to FCA, since the nonlinear losses were not observed in SRN with the index of 2.5, which was demonstrated in our previous work [1], and will be further elaborated on in the current manuscript in the next section. It suffices to note at this point that the largest photocurrent was observed in the sample with the highest SRN refractive index of 3.15, matching the equivalent result for the nonlinear losses observed in SRN waveguides. Needless to say, the observed behavior strongly implies free carrier generation by the incident light. The generated carriers, in turn, absorb the light, subsequently causing nonlinear losses in SRN waveguides.

We also rigorously measured the photocurrent I_{ph} (defined as $I - I_0$) as a function of optical power in the fabricated SRN samples to determine if it follows a linear trend. The measured curves, fitted by a linear trend in Wolfram Mathematica, are shown in Figure 2.3(a) for SRN indices of 3.15 and 2.95 with 210 V of DC voltage applied for the 12 μm electrode gap. It can be seen that photocurrent observed in the SRN sample with the index of 3.15 exceeds that measured in the sample with the index of 2.95 for any optical power. Interestingly, it starts growing at a faster rate (at the power of around 15 dBm) than predicted by the linear dependence. The observed rise in photocurrent ultimately leads to electric field breakdown at higher optical power. On the other hand, the SRN sample with the index of 2.95 clearly exhibits a linear

dependence of the measured photocurrent, even for higher optical powers. More importantly, no voltage breakdown was observed in the second sample with the refractive index of 2.95, nor has it been observed in any samples with a refractive index lower than 2.95. Overall, the photocurrent is consistently larger for a higher SRN refractive index at any optical power used.

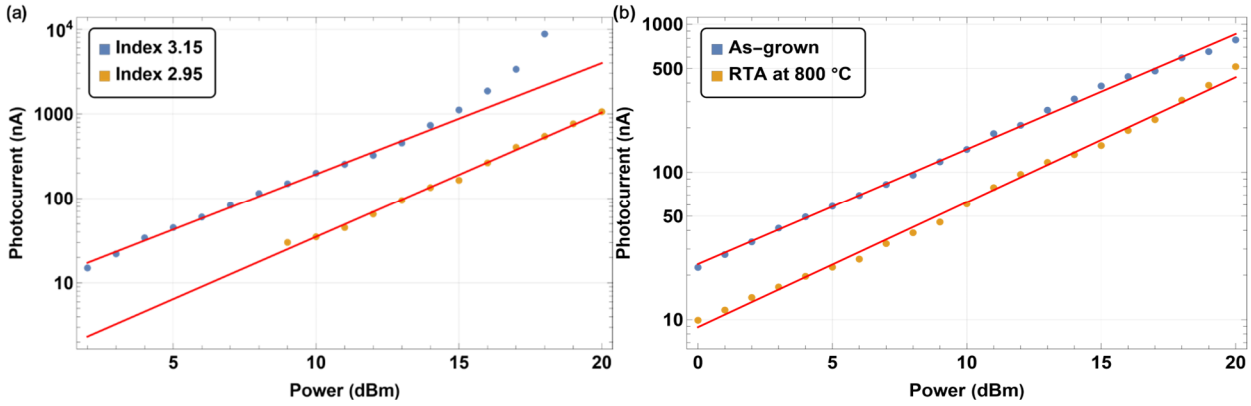

Figure 2.3: Photocurrent I_{ph} as a function of optical power at 210 V DC applied for (a) SRN indices of 3.15 (blue) and 2.95 (orange), (b) as-grown SRN film with refractive index of 2.95 (blue) and annealed one at 800 °C (orange). The data was fitted by a linear trend in Wolfram Mathematica.

As for the origin of the observed trend, it is well-known that SRN with a higher refractive index contains more Si and hydrogen (H) [1]. In fact, the latter is due to the silane SiH_4 gas used in PECVD SRN deposition. Specifically, since the measured photocurrent increases with the SRN sample refractive index, it is crucial to understand whether the increase in Si, H, or both-related defects or impurities are responsible for the observed increase of the photocurrent. Accordingly, with the purpose of determining the effect of Si/H defects or impurities on the photocurrent, we fabricated two identical SRN samples with the index of 2.95 following the approach depicted in Figure 2.1(b), then implemented RTA at 800 °C for 2 min for one sample with the aim of reducing the defect density [38, 39, 40]. As a result of the described annealing process, we observed an increase in the sample's refractive index to 3.15, as a consequence of the increased concentration of Si and density of the film. We subsequently measured the photocurrent in the pair of samples (i.e. in an as-grown SRN film and the annealed sample), and it was confirmed that RTA indeed did reduce the photocurrent measured in the corresponding SRN samples with various electrode gaps (12 µm, 15 µm, and 20 µm). The photocurrent was once again captured for this set of samples as a function of

optical power. The results are presented in Figure 2.3(b), and, similarly, the photocurrent in the as-grown sample was found to consistently exceed that in the annealed one, despite the fact that the refractive index of the latter was much higher. Therefore, it is straightforward to conclude that RTA at 800 °C for 2 min of SRN results in a reduction of the photocurrent. Since annealing is known to reduce the defect density [38, 39, 40], we hypothesize that the photocurrent is caused by the defects present in SRN samples. On the other hand, the fact that the photocurrent remains relatively large even in the annealed samples implies that either the remaining defects and impurities cause the photocurrent, or there is some other mechanism that may be responsible for carrier generation. In any event, the detailed study of defects and impurities present in SRN, while necessary for full comprehension, is beyond the scope of this manuscript.

3. Nonlinear Loss Dynamics in SRN Waveguides

3.1 Fabrication and Setup

Having established FCA to be the main cause of the nonlinear optical losses in SRN waveguides, we set out to rigorously characterize its dynamics and measure both the associated free carrier generation and recombination lifetimes. For reference, it should be noted that in our previous work [1], we have determined that TPA is absent in the fabricated SRN waveguides at the power levels where the nonlinear losses are observed. This consideration also indicates that the cause of free carrier generation is related to the defects present in SRN films (as supported by the experimental results in Section 2 above). Therefore, given that larger nonlinear losses were observed in higher refractive indices of SRN waveguides [1], a reduction of carrier generation and recombination lifetimes is anticipated due to the increase in the defect density. Moreover, it should be possible to avoid nonlinear losses altogether by using optical pulses shorter than the generation lifetime, provided that the pulse repetition period is longer than the recombination lifetime to avoid carrier accumulation and facilitate the carrier recombination process. To strictly determine whether these statements indeed hold true, we assembled the setup presented in Figure 2.4(a), which allowed us to characterize the dynamics of the optical pulse transmission in SRN waveguides. In the setup shown in Figure 2.4(a), a 12.5 Gb s^{-1} N4903A pattern generator from Agilent Technologies (generally known as a J-BERT) was used to generate an electrical pulse pattern to drive a 40 GHz lithium niobate

intensity modulator, which was used to shape optical pulses by modulating a 1540 nm optical signal emitted by an Agilent 81980A CW laser, after a transverse electric (TE) polarization was set by polarization controllers. A C-band erbium-doped fiber amplifier (EDFA) was used to amplify the optical pulse stream, whereas an optical isolator was placed immediately after the amplifier to prevent the high peak power pulse back reflection into the EDFA. Next, a beam splitter was used to direct -20 dB of the optical pulse power to an HP 83485B 30 GHz optical detector for monitoring on an 83480A digital communications analyzer (DCA) from Hewlett Packard, used as a sampling oscilloscope. The rest of the optical pulse power was coupled to the SRN waveguide under test (the cross-section presented in Figure 2.4(b)), after a TE mode was set by polarization controllers. Finally, -10 dB of a transmitted optical pulse was coupled to an optical power meter to measure average transmitted power, while the rest was coupled to an 83440D 32 GHz lightwave detector from Agilent, connected to the sampling oscilloscope to capture and characterize the dynamics of transmitted optical pulses.

The probing (signal) optical pulse (observed on the oscilloscope) had a rise time of about 50 ps and was limited by the rise times of the pattern generator, the sampling oscilloscope, and the 32 GHz photodetector. Consequently, the specified pulse duration allowed reliable measurements of the carrier generation lifetime as short as 50 ps. On the other hand, the maximum repetition pulse period was limited to ~2 μs, as confirmed experimentally, to ensure that the optical pulse distortion (caused by the EDFA transition dynamics) is avoided. Therefore, the described experimental condition allows the measurement of a carrier recombination lifetime as long as 2 μs. As will be shown later, the observed nonlinear loss dynamics fit well within the specified limits, enabling an accurate determination of both recombination and generation lifetimes. Note that the repetition period shorter than the EDFA transition dynamics, such as in our case, enables enhancement of the peak power P_{peak}, with respect to the average power P_{av}, for a pulse duty cycle D, as $P_{peak} = P_{av}/D$. In our case, the pulse duration and repetition period were 200 ns and 2 μs, respectively, leading to a duty cycle of 0.1, and thus, $P_{peak}/P_{av} = 10$, allowing creation of high peak power

optical pulses. Therefore, this setup allowed us to increase the peak power without changing the average power by simply altering the pulse duration duty cycle ratio.

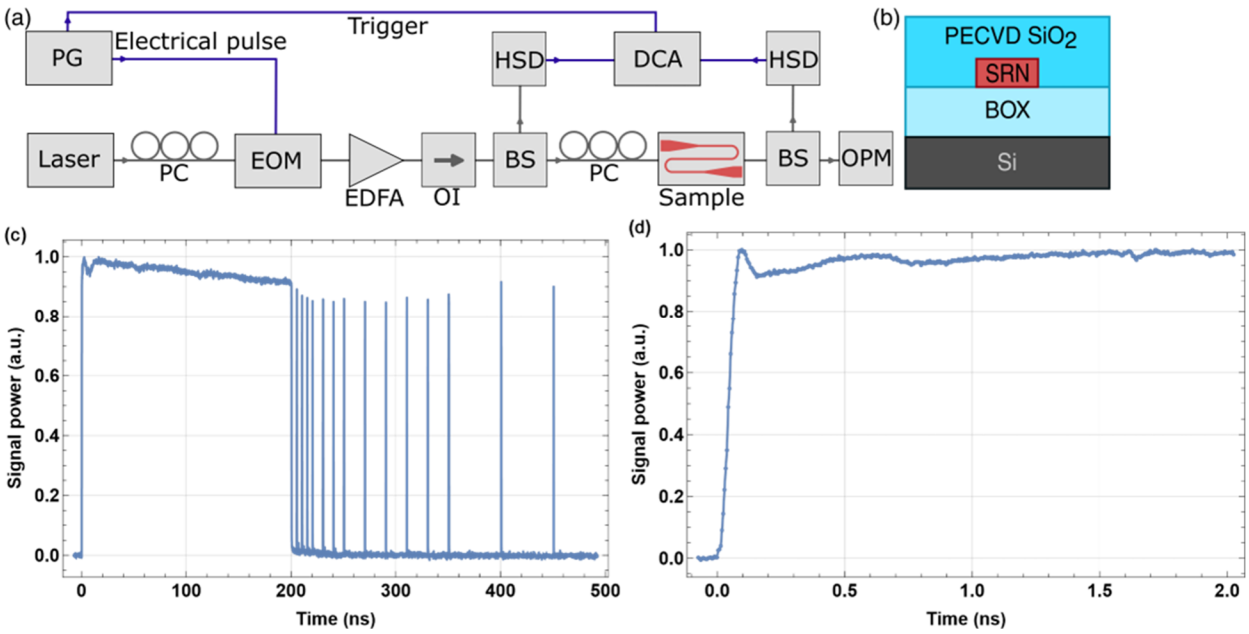

Figure 2.4: (a) Block diagram of the setup used to characterize nonlinear loss dynamics by measuring optical pulse transmission, where blue arrows represent an electrical signal, gray arrows represent an optical signal. PG: Pulse pattern generator as an electrical pulse source, EOM: Electrooptic modulator based on lithium niobate, EDFA: Erbium-doped fiber amplifier, OI: Optical isolator, BS: Beam splitter, PC: Polarization controller, HSD: High speed photodetector, OPM: Optical power meter, DCA: Digital communications analyzers as a sampling oscilloscope. (b) Cross-section of an SRN waveguide used in the experiments. Normalized optical power of a signal pulse measured on the oscilloscope, used to characterize the nonlinear loss dynamics in SRN waveguides: (c) Large timescale (500 ns) demonstrating a complex shape pulse consisting of a 200 ns pulse followed by a time-comb of short ~200 ps pulses, (d) short timescale (~2.5 ns) demonstrating the front edge of the pulse with the rise time of about 50 ps.

In general, it is possible to estimate a free carrier generation lifetime by using only one optical pulse source (signal) by measuring the pulse transmission through a device, even though two sources of light are typically utilized (pulsed pump and CW probe) to measure a recombination lifetime [34]. However, in our study, we implemented a different approach, taking advantage of the pulse generator's ability to generate non-return-to-zero patterns (a binary code). Specifically, a generated waveform used to probe the SRN samples consisted of two parts, where the first part was a continuous 200 ns long optical pulse that generated free carries, while the second part consisted of a series of short isolated 200 ps pulses, in effect forming a comb in the time domain, as demonstrated in Figure 2.4(c). Such a comb created only a negligible

concentration of free carriers, since the duration of each constituent pulse was shorter than the free carrier generation lifetime, thus not affecting the free carrier recombination. Therefore, the lifetime of the latter can be estimated simply by observing the response dynamics of the comb at the output of the SRN waveguide under test (i.e. transmission dynamics). Consequently, as explained above, our novel approach allowed us to characterize both generation and recombination lifetimes based on transmission dynamics, by using just an optical pulse signal, simplifying the free carrier dynamics characterization. Additionally, Figure 2.4(d) shows the front edge of the 200 ns optical pulse (same as from Figure 2.4(c)) exiting from the EDFA, and it can be seen that the rise time is around 50 ps. The minor amplitude variation (<10%), that is observed in both Figure 2.4(c)-(d), is caused by the transient dynamics of EDFA.

To demonstrate how FCA dynamics changes with the SRN index, multiple SRN waveguides with the length of 6.5 mm were fabricated for the indices of 2.5, 2.7, 3.0, and 3.15, and the corresponding widths of the waveguides were 550 nm, 500 nm, 440 nm, and 375 nm, while the corresponding thicknesses were 383 nm, 386 nm, 337 nm, and 343 nm, similar to these used in our previous work [1]. Fully etched linearly apodized grating couplers (GC) were used to couple light in and out of waveguides, while 300 μm long tapers were used to adiabatically change the mode size [41]. Specifically, the following fabrication flow was utilized [1]: First, Si device layer was removed from silicon on insulator (SOI) substrates by a tetramethylammonium hydroxide (TMAH) wet etching such that only 3 μm of the buried oxide (BOX) was left on the top of the Si substrate (note that this step can be avoided if Si samples with only SiO_2 layer on the top are available). Then, a PECVD SRN thin film was deposited in an Oxford Plasmalab PECVD system, where the SiH_4 with N_2 precursor gases were used, with the chamber temperature set to 350 °C, and pressure to 650 mTorr. Next, e-beam lithography was implemented to expose a hydrogen silsesquioxane (HSQ) e-beam resist spun on SRN thin films. After HSQ development, the sample was etched in an Oxford Plasmalab P100 system, and HSQ was removed by 6:1 buffered oxide etch (BOE) solution mixed with de-ionized (DI) water in the ratio of 1:10. Finally, the samples were clad with 1 μm of

a PECVD SiO_2 deposited by the Oxford Plasmalab PECVD system. The cross-section of the device is demonstrated in Figure 2.4(b).

Table 2.1 summarizes some important parameters of our fabricated samples [1], including the SRN refractive index n_{srn}, the waveguide core width w, the waveguide core thickness d, the overlap integral estimated from Lumerical (Ansys) simulations Γ, the linear optical loss coefficient α measured by a cutback method, the GC coupling efficiency per one grating μ. It is worth noting that due to a change of an SRN refractive index it was necessary to adjust the geometry of a waveguide to maintain a consistent mode overlap integral. At the same time, changing the geometry of the waveguides may affect surface recombination, altering a free carrier lifetime. Therefore, the waveguide geometries of the samples were kept as similar as possible to minimize the effect on measurements when comparing data from samples with different indices.

Table 2.1: SRN waveguide and GC parameters for different samples used in the experiments.

n_{srn}	w [nm]	d [nm]	Γ	α [dB/cm]	μ [dB]
2.5	550	383	0.49	8	-6.8
2.7	500	386	0.51	16	-4.4
3	440	337	0.5	19	-4.9
3.15	375	343	0.42	21	-6

3.2 Experimental Results

Figure 2.5(a) demonstrates the dynamics of the transmitted optical pulses for the peak power of 21 dBm coupled to SRN waveguides. As evident in Figure 2.5(a), a sharp drop in transmitted power by about 80% and 50% is observed for sample indices of 3.15 and 2.7, respectively, indicating a strong nonlinear loss effect. Furthermore, the time-comb structure, following the long pulse, effectively sampled the recombination process with the comb pulses' amplitudes growing in time. Lastly, the carrier generation dynamics, captured by the long (200 ns) pulse from Figure 2.5(a), is presented on a shorter timescale in Figure 2.5(b) to demonstrate explicitly that most of the power transmission decline happens on the scale of 10 ns.

It is also worth noting that while the signal pulse distortion can be observed in Figure 2.4(d), it is deemed insignificant since its maximum amplitude variation is less than 10%, i.e. negligible compared to the amplitude decline caused by the nonlinear losses (i.e. 50% – 80% from Figure 2.5(a)). In a similar fashion, the EDFA-caused long pulse drop observed in Figure 2.4(c) does not contribute to the captured

dynamics significantly. Indeed, the total amplitude change is about 10% over 200 ns time-window of the pulse duration. However, within the scale of 10 ns where the nonlinear loss dynamics primarily occurs, the EDFA-caused amplitude change is only around 0.5%, which can be neglected with respect to the magnitude of the nonlinear losses. Therefore, based on the presented arguments, the generated optical pulse signal can indeed be used to accurately characterize transmission dynamics, thus enabling estimation of generation and recombination lifetimes with relatively high accuracy. Interestingly, we can see that the nonlinear loss dynamics presented in Figure 2.5(b) is much smoother for the SRN refractive index of 3.15 since it is mostly affected by the faster carrier generation dynamics, as evident by the sharper decline of the pulse transmission. Meanwhile, in the case of index 2.7, the carrier dynamics is clearly slower and is slightly affected by the signal pulse perturbations seen in Figure 2.4(d). This example also demonstrates why it was important to use longer waveguides and higher optical signal power, thus causing stronger nonlinear losses – namely to increase the accuracy of the measurements by minimizing the impact of the generated signal pulse deviation from an ideal boxcar function.

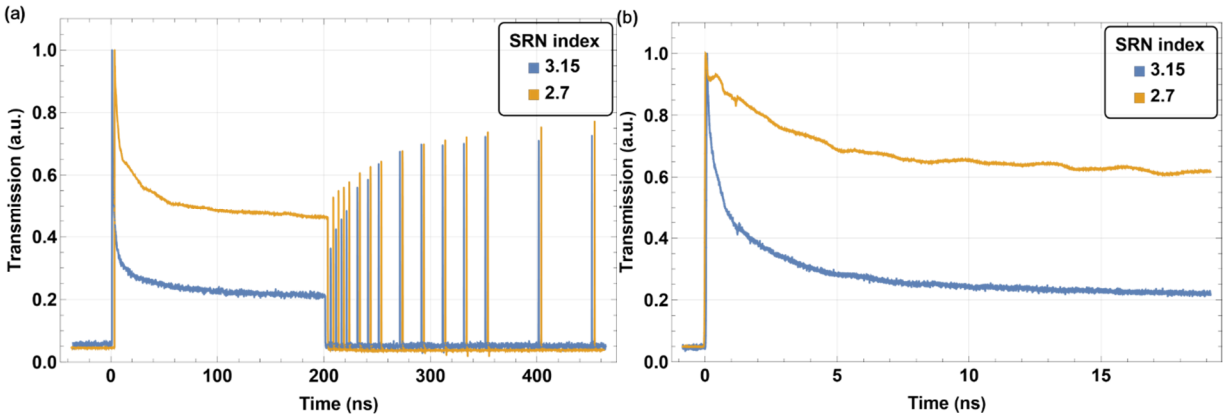

Figure 2.5: Optical pulse transmission dynamics in an SRN waveguide measured on the oscilloscope at the coupled peak power of around 21 dBm for the indices of 3.15 (blue) and 2.7 (orange), (a) Large timescale (500 ns) demonstrating a 200 ns pulse followed by a comb of short pulses, (b) short timescale (20 ns) demonstrating the front edge of the pulse affected by the nonlinear loss dynamics.

In principle, we can introduce the signal loss a (i.e. a reduction in transmission caused by the nonlinear loss) such that $a = 1 - T$, where T is the normalized signal transmission of the optical pulse signal, as shown, for example, in Figure 2.5(a). Then, the free carrier generation and recombination

lifetimes can be extracted from the captured transmission T or signal loss a dynamics assuming the underlying first order model:

$$\frac{dT_i}{dt} = \Delta T_i - \frac{T_i}{\tau_i} \tag{2}$$

$$\frac{da_i}{dt} = \Delta a_i - \frac{a_i}{\tau_i}, \tag{3}$$

where the indices $i = g$ or $i = rec$ refer to the generation or recombination dynamics, respectively, t is time, ΔT (or Δa) is the signal transmission (or loss) change rate, and τ is the carrier generation/recombination lifetime. Note that Equation (2)-(3), which are identical to that describing the free carrier concentration dynamics, have a straightforward solution:

$$T_i(t) = \Delta T_i \tau_i \left(1 - e^{-\frac{t}{\tau_i}}\right) \tag{4}$$

$$a_i(t) = \Delta a_i \tau_i \left(1 - e^{-\frac{t}{\tau_i}}\right) \tag{5}$$

It is worth noting that when considering carrier generation dynamics, it is more convenient to work with the signal loss dynamics which follows Equation (5), since in this case Δa_g acquires a physical meaning of a normalized signal loss rate (measured in s^{-1}), which is proportional to the free carrier concentration generation rate. At the same, the value τ_g is defined as the time it takes for the signal loss to reach the $a_{max}(1 - 1/e)$ level, where $a_{max} = \Delta a_g \tau_g$ is the maximum signal loss achieved in the limit $t \gg \tau_g$, as follows from Equation (5), and denotes the free carrier generation lifetime. Hence, the important parameters such as Δa_g and τ_g can be retrieved from fitting the signal loss dynamics, as shown in Figure 2.6(a). Likewise, Equation (4) allows estimation of the recombination lifetime τ_{rec}, although in our case the transmission dynamics of the time-comb is used for the parameter extraction instead. With that purpose, we measured the transmission peaks of each pulse from the time-comb and fitted them to the function described by Equation (4), as shown in Figure 2.6(b), to retrieve the recombination lifetime τ_{rec}.

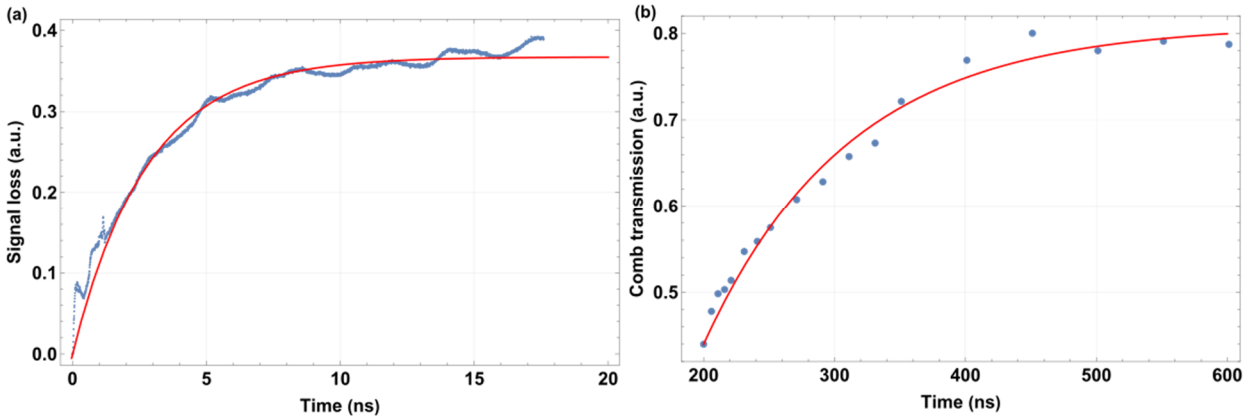

Figure 2.6: (a) Dynamics of signal loss a dynamics in an SRN waveguide caused by free carrier generation at the coupled peak power of around 21 dBm for the index of 2.7, fitted using Equation (5) in Wolfram Alpha, (b) transmission dynamics of the comb in an SRN waveguide demonstrating free carrier recombination dynamics at the coupled peak power of around 21 dBm for the index of 2.7, where dots represent the transmission peaks of each pulse in the comb, fitted using Equation (4) in Wolfram Alpha.

Figure 2.7(a) shows the signal loss rate Δa_g as a function of the pulse peak power (coupled to the waveguide) for various SRN indices extracted from the captured carrier dynamics. As can be seen in Figure 2.7(a), the signal loss rate increases with both the peak power and the SRN index. Specifically, the increase of signal loss rate Δa_g with power is recognized as linear, implying that the free carrier concentration is proportional to the incident optical power, as expected. Indeed, the linear relation suggests that the free carriers are not generated by TPA (which would lead to a quadratic dependence of free carrier concentration on power), but rather by defects in SRN. Likewise, Figure 2.7(b) shows free carrier generation lifetime τ_g as a function of the peak power and the SRN index, and we can observe that τ_g reduces with both parameters. Furthermore, the evolution of Δa_g and τ_g is necessarily correlated since the larger Δa_g depletes the propagating pulse at a faster rate, resulting in a reduction of τ_g. However, it is also reasonable to separate these quantities since they have a distinct physical meaning, as explained in the paragraph above. Overall, the shortest generation lifetime measured in our experiments is around 500 ps, and it was captured for the highest peak power of 24 dBm (coupled to the waveguide) for the sample with the refractive index of 3.15. More importantly, the last quoted value for the carrier lifetime is important since it strictly determines how short the pulses need to be in order to minimize (or avoid) the FCA dynamics and, therefore, the undesired nonlinear losses. Consequently, it can be concluded that for the index of 3.15, the nonlinear losses

significantly decrease for pulses shorter than 500 ps. Similarly, for the index of 2.7 and the peak power of 25 dBm, the pulse duration should be less than 2 ns to minimize the effects of FCA. Thus, a reduction in the SRN refractive index provides a dual advantage: it leads to a decrease in the magnitude of the nonlinear losses determined by Δa_g, and it also increases the maximum pulse duration that can be used without experiencing the nonlinear losses. However, as demonstrated in detail in [1], this trend, unfortunately, also leads to a steady reduction in the SRN optical nonlinear response, indicating a tradeoff between the nonlinearities and losses. For completeness, we also note that no nonlinear losses were observed for the SRN samples with the index of 2.5 (and, thus, the results are not presented here). Lastly, Equation (5) implies that the signal loss (or transmission) eventually reaches a steady state (i.e. saturation) at the value of $a_{max} = \Delta a_g \tau_g$, which can be observed when the incident pulse duration is much longer than the free carrier generation lifetime τ_g. For reference, the latter case is observed in Figure 2.5(a) for the 200 ns pulse. In other words, the saturation implies that the steady state is achieved in the carrier generation dynamics, with no further growth in the free carrier concentration. Therefore, the minimum transmission $1 - a_{max}$ at the saturation is an important parameter that describes the maximum nonlinear losses achieved in a steady state in both pulsed and CW excitation regimes. Hence, the minimum transmission was estimated from the measured free carrier generation dynamics, shown in Figure 2.5(a), as a function of the peak pulse power and presented in Figure 2.8(a). Evidently, we observed the minimum transmission of about -8 dB for the highest SRN index of 3.15 at the peak power of 24 dBm. The minimum steady-state transmission increases to the value of about -2 dB as the peak power is reduced to 12 dBm. Finally, we also point out that it is possible to reduce the transmission losses to just 1-3 dB by utilizing SRN waveguides with the index of 2.7 at the peak powers in the range of 14-25 dBm. Overall, the results align with the conclusions drawn in the preceding paragraph, indicating that a reduction in the SRN index correlates with a decrease in Δa_g.

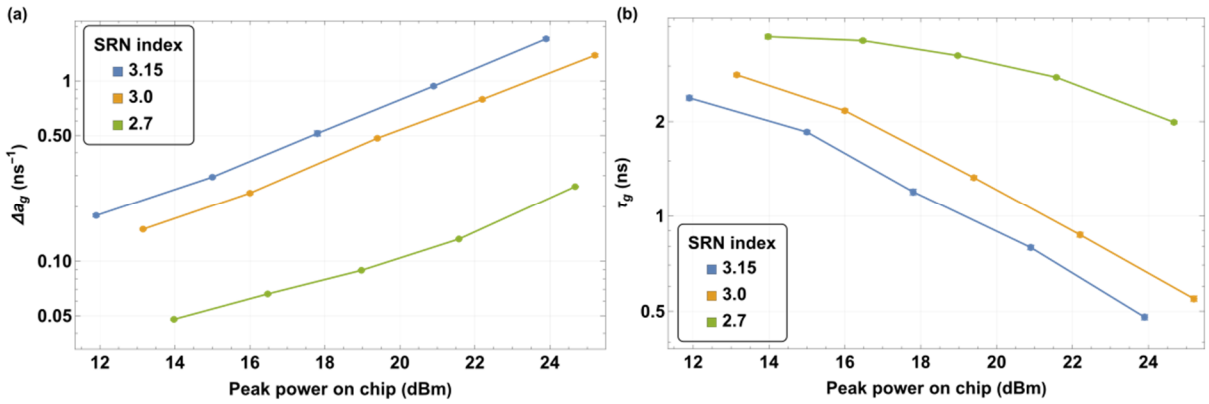

Figure 2.7: (a) Signal loss rate Δa_g as a function of a pulse peak power coupled to an SRN waveguide for the indices of 3.15 (blue), 3 (orange), 2.7 (green), (b) carrier generation lifetime τ_g as the function of pulse power coupled to an SRN waveguide for the indices of 3.15 (blue), 3 (orange), 2.7 (green). The error bars are obtained from fitting in Wolfram Alpha and are based on 95% confidence intervals.

Figure 2.8(b) demonstrates the recombination lifetimes τ_{rec} obtained from the fitting presented in Figure 2.6(b) for a set of varying refractive indices and pulse peak powers (coupled to the SRN waveguide). Remarkably, like in the case of the free carrier generation lifetime τ_g, increasing the refractive index of SRN leads to larger recombination lifetimes, which may indicate higher concentration of defects participating in the recombination. However, it is also important to note that the recombination lifetimes do not change with the peak power within the margins of errors, contrary to the case of carrier generation lifetimes, which indicates an absence of Auger recombination mechanism [28]. Overall, the largest recombination lifetime, which was measured in an SRN waveguide with the index of 2.7, is around (92±7) ns (averaged over 5 points representing different peak powers, where a margin of error represents a standard deviation error), while it is (39±3) ns and (31±2) ns for the indices of 3 and 3.15, respectively. We also note that the recombination lifetimes play an important role in optical pulse tailoring with the purpose of avoiding nonlinear losses. Indeed, as stated previously (and repeated here for completeness) the pulse repetition time ought to be longer than the sample recombination lifetime to allow the free carriers to recombine, prior to the arrival of the next pulse.

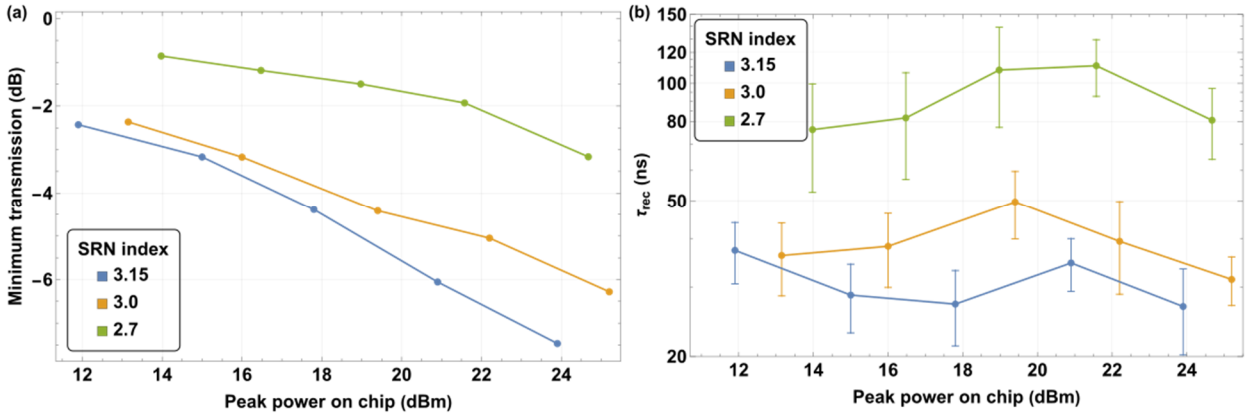

Figure 2.8: (a) Minimum transmission of the pulse as the function of pulse power coupled to an SRN waveguide for the indices of 3.15 (blue), 3 (orange), 2.7 (green), (b) recombination lifetime τ_{rec} as function of a pulse peak power coupled to an SRN waveguide for the indices of 3.15 (blue), 3 (orange), 2.7 (green).

Having determined the free carrier generation and recombination lifetimes, it was possible to optimize optical pulse's duration and repetition rate to minimize nonlinear optical losses. Indeed, one should expect that if the pulse duration is set to be shorter than τ_g, and the repetition period longer than τ_{rec}, free carriers dynamics will be unable to affect propagating optical pulses, as discussed above. In fact, with that purpose we measured the transmission of an optical pulse (with the repetition period of 2 μs, larger than τ_{rec}) in an SRN waveguide, with the index of 3.15 at the coupled peak power of 24 dBm, as a function of the pulse duration and presented the result in Figure 2.9(a). Note that the transmission was calculated as an energy of the transmitted pulse divided by the energy of the signal pulse coming from the EDFA, after which it was normalized by the maximum value (measured at 100 ps pulse duration). As expected, a sharp increase in the transmission is observed as the pulse gets shorter. For completeness, Figure 2.9(b) shows transmission of optical pulses for different pulse durations. As clearly demonstrated by the results in Figure 2.9(b), the part of the pulse, characterized by the sharp decline of amplitude (due to the FCA), can indeed be significantly shortened by decreasing the pulse duration, thus leaving only the part of the pulse least affected by the FCA. Hence, it enables utilization of high index SRN waveguides for certain applications where short optical pulses can be used, while avoiding the nonlinear losses and benefiting from the large optical nonlinearities of SRN [1].

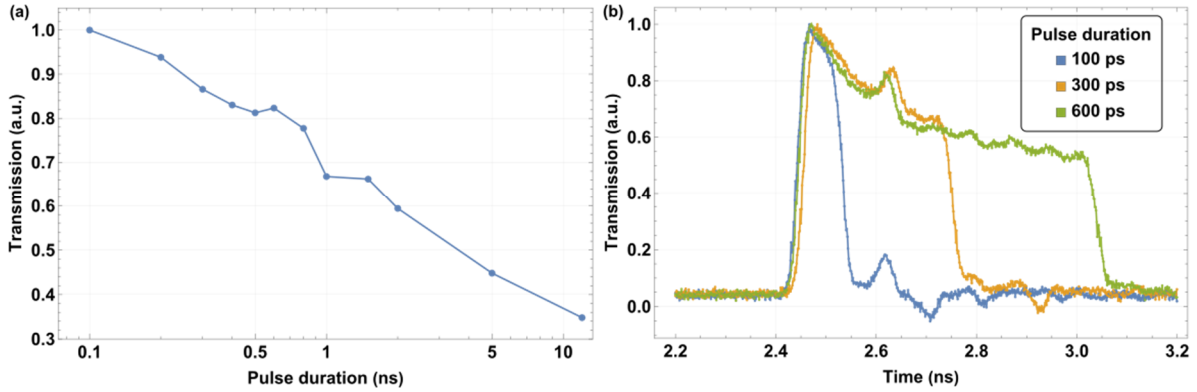

Figure 2.9: (a) Pulse transmission as a function of the pulse duration for SRN index of 3.15 and coupled peak power of 24 dBm, (b) pulse transmission dynamics for the pulse durations of 100 ps (blue), 300 ps (orange), 600 ps (green) for SRN index of 3.15 and coupled peak power of 24 dBm.

4. Discussion

In summary, we have provided compelling and detailed evidence that the observed nonlinear optical losses in SRN waveguides are attributed to FCA. Indeed, we observed photocurrent in SRN thin films with the refractive indices in the range of 2.65 - 3.15, which serves as a clear signature of the generated free carriers, and determined that it increases with the SRN refractive index. Similarly, we established that the nonlinear optical losses observed in SRN waveguides, within a comparable range of the refractive indices, also increase with the refractive index. On the other hand, negligible photocurrent in the SRN thin films and absence of nonlinear losses in the corresponding waveguides were observed for the index of 2.5, clearly indicating the absence of free carriers in this case. The aforementioned set of circumstances strongly supports the hypothesis that the photocurrent and the nonlinear losses indeed have the same origin – namely the generated free carriers. Furthermore, it is evident that the free carriers are not generated by TPA, since the last was not observed at the optical powers used in this work [1]. Additionally, it was found that the signal loss rate Δa_g, which is proportional to the free carrier generation rate, grows linearly with the optical pulse peak power, as in the case when defects generate free carriers. We, therefore, conclude that various defects and/or impurities present in SRN films with a large refractive index facilitate both the free carrier generation and recombination processes. Moreover, based on the FCA dynamics observed in SRN waveguides, we determined that both free carrier generation and recombination lifetimes decrease with the

refractive index of SRN samples, stemming from the associated increase of the defect density in SRN samples with higher refractive indices. Specifically, the free carrier recombination lifetimes of (92±7) ns, (39±3) ns, and (31±2) ns were estimated for the SRN indices of 2.7, 3 and 3.15, respectively. Notably, voltage breakdown was observed in an SRN thin film for the highest index of 3.15 at a relatively low DC electric field of around 20 V μm^{-1}, and it can be explained by the presence of a high defect density in the SRN film [42, 43, 44]. On the other hand, a noticeable reduction of the photocurrent was observed in the SRN thin film after RTA at 800 °C for 2 min, compared to the as-grown SRN thin film under the same conditions. We, therefore, hypothesize that it indicates the increased incorporation of defects and impurities in as-grown SRN films, owing to the prior ample evidence that RTA reduces defect density [30, 31, 32]. Nonetheless, it ought to be stated that while the origin of the observed nonlinear losses is FCA caused by the defects, the origin of the defects has not been established directly, indicating that further research is needed. Finally, and perhaps most importantly, we have demonstrated that it is possible to reduce or avoid nonlinear optical losses in SRN waveguides altogether by utilizing optical pulses shorter than the free carrier generation lifetime while maintaining a repetition period of the pulses longer than the free carrier recombination lifetime. Consequently, the presented results strictly delineate the conditions for taking full advantage of the large nonlinearities in high index SRN ($\chi_3 = (12.6 \pm 1.4) \times 10^{-19}$ m^2V^{-2} corresponding to the SRN index of 3.2 [1]), leading to its efficient application in nonlinear optics. In the future, we plan to investigate other methods to reduce nonlinear losses, determine the origin of defects responsible for free carrier generation and recombination, and research the spectral response of nonlinear losses to further enhance our understanding of the SRN platform.

Acknowledgements

Chapter 2, in part, is a reprint of the material published in Advanced Optical Materials. The dissertation author was the first author of this paper, with co-authors Yeshaiahu Fainman, Andrew Grieco, and Nikola Alic.

CHAPTER 3 - LARGE BIDIRECTIONAL REFRACTIVE INDEX CHANGE IN SILICON-RICH NITRIDE VIA VISIBLE LIGHT TRIMMING

1. Introduction

Silicon-rich nitride (SRN) grown using plasma-enhanced chemical vapor deposition (PECVD) has numerous qualities that are outstanding for a versatile complementary metal-oxide semiconductor (CMOS) compatible integrated photonics platform. As the Si content (and with it – the refractive index) of SRN films vary with the choice of PECVD deposition and post-processing parameters, films can be grown with a refractive index (as measured at 1550 nm) ranging from ~2.0 (lower Si content: Si_3N_4) to ~3.2 (higher Si content: Si_7N_3)[1,2]. Furthermore, other linear and nonlinear optical properties of SRN are also altered remarkably with the change of silicon content, including linear optical losses and transparency window[2], nonlinear optical losses[1,3], thermo-optic coefficient[4], and third-order susceptibility ($\chi^{(3)}$)[1,5]. Consequently, control of these properties enables SRN films to be optimized for various applications. For example, a wide variety of nonlinear effects have been demonstrated in SRN devices, such as the DC Kerr effect[6], nonlinear Kerr switching[7], second harmonic generation[8], intermodal frequency generation[9], four-wave mixing[5], and supercontinuum generation [10]. Additionally, SRN's relatively high thermo-optic coefficient (especially for higher Si-content films) enables implementation of efficient thermally driven phase shifters and switches[11,12]. Finally, SRN is substantially more compatible with traditional CMOS mass-manufacturing process than other materials, such as LPCVD Si_xN_y, since the relatively low temperature of PECVD SRN deposition (~350 °C) does not exceed the thermal budget of front-end-of-the-line semiconductor processes[2].

On the other hand, fabrication variability continues to represent a persistent challenge in integrated photonics, including SRN integrated platform. In particular, phase-sensitive devices, such as micro-ring resonators (MRRs), are highly sensitive to variations in the fabrication process even on the scale of 1 nm, which can lead to significant performance inconsistencies, ultimately precluding these devices from commercial and widespread use[13,14]. These random variations typically require optical devices to be biased to operating specifications using power-demanding heaters[15]. Alternatively, optical trimming, which is fine

tuning of the optical properties of photonic devices post-fabrication, has been employed to compensate for such variations. However, most presented trimming methods either induce unidirectional refractive index change only, or suffer from strong relaxation, or require CMOS-incompatible materials as cladding, limiting their effectiveness.

It has been well-known for nearly half a century that optical materials exposure to high-intensity visible or UV light can alter their optical properties[16]. As such, some of the first approaches to trimming integrated photonic devices used UV exposure to silane-based waveguide cladding — and soon after, Si_xN_y waveguide cores — to substantially shift the center wavelengths of filters and ring resonators[17,18]. In the time since, a wide variety of methods and optical materials have been proposed to trim optical properties of integrated components, including further developments of CW UV and visible light exposure[19-22], pulsed laser irradiation[23], electron beam exposure[24,25], and localized annealing of regions exposed to ion implantation[26-31]. These methods can introduce waveguide effective index changes on the order of 10^{-3} to 10^{-2}, which is sufficient for many applications[26,30]. However, several of these methods require exotic non-CMOS-compatible materials to sensitize the optical structure to the applied stimulus, such as chalcogenides, phase change materials, tunable polymers, and liquid crystals[17,19,21,32]. Other methods require trimming to be performed on waveguides prior to the application of the final cladding, necessitating the use of temporary cladding and adding complexity to the trimming process[33]. Recently, simple CMOS-compatible post-fabrication trimming of structures has been demonstrated using localized annealing from on-chip heaters included in the chip design[26-31]. While this method is simple and effective, it requires Ge implantation of the waveguide and is capable only of decreasing the refractive index of the optical material. In fact, most of those mentioned above techniques are not capable of post-fabrication trimming in both directions.

In this manuscript, we present extensive and novel results on visible radiation (405 nm and 520 nm) induced bidirectional trimming of PECVD SRN with refractive indices of 2.4 and 2.9 (at 1550 nm). Refractive index tuning is accomplished in a simple and cost-effective setup that allows rapid fine trimming

via real-time position tracking of resonance in an MRR. Remarkably, both 405 nm and 520 nm radiation can induce blue and red wavelength resonance shifts in an SRN MRR. The latter implies that a refractive index of SRN can be both decreased and increased by using a single laser-source, which is undoubtedly a highly advantageous feature for the trimming of SRN devices. Furthermore, the blue and red shifts can be easily separated in a fully controllable way simply by changing the trimming laser power or the exposure duration. Moreover, a strong blue shift of 10.6 nm and a largest ever reported red shift of 49.1 nm are achieved in trimmed SRN MRRs. In addition, the refractive index can be decreased by 2×10^{-2} and increased by a record value of 0.11. We demonstrate that both blue and red shifts originate from thermal annealing, with blue shifts occurring at lower annealing temperatures (400 °C – 500 °C) and red shifts emerging at temperatures above 500 °C – 600 °C. Intriguingly, the magnitude and direction of the shifts vary significantly with the refractive index of SRN, which makes the material an excellent choice for coating. Additionally, it is established that the presence of both red and blue shifts mitigates the resonance backshifting by pushing the resonance in opposite directions. Finally, we demonstrate the effectiveness of the novel technique employing it for trimming of an SRN-based optical demultiplexer with MRRs to an accuracy of approximately 10 pm. Overall, our results suggest that SRN is a highly reconfigurable CMOS-compatible platform, which offers a pathway toward significantly improving the precision and manufacturability of SRN (or Si if SRN is used as coating) photonic devices, particularly for phase-sensitive applications where sub-nanometer tuning accuracy is required.

2. Results

2.1 Experimental setup

To investigate the effects of visible light exposure on SRN waveguides, we deposited SRN films with refractive indices of 2.4 and 2.9 (measured at 1550 nm) using plasma-enhanced chemical vapor deposition (PECVD). For the waveguide with a refractive index of 2.4, the width and thickness were 600 nm and 385 nm, respectively; for the waveguide with an index of 2.9, they were 450 nm and 340 nm. The fabricated micro-ring resonators (MRRs) had a radius of 25 μm, with a coupler length of 6.5 μm, yielding

a total length of approximately 170 µm. The gap between a bus waveguide and a coupler was 400 nm. Fig. 3.1a demonstrates a microscope image of the fabricated device used for trimming experiments.

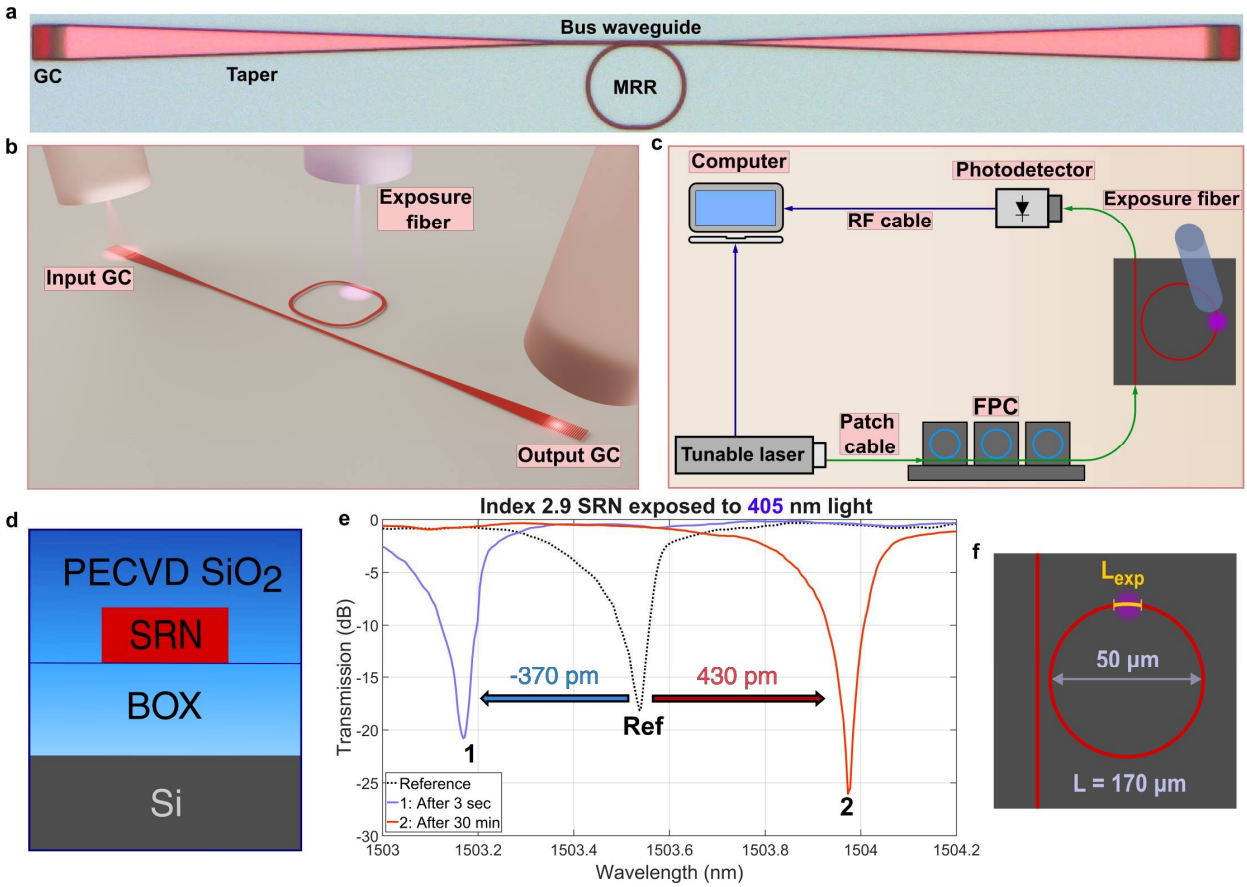

Figure 3.1: (a) Microscope image of a device to be trimmed showing an MRR, bus waveguide, grating couplers (GC), tapers. (b) 3D illustration of the configuration of 3 fibers used for trimming and real-time measurement. Laser light couples in and out via grating couplers. The exposure fiber is centered over a section of an MRR. (c) Block-diagram of the setup showing the equipment used in experiments. Here FPC is fiber polarization controllers used to set transverse electric (TE) polarization. Blue arrows denote RF cables, while the green ones – fiber patch cables. (d) Cross-section of a waveguide used in experiments. Here BOX is buried oxide. (e) Transmission spectra of the probing signal in SRN MRRs after exposure to 405 nm light. The dotted black curve indicates the initial position of resonance (reference). The numbers (and "Ref") next to the resonances indicate the order in which the spectra were measured (starting with "Ref"). The labels describe exposure time. (f) Image of MRR showing how its section is exposed (violet circle), the MRR diameter is 50 µm, and ring length (L) is 170 µm. The length of one exposed section is L_{exp}.

Fig. 3.1b and 1c demonstrate the setup used for the trimming experiments. The goal was to achieve a strong MRR resonance shift and fine-tuning in real time as the visible laser exposure was applied, while maintaining a simple and cost-effective setup. For this, we used inexpensive fiber-coupled multimode

(MM) 405 nm and 520 nm laser diodes (Laser Tree LT-FCLD-M405075 and LT-FCLD-M520065) coupled to SMF-28 patch cables. The bare fiber tip, cleaned and cleaved, was angled at 10 degrees relative to the sample to minimize back reflections. The fiber was attached to the grating coupler stage which had six degrees of freedom, enabling precise alignment, with an accuracy of 500 nm (more details on how high accuracy alignment was achieved can be found in Supplementary information, section S1). The trimming resolution (that is the minimum feature size that can be exposed) in this setup was 10 μm, primarily limited by the beam size of the trimming light. While the SMF-28 patch cable was not optimized for 405 nm or 520 nm light, we found it suitable, with transmission losses of only 0.7 dB. No degradation in cable or laser performance was observed, even at maximum power of 16.4 dBm used in the experiments.

Fig. 3.1c demonstrates a block-diagram of the setup used in the experiments. To monitor the trimming-induced resonance shift in real time, light from an Agilent 81980A tunable continuous-wave laser (1465 nm – 1575 nm) was coupled into the SRN samples (cross-section is shown in Fig. 3.1d) using grating couplers. Polarization controllers were used to set polarization to transverse electromagnetic (TE) mode, and the output light was measured by a photodetector (model).

Fig. 3.1e exemplifies the measured transmission spectra of the probing signal in SRN MRRs when a section of an MRR was exposed to 405 nm (as illustrated in Fig. 3.1f; also see Supplementary information, section S2, for more results). The results confirm that it is indeed possible to achieve both red and blue resonance shifts using a single laser source. A blue shift was observed within a few seconds of exposure while the red shift took up to 30 minutes to saturate. These results demonstrate the ability to clearly separate blue and red shifts by varying the duration of exposure, a crucial property for trimming applications.

2.2 Dynamics and power dependence of SRN refractive index change

This section systematically analyzes how key parameters — such as a refractive index of (n_{srn}), exposure wavelength (λ_{exp}), optical power of exposure (P_{exp}), exposure duration (t_{exp}) — affect the trimming process. Specifically, we exposed SRN MRRs with refractive indices n_{srn} of 2.4 and 2.9 to visible radiation wavelengths of 405 nm (violet) and 520 nm (green).

The presence of both blue and red resonance shifts in MRRs demonstrates that the effective index of SRN waveguides n_{eff} can be both decreased and increased using either 405 nm or 520 nm lasers. The refractive index change is proportional to the resonance wavelength shift, as shown in Eqs. (1-3) [34, 35]:

$$\Delta n_{eff} = n_g \frac{\Delta\lambda_{res}}{\lambda_{res}} \cdot \frac{L}{L_{exp}} \tag{1}$$

$$n_g = \frac{\lambda_{res}^2}{FSR \cdot L} \tag{2}$$

$$L_{exp} = \frac{\Delta\lambda_{sec}}{\Delta\lambda_{ring}} L \tag{3}$$

Here Δn_{eff} is the change of the effective index n_{eff} in an SRN waveguide, n_g is the group index, λ_{res} is the resonance wavelength of an MRR, $\Delta\lambda_{res}$ is the resonance wavelength shift in an MRR, *FSR* is a free spectral range of an MRR, $\Delta\lambda_{ring}$ is the resonance wavelength shift when the whole MRR is exposed, $\Delta\lambda_{sec}$ is the resonance wavelength shift when only one section of the MRR is exposed, L_{exp} is the length of the single exposed section (see Fig. 3.1f), L is the length of the MRR. Additionally, to estimate a refractive index change Δn_{srn}, we performed simulations in Lumerical to calculate what refractive index change Δn_{srn} is required to cause the corresponding effective index change Δn_{eff}. Based on Eqs. (1-3), and the resonance shift from MRRs transmission spectra (like in Fig.3.1e, also see Fig. 3.S2), we estimated the refractive index changes. It is worth noting that L_{exp} of 10 μm was estimated experimentally (see next section) and used in Eqs. (1-3).

First, we investigate the SRN refractive index change dynamics measured in MRRs exposed to 405 nm and 520 nm light (Fig. 3.2a, 3.2b). Only one section of an MRR was exposed in each experiment, as shown in Fig. 3.1f. In Fig. 3.2a, we observe the refractive index change in an SRN MRR with $n_{srn} = 2.9$ as a function of exposure time for 405 nm and 520 nm light. Focusing on the 405 nm case, the blue shift (due to refractive index decrease) saturates in approximately 5 seconds, while the red shift (due to refractive index increase) fully compensates for the blue shift in about 200 seconds when exposed to 405 nm light. In

contrast, the red shift takes approximately 30 minutes to saturate. Meanwhile, both the blue and red shifts induced by the 520 nm laser follow a similar pattern, though they take slightly longer to saturate compared to the 405 nm laser. Also, stronger blue shift can be observed when induced by 520 nm laser, while strong red shift can be observed when induced by 405 nm laser (for the same power of exposure).

Similarly, Fig. 3.2b illustrates the refractive index change in an SRN MRR with n_{srn} = 2.4 as a function of exposure time for 405 nm and 520 nm light. This time, the difference in dynamics between the two lasers is more evident. Notably, no blue shift is observed within the first second of exposure to 405 nm light, unlike with the 520 nm laser. Additionally, a stronger red shift can be seen when an SRN MRR is exposed to 405 nm light.

The complex behavior of SRN trimming originates from the thermal annealing mechanism driving the refractive index change. We found that lower temperature annealing (400 °C – 500 °C) leads to a decrease in refractive index, while annealing at temperatures above 500 °C – 600 °C results in an increase. Notably, the refractive index reduction is significantly smaller in SRN with an index of 2.4 compared to SRN with an index of 2.9, and that agrees well with the results shown in Figs. 3.2c and 3.2d, where it is evident that the blue shift is noticeably weaker in index 2.4 SRN. Greater details and discussion are provided in the Supplementary information, section S3. Also, in Supplementary information, section S6, we demonstrate that neither PECVD SiO_2 nor residual HSQ contribute to the permanent shifts observed in SRN MRRs.

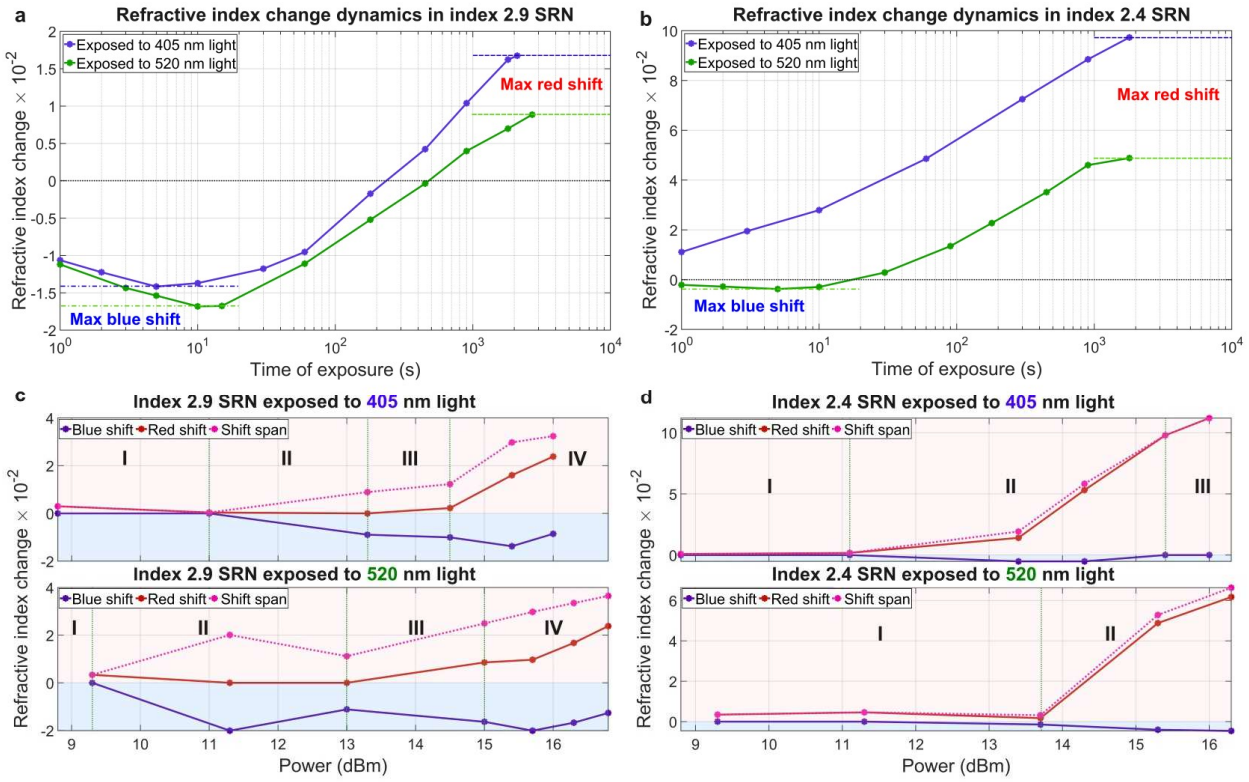

Figure 3.2: Dynamics of resonance shift in an SRN MRR when (a) $n_{srn} = 2.9$, and (b) $n_{srn} = 2.4$. The exposure power $P_{exp} \approx 15.5$ dBm; the violet curve represents exposure to 405 nm light, and the green – to 520 nm light; the dotted black line indicates no refractive index change. Refractive index change of SRN as a function of exposure power when (c) $n_{srn} = 2.9$ and (d) $n_{srn} = 2.4$; the upper plots represent the case when the exposure was done with the 405 nm laser, and the bottom ones – with the 520 nm laser; red and blue areas mark positive and negative refractive index changes, respectively.

It was also of great interest to investigate how exposure power affects direction of the shifts (or refractive index change) and their magnitude. Fig. 3.2c and Fig. 3.2d show the refractive index change in SRN measured in MRRs exposed to 405 nm and 520 nm light as a function of exposure power.

Based on Fig. 3.2c, overall, we indicate 4 different sections with distinct dynamics (I – IV). In section I, at the lowest exposure powers, we observe only weak red shift, and no blue shift. As power increases, in section II, no red shift can be observed, although noticeable blue shift can be visible. It takes 10 min – 30 min for the blue shift to saturate. As the exposure power continues to increase, in section III, aside from a strong blue shift, the onset of the red shift can be seen. The red shift takes over only after the blue shift saturates (after about 5 min – 15 min), and it takes the red shift about 30 min to saturate. Therefore, it is possible to separate the directions of the shifts by time of exposure, although the red shift is much

weaker since both red and blue shifts partially compensate each other. Finally, section IV reveals that both strong blue and red shifts are possible. In noticeable contrast to section III, the red shift is much stronger, although it still takes around 30 min to saturate. The blue shift, however, dominates first and takes a few seconds only to saturate, which can also be seen from Fig. 3.2a. Therefore, it can easily be separated from the slower red shift, which results in both strong red and blue shifts, which is favorable for bidirectional trimming. Overall, a maximum refractive index increase of 2.4×10^{-2} was observed with exposure to either the 405 nm or 520 nm laser, while the greatest decrease, -2×10^{-2}, occurred with 520 nm laser exposure.

Fig. 3.2d shows a different trimming behavior for $n_{srn} = 2.4$. This time up to 3 different sections can be highlighted. The first section I, which corresponds to the lowest exposure powers, indicates only weak red shifts. With the increase of exposure power, in section II, we can first observe a weak blue shift which takes a few seconds to saturate, followed by a strong red shift, which in turn takes around 30 min to saturate. In case of exposure to 405 nm light, we also indicate section III where no blue shift could be observed, although a much stronger red shift can be seen. Remarkably, the maximum refractive index increase was 0.11, the largest ever reported, which indicates a great potential of this material for trimming. Meanwhile, the largest refractive index decrease was only -0.5×10^{-3} for both wavelengths of exposure.

We discuss the observed trend in greater detail in Supplementary information, section S4, where we conclude that thermal annealing explains the observed behavior. Specifically, a laser beam has a non-uniform distribution of power, which results in a temperature gradient within a section of an MRR. The sections of the ring heated to 350 C – 550 C induce the blue shifts, while the sections heated above 550 C – the red shifts. Here we also briefly report that in case of index 2.9, 520 nm light is favored for bidirectional trimming since it causes lower temperature gradient in a SRN waveguide, which results in a stronger blue shift (see Supplementary information, section S4), while a stronger red shift can be achieved by simply increasing exposure power. Meanwhile, 405 nm is preferred when trimming $n_{srn} = 2.4$ SRN MRRs since it causes a stronger red shift due to larger absorption and heating.

In summary, this complex behavior offers significant advantages for trimming. Both the direction and magnitude of the shifts, as well as the shift rates, can be finely tuned by adjusting the laser power, allowing higher power for coarse trimming and lower power for fine-tuning. This offers significant flexibility for trimming applications, depending on the specific requirements from a photonic device.

2.3 Maximizing resonance shift

In the previous section we established that significant refractive index changes in both directions are possible. Therefore, in this section we aim to maximize the resonance shifts, and so we exposed the whole length of SRN MRRs to both 405 nm and 520 nm lasers. Fig. 3.3a and Fig. 3.3b exemplify the measured resonance shifts in SRN MRRs during exposure. Fig. 3.3c demonstrates how resonances shift in the case of blue shift from Fig 3.3a. Meanwhile, Fig. 3.3d and Fig. 3.3e provide illustrations which demonstrate that the whole ring was exposed by steps. Specifically, the ring was split into even sections separated by the arc length L_{step}. Another parameter, L_{exp}, is the length of the exposed section of the ring, limited by a beam size. Given that the length of the ring was 170 μm, and the number of exposed sections was 18 – 30, based on Fig. 3.3a and Fig. 3.3b, L_{step} was in a range of 5.5 μm – 9.5 μm.

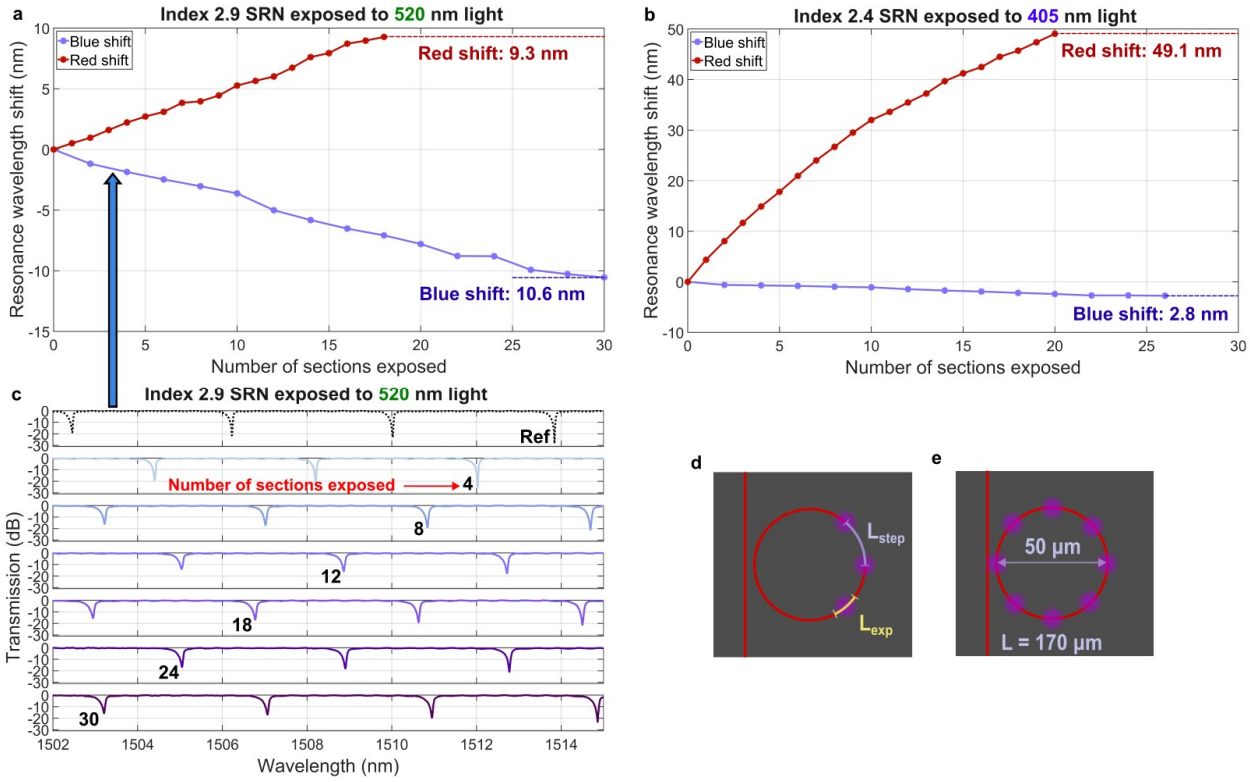

Figure 3.3: Resonance wavelength shifts in SRN MRRs exposed to (a) 16.7 dBm of 520 nm light when n_{srn} = 2.9 and (b) 16.0 dBm of 405 nm light when n_{srn} = 2.4. (c) Transmission spectra of the probing signal in SRN MRR for the case of blue shift from Fig. 3.3a. The dotted black curve indicates the initial position of a resonance (reference). The numbers next to the resonances indicate the number of sections exposed. (d) Illustration of how L_{exp} and L_{step} are defined. (e) Illustration of how the whole ring was exposed, where L_{step} varied in a range of 5.5 µm – 9.5 µm based on number of sections exposed.

From Fig. 3.3a, we observe a large blue shift of 10.6 nm and a red shift of 9.3 nm in index 2.9 SRN when exposed to 520 nm light. Meanwhile, from Fig. 3.3b, a lower blue shift of 2.8 nm and the largest ever reported red shift of 49.1 nm were achieved in index 2.4 SRN when exposed to 405 nm light. Notably, blue shifts were saturated while the red shifts were not since each section of the MRR was exposed only for 10 min to expedite trimming process (it takes around 30 min for the red shift to saturate). Therefore, we conclude that the red shift can be even stronger.

It is worth noting that depth of resonances changes after exposure, as apparent from Fig. 3.3c. It is caused by change in transmission coefficient of a coupler section of a ring and increase in optical losses. The latter is due to scattering losses stemming from non-uniform refractive index profile caused by stepped

exposures (Fig. 3.3e). We demonstrated that a significant reduction in losses is possible if the ring is exposed more uniformly, and provided greater details in Supplementary information, section S5.

We can estimate the maximum resonance shift possible to achieve by using Eqs. (1-3) when the whole ring is exposed to saturation. First, we need to determine L_{exp} from Eq. 3, and for that we need to measure the resonance shift $\Delta\lambda_{sec}$ when only one section is exposed (Fig. 3.1f), and $\Delta\lambda_{ring}$ when the whole ring is exposed (Fig. 3.3d). Since the maximum blue shift of $\Delta\lambda_{ring}$ = 10.6 nm was measured in the case when n_{srn} = 2.9, λ_{exp} = 520 nm (Fig. 3.3a), and $\Delta\lambda_{sec}$ = 540 pm blue shift was observed when only one section of the ring was exposed (Fig. 3.S2b), it was possible to estimate the exposure length: $L_{exp} \approx 10$ μm. Now it is possible to estimate $\Delta\lambda_{ring}$ since $\Delta\lambda_{sec}$ is known. For example, when n_{srn} = 2.4, λ_{exp} = 405 nm, we determined that $\Delta\lambda_{sec}$ = 3900 pm (Fig. 3.S2c), and so $\Delta\lambda_{ring}$ = 66.3 nm. Both demonstrated $\Delta\lambda_{ring}$ = 49.1 nm and estimated $\Delta\lambda_{ring}$ = 66.3 nm are record high, proving that SRN can be trimmed in a very high range.

Table 3.1 summarizes the estimated maximum resonance shifts possible when the whole ring is exposed to saturation. We used the best results from Fig. 3.2c and Fig. 3.2d, where we measured refractive index changes for different exposure powers. The shift span is achieved by subtracting $\Delta\lambda_{ring}$ for blue shift from $\Delta\lambda_{ring}$ for red shift.

Table 3.1: Maximum estimated resonance shifts $\Delta\lambda_{ring}$ when the whole ring is exposed. The measured values are marked by an asterisk.

	n_{srn} = 2.4, λ_{exp} = 405 nm	n_{srn} = 2.4, λ_{exp} = 520 nm	n_{srn} = 2.9, λ_{exp} = 405 nm	n_{srn} = 2.9, λ_{exp} = 520 nm
$\Delta\lambda_{ring}$ (nm), red shift	66.3	36.6	10.9	10.9
$\Delta\lambda_{ring}$ (nm), blue shift	3.1	2.7	6.1[1]	10.6[1]
$\Delta\lambda_{ring}$ (nm), shift span	69.4	39.3	17	21.5

[1]Measured value.

As can be seen in Table 1, overall, n_{srn} = 2.4 SRN yields a much larger range of trimming than n_{srn} = 2.9 SRN, although the blue shift is much weaker. In contrast, in case of n_{srn} = 2.9 SRN, the blue shift can be as strong as 10.6 nm when SRN is trimmed by the 520 nm laser, which favors bidirectional trimming. Therefore, there is a tradeoff between these two cases.

We also provide Table 3.2, which summarizes our results and compares them with those of other research groups. We focus on the best results achieved in our work and demonstrated elsewhere for any trimming method.

Table 3.2. Summary of our experimental results compared to the results from other research groups, sorted by the resonance wavelength shift, $\Delta\lambda$.

Ref.	$\Delta\lambda$ (nm), span	$\Delta\lambda$ (nm), blue & red shift	$\Delta n_{srn}\times10^{-2}$, blue & red shift	CMOS-compatible?	Material	Method
25	2.5	-2.5	-	No	Chromophore-doped polymer cladding	Exposure to e-beam
26	3	-1 & 2	-0.4 & 0.8	No[1]	HSQ cladding	Laser annealing
24	4.9	4.9	-	Yes	SiO_2 cladding	Exposure to e-beam
19	6.7	6.7	4.8	No	As_2S_3 cladding	Illumination with halogen lamp
36	7	-7	-	Yes	Si core implanted with Ge ions	Laser annealing
37	7	-7	-0.7	Yes	Nitrogen-rich SiN core	Exposure to 244 nm light
35	8	-8	-	Yes	a-Si core	Exposure to 405 nm light
22	8.7	-8.7	-	Yes	c-Si core	Oxidizing by 532 CW laser
17	9.7	-9.7	-7.5	No	Polysilane cladding	Exposure to 370 nm light
18	12.1	-12.1	-1.3	Yes	SiN core	Exposure to 244 nm light
23	16	-10.5 & 5.5	-	Yes	c-Si core	Amorphization and ablation by 400 nm femtosecond laser
This work	19.9	-10.6 & 9.3	-2 & 2.4	Yes	Index 2.9 SRN core	Annealing by 405 nm and 520 nm light
This work	51.9	-2.8 & 49.1	-0.5 & 11.2	Yes	Index 2.4 SRN core	Annealing by 405 nm and 520 nm light

[1]When used as a cladding due to instability caused by change in humidity[26].

While numerous groups have successfully achieved strong blue shifts, inducing a substantial red shift has proven particularly challenging. The largest red shift reported so far, 6.7 nm, required a CMOS-incompatible chalcogenide cladding[19]. In contrast, our work demonstrates nearly an order of magnitude improvement in refractive index using SRN with a refractive index of 2.4. Furthermore, most studies report only unidirectional resonance shifts, with few exceptions. For instance, a bidirectional shift was achieved

using HSQ cladding[26]; however, this approach suffered from significant backshifting due to moisture absorption[26]. Alternatively, bidirectional shifts in crystalline silicon (c-Si) have been demonstrated via ablation and amorphization using a 400 nm femtosecond laser (second harmonic of a Ti:Sa laser)[23]. This method, however, entails considerably higher trimming costs, limits precision, and was only demonstrated in uncladded samples[23], raising concerns about its compatibility with cladded devices. In summary, the bidirectional tuning capability, record-breaking red shift, CMOS-compatibility, and precise, cost-effective trimming achieved in SRN clearly underscore its exceptional performance.

2.4 Resonance backshifting in index 2.9 SRN MRRs

It is known that the resonance shift induced by trimming may drift over time[26]. Therefore, it was important to assess the stability of both red and blue shifts in our case. Fig. 3.4 displays the MRR resonance wavelength shift tracked over several days after exposure. In this work, we define backshifting as the resonance shift of an MRR moving in the direction opposite to the initial tuning shift. Conversely, forward shifting describes resonance movement continuing along the original shift direction.

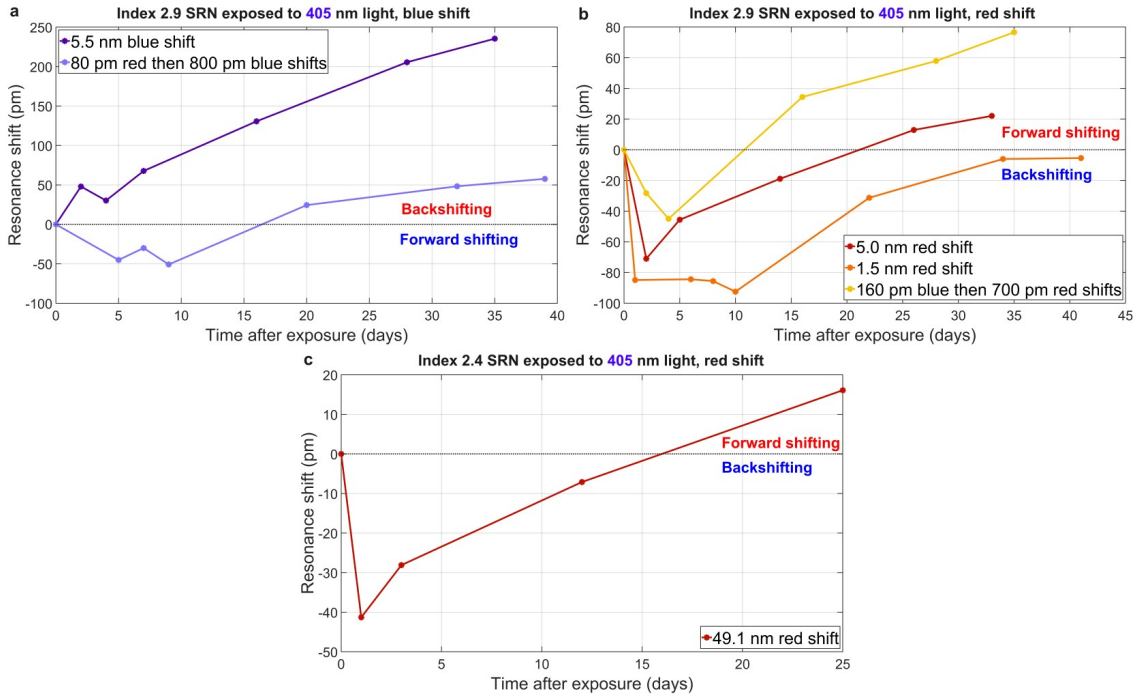

Figure 3.4: Resonant wavelength shift as a function of time after exposure when MRRs are exposed to 405 nm light in case of (a) a blue shift, $n_{srn} = 2.9$, (b) a red shift, $n_{srn} = 2.9$, (c) a red shift, $n_{srn} = 2.4$. The dotted black line separates the areas of forward shifting and backshifting.

In Fig. 3.4a, a backshift (red shift in this case) of 240 pm was observed 35 days after exposure of the MRR where an initial blue shift of 5.5 nm was induced. This result aligns with previous reports, where long-term backshifting is commonly observed after trimming[26]. However, the backshift is considerably smaller than the initial 5.5 nm shift, making wide-range trimming approach suitable for applications where accuracy within approximately 200 pm is acceptable.

Additionally, in one case where an initial 80 pm red shift was followed by an 800 pm blue shift, a forward shift was observed within the first 10 days instead of the expected backshift. This suggests that the red shift dominated the early back-shifting process immediately after exposure. Over time, however, the blue shift prevailed, causing the resonance to shift in the opposite direction. This behavior suggests that red shifts tend to dominate shortly after exposure, while blue shifts have a more pronounced long-term influence.

To further support this, in another example, shown in Fig. 3.4b, where a 1.5 nm red shift was initially induced, the resonance first back-shifted within the first 10 days, after which it reversed the direction of shifting, and gradually returned close to its original position over 41 days. Similar dynamics was observed when the initial shift was 5.0 nm, where resonance returned close to its initial position after 33 days. This demonstrates that, under certain conditions, resonance backshifting can be almost fully mitigated when a balance between red and blue shifts is achieved.

In addition, we also provide an example where a resonance was first blue-shifted by 160 pm, followed by a 700 pm red shift. In this case, the blue shift eventually prevailed, forward shifting the resonance by 80 pm without signs of saturation. This suggests that excessive blue shift may still cause significant (forward) shifts even after a red shift is induced post-exposure.

Finally, Fig. 3.4c demonstrates that resonance relaxation dynamics at $n_{srn} = 2.4$ is similar to that at $n_{srn} = 2.9$. Notably, the observed instability was under 100 pm, despite an initial large red shift of 49.1 nm — highlighting the exceptional stability and suitability of SRN for trimming applications.

In conclusion, red and blue shifts coexist and drive resonance shifts in opposite directions, but they follow distinct dynamic patterns. Red shifts dominate within the first 3-10 days, while blue shifts tend to take over afterward. The stronger backshifting effects caused by blue shifts suggest that large blue shifts may be less desirable for long-term stability. However, a balanced combination of red and blue shifts can lead to resonance stabilization post-exposure.

3 Application demonstration: bidirectional fine trimming of a demultiplexer

In this section, we demonstrate the benefits of bidirectional refractive index trimming. We adjust the passbands of a wavelength-division multiplexing (WDM) demultiplexer fabricated using SRN with a refractive index of $n_{srn} = 2.9$ (at 1550 nm). This example illustrates that a passband can be trimmed with the accuracy of about 10 pm, proving the effectiveness of the approach.

Fig. 3.5a presents a microscopic image of the WDM demultiplexer used in practical trimming experiments. In addition, Fig. 3.5b shows a magnified image of an MRR that was trimmed. The ring was made of four straight sections connected by four arcs with the radius of 25 μm. The straight sections at the couplers' sides had the length of 16 μm, while the length of the other two straight sections was 10 μm. In total, the length of the ring was about 209 μm.

Fig. 3.5c and Fig. 3.5d show the transfer characteristics of the WDM demultiplexer at a through port and one of drop ports, respectively, before and after trimming with a 405 nm laser. The objective of the trimming process was to set the passbands of the demultiplexer at 1550 nm, 1549.25 nm, and 1548.5 nm such that they are separated by 750 pm. Based on Fig. 3.5c and Fig. 3.5d, we achieved the trimming accuracy of about 10 pm. Indeed, the final resonances' positions were 1548.508 nm, 1549.248 nm, and 1549.988 nm, which means they were away from the targets by 8 pm, 2 pm, and 12 pm, respectively. Notably, the trimming technique enabled both red and blue shifts of resonances, providing a versatile method for fine-tuning the device's filtering properties. The switching of the direction and the rate of resonance shifting was enabled by changing the laser's power.

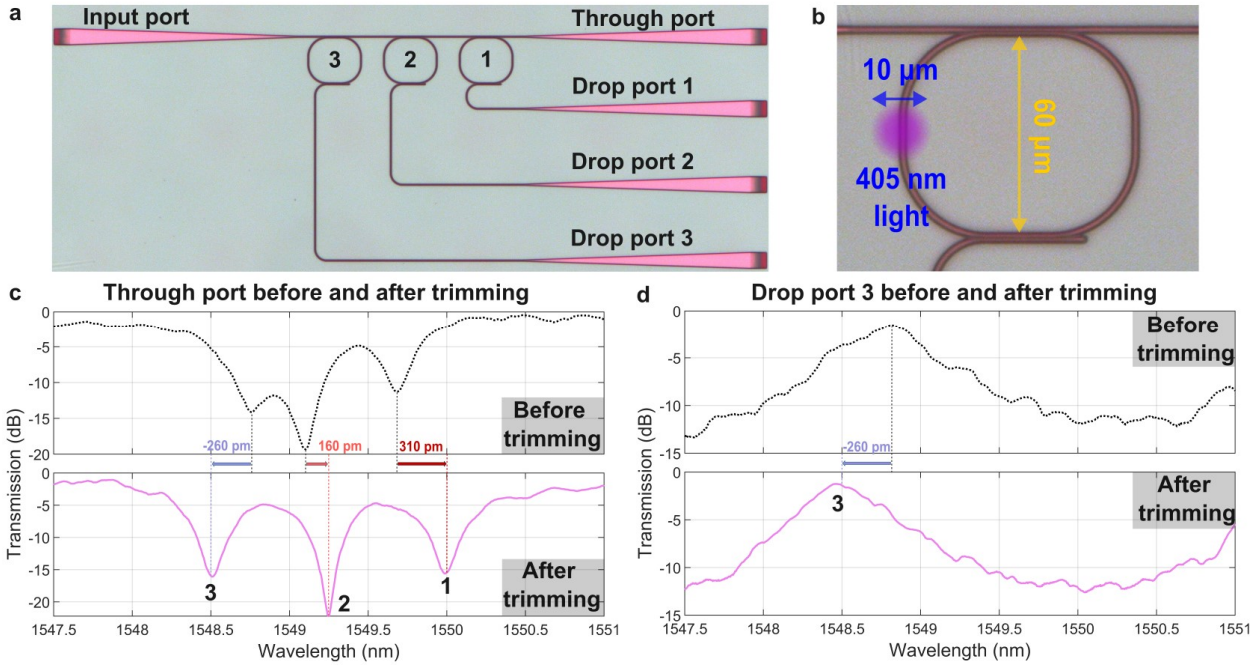

Figure 3.5: (a) Microscope image of demultiplexer. (b) Magnified microscope image of an MRR. Transmission of the probing signal in SRN MRRs as a function of the wavelength for (c) through port and (d) drop port 3. The values above the arrows represent resonance shifts necessary for trimming to achieve the target. The numbers 1,2,3 represent each ring from Fig. 3.5a.

Here we highlight the importance of bidirectional shifting. Indeed, the initial position of the resonance "3" (from Fig. 3.5c) needed to be blue-shifted by 260 pm, while the position of the resonance "2" – red-shifted by only 160 pm, and finally, a stronger red shift of 310 pm was needed for the resonance "1". If only blue shift was available, the resonances "1" and "2" would need to be blue-shifted by $FSR - \Delta\lambda_{red}$, where $\Delta\lambda_{red}$ is the resonance red shift needed. Given that typical FSR is in a range between 1 nm and 5 nm, that would require a much stronger blue shift from 850 pm to 4850 pm for the resonance "1". A large shift is undesirable since it will lead to stronger backshifting and increased losses.

Thus, the results confirm that the trimming approach is suitable for sophisticated photonic devices, providing the necessary precision for fine-tuning passbands in WDM applications. By leveraging the bidirectional trimming method, we can achieve enhanced performance in SRN-based integrated photonic systems.

4 Discussion

Our study demonstrates the remarkable potential of SRN as a reconfigurable photonics platform, offering unprecedented control over the refractive index through visible light trimming. The ability to achieve bidirectional resonance shifts, both blue and red, with a single laser source represents a significant advancement over most existing trimming methods, which are largely limited to unidirectional index changes. This capability opens new possibilities for dynamic tuning of phase-sensitive devices.

The observed resonance shifts, reaching up to 10.6 nm for blue shifts and a record-setting 49.1 nm for red shifts, underscore SRN's scalability and versatility across diverse photonic applications. These shifts correspond to refractive index changes of approximately -2×10^{-2} and 0.11, respectively, which are not only substantial but also finely tunable through adjustments in laser power and exposure duration. This tunability addresses a critical limitation in photonic device manufacturing by providing a means to precisely control device performance post-fabrication, effectively compensating for inherent variations.

Moreover, the coexistence of red and blue shifts provides an additional benefit: significantly reduced trimming backshifting over time, thus contributing to the long-term stability of the trimmed devices. This stabilization is particularly valuable for photonic devices where phase accuracy is critical, such as in WDM systems and other high-performance optical networks.

Our results also highlight the cost-effectiveness of this trimming approach. Unlike alternative methods that often require CMOS-incompatible materials, or expensive trimming methods, our approach uses widely available equipment and CMOS-compatible materials, positioning it as a practical solution for scaled up and industrial applications.

Additionally, the bidirectional shifting in SRN arises from its thermal annealing properties. We established that at lower annealing temperatures (400 °C – 500 °C), the refractive index decreases, while above 500 °C – 600 °C, it increases. This behavior aligns with trimming trends, where lower power induces blue shifts and higher power causes red shifts. Additionally, refractive index reduction is more pronounced in higher-index SRN during rapid thermal annealing, matching observations in trimming, where higher-

index SRN undergoes larger blue shifts. These findings suggest that trimming behavior can be effectively predicted by annealing SRN thin films at different temperatures and measuring refractive index changes, which is a much faster and cheaper alternative to fabricating SRN waveguides.

It is widely recognized that rapid thermal annealing (RTA) of SRN at high temperatures (typically >600 °C) leads to the dissociation of Si-H bonds, significant hydrogen (H) desorption, reduced nitrogen (N) content, and an increased concentration of Si-Si bonds[38-40]. Conversely, studies have shown that RTA at lower temperatures (<600 °C) causes bond redistribution (e.g., Si-Si, Si-N, Si-H, N-H), leading to an increase in Si-H and Si-N bond concentration at the expense of N-H and Si-Si bond concentration[38,39]. In our study, we also observed a noticeable change in behavior when RTA temperatures exceeded 600 °C. Based on these findings, we hypothesize that the refractive index reduction at <600 °C is due to bond redistribution which results in increased Si-H and Si-N bond formation, while the refractive index increase at >600 °C results from significant H desorption due to Si-H bond dissociation, and nitrogen reduction.

While both 405 nm and 520 nm lasers enable bidirectional trimming as both wavelengths are absorbed by SRN, generating heat, it is important to acknowledge that 520 nm light is preferred for index 2.9 SRN bidirectional trimming since it causes a stronger blue shift. It was demonstrated that this is due to lower absorption resulting in lower temperature gradient, which was proven to favor blue shift. Meanwhile, in SRN with a refractive index of 2.4, red shifts are noticeably smaller under 520 nm exposure due to its much lower absorption (extinction coefficients are 0.44 for 405 nm and 0.08 for 520 nm), resulting in less heating, so 405 nm light trimming is preferred.

Finally, we identify new applications for SRN in integrated photonics. For example, SRN shows promise as a CMOS-compatible coating for silicon-on-insulator (SOI) platforms, enabling bidirectional tuning through visible light exposure. Its capacity for a significant refractive index increase also suggests potential for creating etch-free SRN waveguides using visible light, which could reduce fabrication costs and minimize scattering losses due to the absence of etched sidewalls.

In conclusion, this work establishes visible light trimming of SRN as a powerful, flexible tool for photonic device optimization. The demonstrated bidirectional tuning capability, coupled with its precision, cost-effectiveness, and stability, positions SRN as a key material for the next generation of integrated photonics. Future research should explore extending this technique to other photonic architectures, potentially broadening the range of applications and further refining the precision and scalability of SRN-based devices.

5 Materials and methods

5.1 Fabrication process

The fabrication process of PECVD SRN MRRs began with the removal of the silicon device layer from silicon-on-insulator (SOI) substrates using tetramethylammonium hydroxide (TMAH) wet etching, leaving only a 3 μm buried oxide (BOX) layer on top of a 700 μm Si substrate (note that this step can be skipped if Si samples with only SiO_2 layer on top are available). Next, PECVD SRN films were deposited in an Oxford Plasmalab PECVD system at a temperature of 350 °C and a pressure of 650 mTorr. The SiH_4 and N_2 precursor gases were introduced at flow rates of 80 sccm and 800 sccm, respectively, for the 2.4 refractive index film, and 450 sccm and 200 sccm for the 2.9 refractive index film. Following deposition, hydrogen silsesquioxane (HSQ) e-beam resist was spun onto the SRN films, and electron-beam lithography was used to define the waveguide patterns. After developing the HSQ resist, the SRN films were etched in a Plasma-Therm ICP-RIE system, and the HSQ was subsequently removed using a 6:1 buffered oxide etch (BOE) diluted with deionized water in ratio 1:20. Complete removal of the HSQ resist was confirmed by measuring the remaining waveguide thickness with a stylus profilometer. The samples were then clad with a 2 μm PECVD SiO_2 layer, also deposited using the Oxford Plasmalab PECVD system.

Supplementary information for "Large bidirectional refractive index change in silicon-rich nitride via visible light trimming".

S1. Aligning procedure of exposure fiber

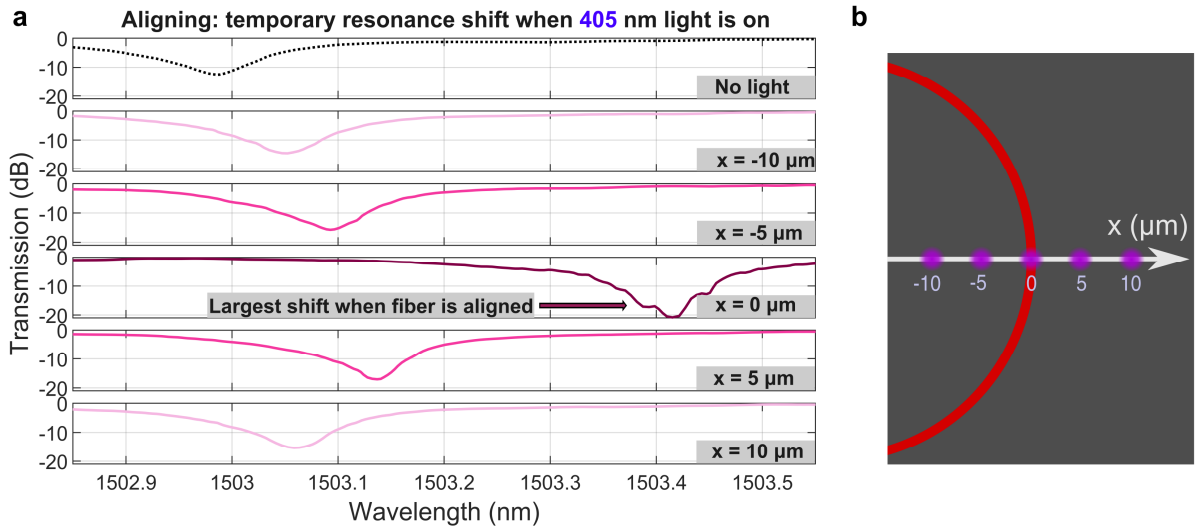

Figure 3.S1: (a) MRR transmission spectra when 405 nm exposing light (8.8 dBm) is off and on, plotted for multiple fiber offsets x. The dotted black curve represents the case when the exposing laser is off. The magenta/pink curves represent the cases when the 405 nm laser is on, and darker tint corresponds to a stronger wavelength shift. When x = 0, the fiber is perfectly centered over a section of the MRR. (b) Section of an MRR showing x-axis and the fiber offsets x from -10 µm to 10 µm used in (e).

Fig. 3.S1a and 3.S1b clarify the aligning process. Specifically, Fig. 3.S1a illustrates how MRR transmission spectrum shifts as the fiber is moved from x = -10 µm to x = 10 µm. Meanwhile, Fig. 3.S1b demonstrates how x-axis is defined. The alignment of the exposing fiber was performed in two steps: coarse alignment using a camera microscope and fine alignment based on the temporary resonance shift caused by light absorption in SRN. The resonance red shift occurred as the fiber approached the MRR, with the maximum shift of 400 pm reached when the fiber was centered over the ring (x = 0 in Fig. 3.S1a and 3.S1b). During alignment, low-power laser exposure was used to minimize permanent trimming, as low powers induce mostly temporary shifts due to heating and free carrier generation. It is worth noting that in practice, before alignment, the probing light was set at the resonance wavelength of the MRR, allowing resonance shifts to be tracked in real-time through changes in optical power. This approach enabled rapid fine alignment even with manual stages.

S2. Resonance shifting due to trimming of a section of an MRR

Fig. 3.S2 exemplifies the measured transmission spectra of the probing signal in SRN MRRs when exposed to 405 nm and 520 nm light. The exposing fiber was centered over a section of the MRR (x = 0), as illustrated in Fig. 3.S1a and Fig. 3.S1b. Only one section of the MRR was exposed.

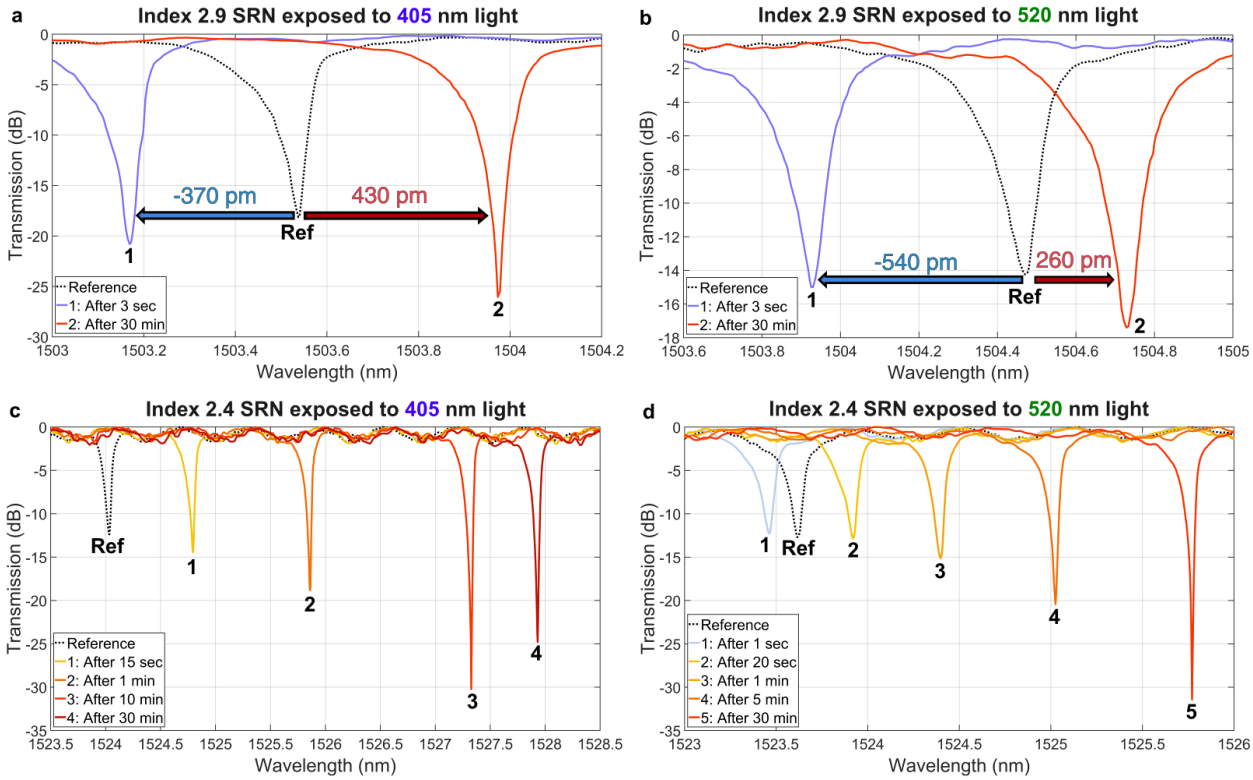

Figure 3.S2: Transmission spectra of the probing signal in SRN MRRs after trimming when (a) n_{srn} = 2.9, λ_{exp} = 405 nm, (b) n_{srn} = 2.9, λ_{exp} = 520 nm, (c) n_{srn} = 2.4, λ_{exp} = 405 nm, (d) n_{srn} = 2.4, λ_{exp} = 520 nm. The dotted black curve indicates the initial position of resonance (reference). The numbers (and "Ref") next to the resonances indicate the order in which the spectra were measured (starting with "Ref"). The labels describe exposure time.

The results in Fig. 3.S2 confirm that it is indeed possible to achieve both red and blue resonance shifts using a single laser source (P_{exp} = 16.0 dBm). A blue shift was observed within a few seconds of exposure in every case except when n_{srn} = 2.4, λ_{exp} = 405 nm (blue shift is still possible at lower power), followed by a reversal of shift direction. In contrast, the red shift took up to 30 minutes to saturate. These results demonstrate the ability to clearly separate blue and red shifts by varying the duration of exposure, a crucial property for trimming applications.

Noticeably, for n_{srn} = 2.4, the red shift was significantly stronger than for n_{srn} = 2.9. Specifically, the red shift was 430 pm for n_{srn} = 2.9, λ_{exp} = 405 nm, but as much as 3900 pm for n_{srn} = 2.4, λ_{exp} = 405 nm. Meanwhile, the strongest blue shift was observed when n_{srn} = 2.9, λ_{exp} = 520 nm.

S3. Thermal annealing as the origin of the bidirectional shifting in SRN MRRs

In this section we demonstrate that thermal annealing is a cause of the bidirectional resonance shifting observed in SRN MRRs. We investigate how temperature of rapid thermal annealing (RTA) affects the refractive index (RI) change of SRN thin film. The refractive index of SRN (n_{srn}) films and their thicknesses are measured by ellipsometer. Fig. 3.S3a presents n_{srn} change as a function of RTA temperature after 2 min of RTA, while Fig. 3.S3b also demonstrates results for 6 min annealing.

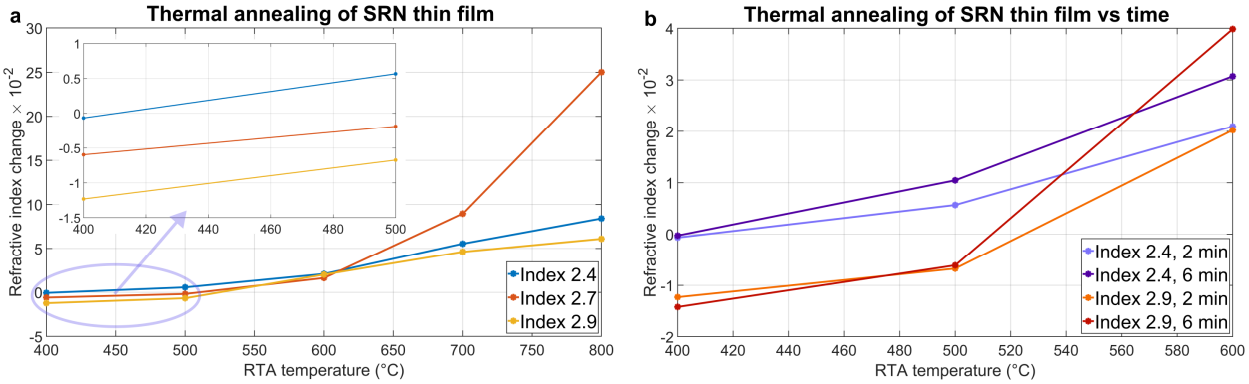

Figure 3.S3: (a) SRN refractive index change as a function of RTA temperature. The inset represents an area of a plot with RTA temperatures in range 400 °C – 500 °C. (b) SRN refractive index change as a function of RTA temperature for different times of RTA.

Based on Fig. 3.S3, it is evident that RTA is a cause of the bidirectional shifting observed in SRN. First, we can see a decline in n_{srn} when annealing is done at lower temperatures. Specifically, the RI reduction is observed at 400 °C RTA for all n_{srn} of 2.4, 2.7, 2.9, and for n_{srn} of 2.7 and 2.9, RI reduces even at 500 °C RTA. Importantly, once RTA temperature exceeds 600 °C, n_{srn} increases in all cases. This matches the behavior of the MRRs resonance shifting, where lower exposure power induces blue shift (due to less heating), while larger power causes a red shift. For example, the RI decrease in n_{srn} = 2.9 due to RTA is 1.4×10^{-2}, which is of the same order compared to the RI decrease measured during trimming experiments (2×10^{-2}). The maximum RI increase of 2.4×10^{-2} during trimming corresponds to RTA at 600 °C and above.

Second, the RI reduction is larger in SRN with a higher n_{srn}, as can be seen from the inset provided in Fig. 3.S3a. This matches perfectly the trend observed during trimming of n_{srn} = 2.4 and n_{srn} = 2.9 SRN, where blue shift was considerably stronger in n_{srn} = 2.9. The RI increase, on the other hand, appears larger in n_{srn} = 2.4, which also agrees well with the trimming results.

In addition, the trend observed from trimming (Fig. 3.2c, Fig. 3.2d) indicates that 520 nm light requires higher power to achieve a strong red shift. This is to be expected since 520 nm light is absorbed less by SRN, which results in less heating. For example, extinction coefficients are 0.44 for 405 nm (penetration depth – 73 nm) and 0.08 (penetration depth – 530 nm) for 520 nm light in n_{srn} = 2.4 SRN, therefore it is expected that 405 nm light should cause stronger red shift. Given that the thickness of index 2.4 SRN waveguides is about 380 nm, we conclude, based on the Beer–Lambert law, that only 50% of all 520 nm light is absorbed (although Si substrate absorbs the rest, causing some extra heating). This explains why 520 nm light requires about 2 dB more power to induce the same RI change (Fig. 3.2d).

S4. On the origin of the bidirectional shifting: exposure power dependence

In this section, we provide a more detailed explanation of the trend observed in Fig. 3.2c. Since the trimming is performed with a laser beam that has a non-uniform power distribution, a temperature gradient is created within a section of an MRR. As a result, different regions of the MRR simultaneously experience both increases and decreases in refractive index during exposure. This effect is particularly pronounced in the index 2.9 SRN, where strong red and blue shifts were observed. Therefore, we focus on this case here.

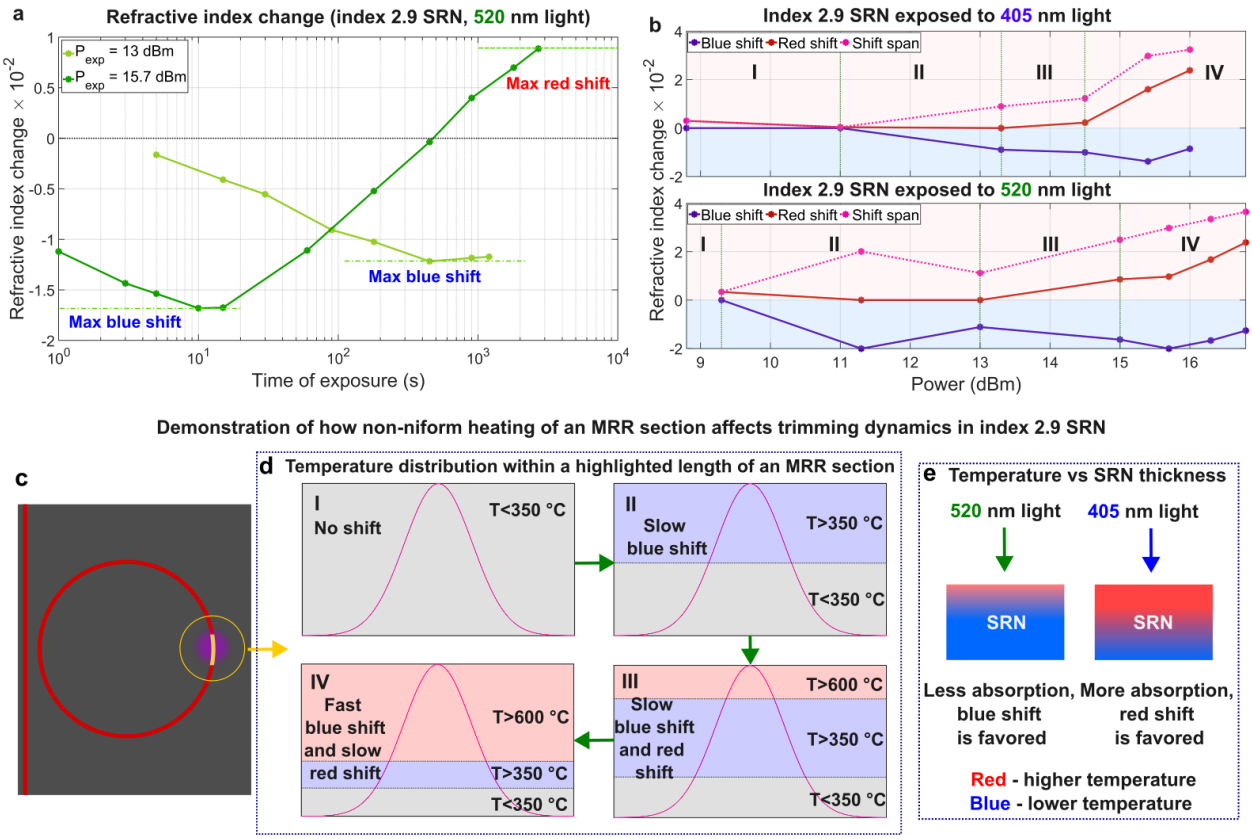

Figure 3.S4: (a) Dynamics of resonance shift in an SRN MRR when $n_{srn} = 2.9$ and $\lambda_{exp} = 520$ nm. (b) Refractive index change of SRN as a function of exposure power when $n_{srn} = 2.9$ (same as Fig. 3.2c, presented here for convenience). (c) Image of an MRR showing how its section is exposed. (d) Demonstration of how non-uniform distribution of heating within an exposed section of an MRR results in different trimming behavior (observed in Fig. 3.S4b). The grey, blue and red areas represent no shift, blue shift and red shift, respectively, due to annealing. The numbers I – IV correspond to cases described in Fig. 3.S4b. (e) Demonstration of how lower absorption of 520 nm light by an SRN waveguide results in larger blue shifts, while higher absorption of 405 nm – in red shifts, for the same level of power.

Fig. S4a shows how the dynamics change at different exposure powers when $n_{srn} = 2.9$ and $\lambda_{exp} =$ 520 nm. Meanwhile, Fig. 3.S4b (identical to Fig. 3.2c, shown here for convenience) depicts the refractive index (RI) change as a function of exposure power for $n_{srn} = 2.9$. To understand the behavior in Fig. 3.S4b, we include Fig. 3.S4c (arc exposure) and Fig. 3.S4d, where we discuss how temperature gradients, caused by non-uniform power distribution, affect trimming.

We start with case I, where power is low enough that even the peak temperature remains below 350 °C (the SRN deposition temperature), resulting in negligible shifts. As power increases in section II, we observe a slower blue shift since parts of the exposed MRR section are heated between 350 °C and 600 °C.

This is illustrated in Fig. 3.S4a, where only a blue shift is observed at P_{exp} = 13 dBm, saturating within 7 minutes (hence we call it 'slow'). In section III, with further power increase, some ring sections reach temperatures above 600 °C, where a red shift dominates, while others remain between 350 °C and 600 °C, where a blue shift persists. This results in bidirectional shifting. However, because both shifts are slow (5 to 30 minutes), they may partially offset each other, reducing the overall trimming range. Finally, in section IV, at the highest power levels, a stronger red shift is observed, though a blue shift is still present. At this stage, most of the ring section reaches temperatures above 600 °C, which intensifies the red shift. Notably, the blue shift dynamics accelerate significantly, with saturation occurring in about 10 seconds (as seen in Fig. 3.S4a for P_{exp} = 15.7 dBm). In contrast, the red shift saturates in about 30 minutes, allowing red and blue shifts to be separated by exposure time, which is essential for bidirectional trimming.

Fig. 3.S4b shows that the blue shift is more pronounced, even at lower exposure powers, when trimming is performed with 520 nm light, while the red shift is more prominent when using 405 nm light. This can be attributed to the higher absorption of 405 nm light by SRN, leading to greater heating and a stronger red shift, as illustrated in Fig. 3.S4e. Specifically, the extinction coefficients are 1.07 and 0.32 for 405 nm and 520 nm light, respectively, resulting in penetration depths of 30 nm and 130 nm, respectively. As light propagates through SRN, power attenuates according to the Beer–Lambert law, creating a temperature gradient. The lower absorption of 520 nm light results in a reduced temperature gradient, which favors blue shifts due to more uniform heating across the SRN waveguide. This uniformity makes it easier for sections of the ring to reach temperatures between 350 °C and 600 °C, where blue shifts are more likely. Fig. 3.S4e emphasizes this effect: with 520 nm light, only a small region at the top of the waveguide undergoes a red shift. However, with 405 nm light, stronger red shifts are seen at the top, and a steeper temperature gradient causes both red and blue shifts to partially offset, reducing the blue shift. In conclusion, 520 nm light is more favorable for bidirectional trimming, as it induces a strong blue shift due to the reduced temperature gradient, while a stronger red shift can be achieved by just increasing exposure power.

S5. Minimizing scattering loss during trimming

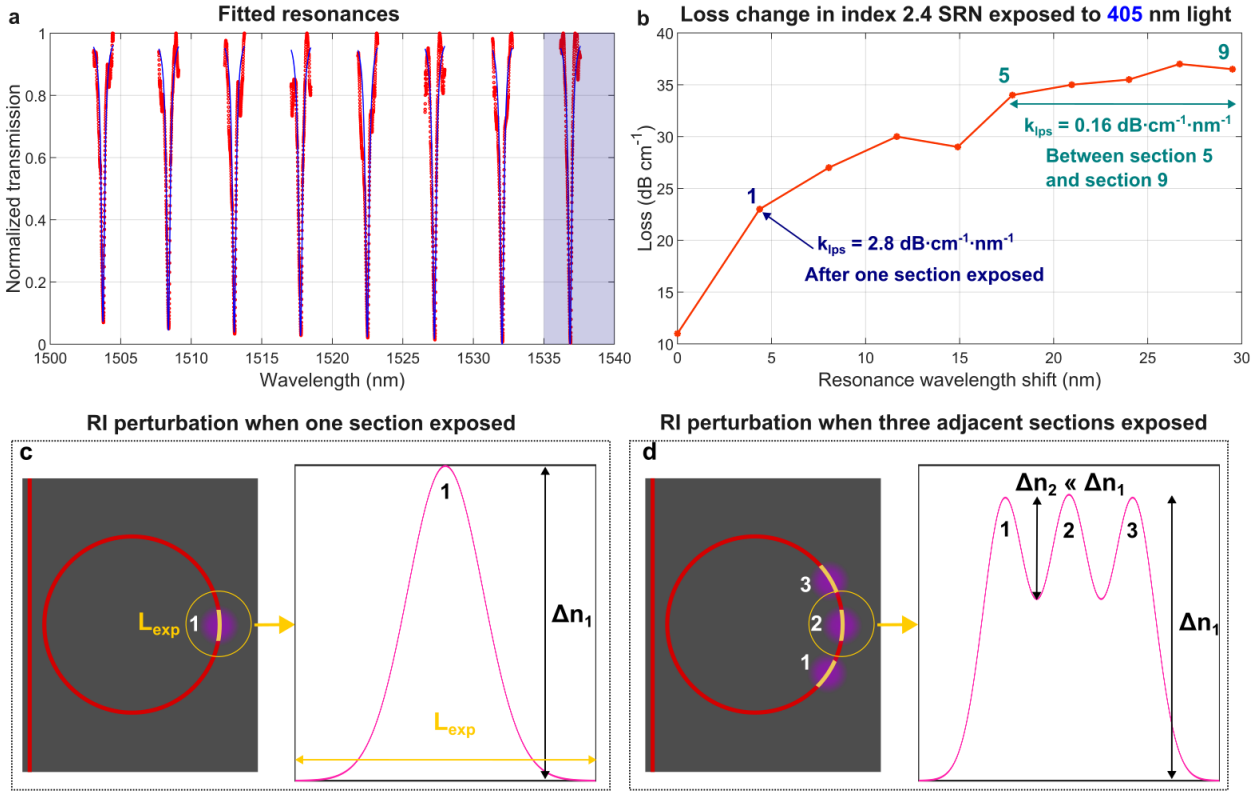

Figure 3.S5: (a) An example of transmission spectrum with fitted resonances of an exposed MRR resonator when n_{srn} = 2.4, λ_{exp} = 405 nm. The blue area denotes the wavelength range where losses were measured. Blue curves represent a fitting function, red circles – measured data. (b) Loss change as a function of shifted resonance wavelength after trimming of an MRR resonator when n_{srn} = 2.4, λ_{exp} = 405 nm (measured in range 1535 nm – 1540 nm). Here numbers mean how many sections of the same MRR were exposed. The parameter k_{lps} is loss per wavelength shift, it determines how much loss increases (in dB cm^{-1}) per 1 nm resonance shift. (c) Illustration of how exposure of one section of an MRR results in RI perturbation Δn_1 responsible for scattering losses. (d) Illustration of how exposure of three adjacent sections of an MRR results in RI perturbation Δn_1 and Δn_2 responsible for scattering losses.

In this section, we examine how different trimming approaches impact scattering losses. Fig. 3.S5a illustrates the process of determining optical losses by fitting MRR resonances. For consistency, all loss measurements were conducted in the wavelength range of 1535 nm – 1540 nm. Fig. 3.S5b shows the increase in scattering losses as a function of the resonance wavelength shift induced by 405 nm light trimming when n_{srn} = 2.4. Each point in this plot represents a different adjacent section of the same MRR exposed to 405 nm light, with a spacing of 17 μm between sections.

Exposure was organized such that the first section (labeled as section 1 in Fig. 3.S5b) was exposed for 45 minutes, the second for 30 minutes, and the remaining sections for 15 minutes each. It is evident that

exposing the first section for 45 minutes led to a considerable increase in scattering losses, as expected: the estimated refractive index (RI) increase was approximately 0.1, changing from 2.4 to 2.5. However, this increase in losses diminished significantly with exposure of the adjacent sections. Indeed, when only the first section was exposed for 45 minutes, the loss increase per wavelength shift, k_{lps}, was 2.8 dB cm^{-1} nm^{-1}. Notably, this value dropped to 0.16 dB cm^{-1} nm^{-1} between sections 5 and 9, indicating that a 1 nm shift would lead to an average increase of only 0.16 dB cm^{-1}, which is acceptable for many applications where expected resonance shifts remain below FSR of an MRR (typically 1 nm – 5 nm). We propose that k_{lps} can be further minimized by exposing the MRR uniformly rather than in discrete steps.

Fig. 3.S5c and 3.S5d clarify how a more uniform exposure reduces scattering losses by decreasing RI perturbations. In this example, closely spaced exposed sections lead to a more uniform RI increase ($\Delta n2 << \Delta n1$), resulting in less scattering. Thus, ensuring uniform exposure of the MRR is essential to mitigate scattering losses, which can otherwise be significantly detrimental, as demonstrated in this section.

S6. Negligible contribution to trimming from PECVD SiO_2 and remaining HSQ

In this section, we investigate whether PECVD SiO_2 or remaining HSQ can account for the permanent resonance shifts observed in SRN MRRs. To explore this, we fabricated c-Si MRRs (waveguide width: 450 nm, waveguide thickness: 220 nm), as shown in Fig. 3.S6a, and exposed one section of the MRR to 520 nm light (Fig. 3.S6b). The fabrication process followed the same flow detailed in the Methods and materials section, with two exceptions: the Si device layer was not removed, and SRN was not deposited. The primary objective was to assess whether permanent resonance shifting occurs in the absence of SRN.

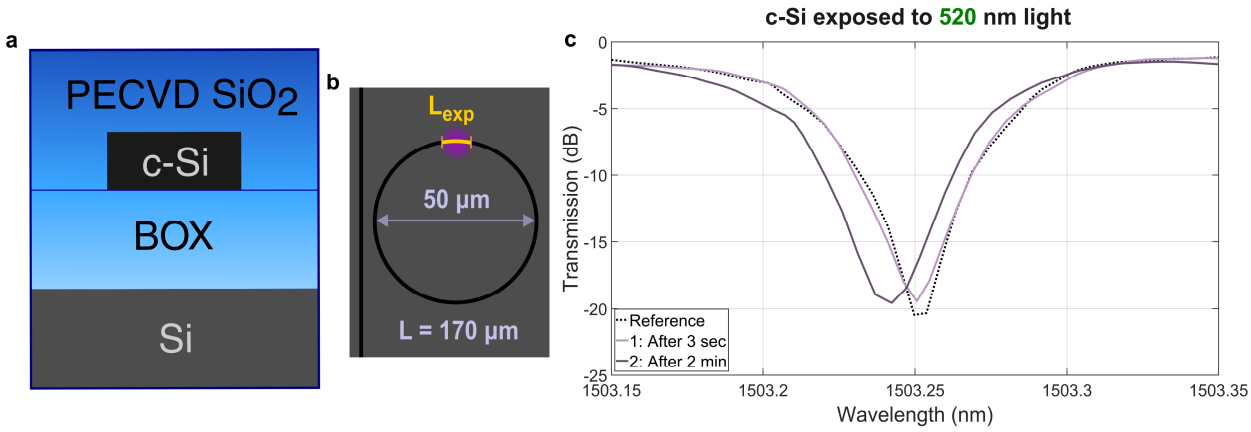

Figure 3.S6: (a) Cross-section of a c-Si waveguide used in experiments. Here BOX is buried oxide. (b) Image of MRR showing how its section is exposed (violet circle), the MRR diameter is 50 µm, and ring length is 170 µm. (c) Transmission spectra of the probing signal in c-Si MRRs after exposure to 520 nm light, P_{exp} = 16.7 dBm. The dotted black curve indicates the initial position of resonance (reference). The labels describe exposure time.

Based on the transmission spectra (Fig. 3.S6c), even after 2 minutes of exposure, the impact on the resonance position is negligible. Specifically, the observed shift of -10 pm is far too small to account for the substantial shifts seen in SRN MRRs. Thus, we conclude that neither PECVD SiO_2 nor residual HSQ contribute to the resonance shifts observed in SRN, regardless of the refractive index.

Acknowledgements

Chapter 3, in part is currently in submission to a peer-reviewed journal. The dissertation author was the first author of this paper, with co-authors Md Masudur Rahman, Karl Johnson, Vladimir Fedorov, Nikola Alic, Abdoulaye Ndao, Paul K. L. Yu, and Yeshaiahu Fainman.

References for Chapter 1

[1] A. Frigg, A. Boes, G. Ren, I. Abdo, D.-Y. Choi, S. Gees, A. Mitchell, Opt. Express 2019, 27, 26 37795.

[2] J. F. Bauters, M. J. R. Heck, D. John, D. Dai, M.-C. Tien, J. S. Barton, A. Leinse, R. G. Heideman, D. J. Blumenthal, J. E. Bowers, Opt. Express 2011, 19, 4 3163.

[3] X. Ji, F. A. S. Barbosa, S. P. Roberts, A. Dutt, J. Cardenas, Y. Okawachi, A. Bryant, A. L. Gaeta, M. Lipson, Optica 2017, 4, 6 619.

[4] K. J. A. Ooi, D. K. T. Ng, T. Wang, A. K. L. Chee, S. K. Ng, Q. Wang, L. K. Ang, A. M. Agarwal, L. C. Kimerling, D. T. H. Tan, Nature Communications 2017, 8, 1 13878.

[5] D. T. H. Tan, K. J. A. Ooi, D. K. T. Ng, Photon. Res. 2018, 6, 5 B50.

[6] B.-U. Sohn, J. W. Choi, D. K. T. Ng, D. T. H. Tan, Scientific Reports 2019, 9, 1 10364.

[7] R. Soref, Nature Photonics 2010, 4, 8 495.

[8] L. Zhang, Y. Li, Y. Hou, Y. Wang, M. Tao, B. Chen, Q. Na, Y. Li, Z. Zhi, X. Liu, X. Li, F. Gao, X. Luo, G.-Q. Lo, J. Song, Opt. Express 2021, 29, 19 29755.

[9] Y. R. Shen, Nature 1989, 337, 6207 519.

[10] M. W. Puckett, R. Sharma, H.-H. Lin, M. han Yang, F. Vallini, Y. Fainman, Opt. Express 2016, 24, 15 16923.

[11] M. A. Porcel, J. Mak, C. Taballione, V. K. Schermerhorn, J. P. Epping, P. J. van der Slot, K.-J. Boller, Opt. Express 2017, 25, 26 33143.

[12] T. Ning, H. Pietarinen, O. Hyvärinen, R. Kumar, T. Kaplas, M. Kauranen, G. Genty, Opt. Lett. 2012, 37, 20 4269.

[13] J. S. Levy, M. A. Foster, A. L. Gaeta, M. Lipson, Opt. Express 2011, 19, 12 11415.

[14] Y. Zhang, J. Nauriyal, M. Song, M. G. Baez, X. He, T. Macdonald, J. Cardenas, Opt. Mater. Express 2023, 13, 1 237.

[15] D. D. Hickstein, D. R. Carlson, H. Mundoor, J. B. Khurgin, K. Srinivasan, D. Westly, A. Kowligy, I. I. Smalyukh, S. A. Diddams, S. B. Papp, Nature Photonics 2019, 13, 7 494.

[16] E. Nitiss, O. Yakar, A. Stroganov, C.-S. Brès, Opt. Lett. 2020, 45, 7 1958.

[17] E. Nitiss, T. Liu, D. Grassani, M. Pfeiffer, T. J. Kippenberg, C.-S. Brès, ACS Photonics 2020, 7, 1 147.

[18] D. Grassani, M. H. P. Pfeiffer, T. J. Kippenberg, C.-S. Brès, Opt. Lett. 2019, 44, 1 106.

[19] X. Lu, G. Moille, A. Rao, D. A. Westly, K. Srinivasan, Nature Photonics 2021, 15, 2 131.

[20] A. Billat, D. Grassani, M. H. P. Pfeiffer, S. Kharitonov, T. J. Kippenberg, C.-S. Brès, Nature Communications 2017, 8, 1 1016.

[21] A. R. Johnson, A. S. Mayer, A. Klenner, K. Luke, E. S. Lamb, M. R. E. Lamont, C. Joshi, Y. Okawachi, F. W. Wise, M. Lipson, U. Keller, A. L. Gaeta, Opt. Lett. 2015, 40, 21 5117.

[22] M. Ferrera, D. Duchesne, L. Razzari, M. Peccianti, R. Morandotti, P. Cheben, S. Janz, D.-X. Xu, B. E. Little, S. Chu, D. J. Moss, Opt. Express 2009, 17, 16 14098.

[23] K. Luke, Y. Okawachi, M. R. E. Lamont, A. L. Gaeta, M. Lipson, Opt. Lett. 2015, 40, 21 4823.

[24] E. Sahin, B. Zabelich, O. Yakar, E. Nitiss, J. Liu, R. N. Wang, T. J. Kippenberg, C.-S. Brès, Nanophotonics 2021, 10, 7 1923.

[25] B. Zabelich, C. Lafforgue, E. Nitiss, A. Stroganov, C.-S. Brès, APL Photonics 2024, 9, 1 016101.

[26] N. K. Hon, R. Soref, B. Jalali, Journal of Applied Physics 2011, 110, 1 011301.

[27] K. Ikeda, R. E. Saperstein, N. Alic, Y. Fainman, Opt. Express 2008, 16, 17 12987.

[28] C. Lacava, S. Stankovic, A. Z. Khokhar, T. D. Bucio, F. Y. Gardes, G. T. Reed, D. J. Richardson, P. Petropoulos, Scientific Reports 2017, 7, 1 22.

[29] Y. Cao, B.-U. Sohn, H. Gao, P. Xing, G. F. R. Chen, D. K. T. Ng, D. T. H. Tan, Scientific Reports 2022, 12, 1 9487.

[30] C. Lacava, T. D. Bucio, A. Z. Khokhar, P. Horak, Y. Jung, F. Y. Gardes, D. J. Richardson, P. Petropoulos, F. Parmigiani, Photon. Res. 2019, 7, 6 615.

[31] A. Friedman, H. Nejadriahi, R. Sharma, Y. Fainman, Opt. Lett. 2021, 46, 17 4236.

[32] X. X. Chia, G. F. R. Chen, Y. Cao, P. Xing, H. Gao, D. K. T. Ng, D. T. H. Tan, Scientific Reports 2022, 12, 1 12697.

[33] X. X. Chia, D. T. H. Tan, Nanophotonics 2023, 12, 8 1613.

[34] H. Kim, J. Aziz, V. D. Chavan, D. kee Kim, Current Applied Physics 2024, 57 59.

[35] F. Martini, A. Politi, Applied Physics Letters 2018, 112, 25 251110.

[36] R. Marchetti, C. Lacava, A. Khokhar, X. Chen, I. Cristiani, D. J. Richardson, G. T. Reed, P. Petropoulos, P. Minzioni, Scientific Reports 2017, 7, 1 16670.

[37] T. Wang, D. K. T. Ng, S.-K. Ng, Y.-T. Toh, A. K. L. Chee, G. F. R. Chen, Q. Wang, D. T. H. Tan, Laser & Photonics Reviews 2015, 9, 5 498.

[38] E. A. Douglas, P. Mahony, A. Starbuck, A. Pomerene, D. C. Trotter, C. T. DeRose, Opt. Mater. Express 2016, 6, 9 2892.

[39] S. C. Mao, S. H. Tao, Y. L. Xu, X. W. Sun, M. B. Yu, G. Q. Lo, D. L. Kwong, Opt. Express 2008, 16, 25 20809.

References for Chapter 2

[1] D. Belogolovskii, N. Alic, A. Grieco, Y. Fainman, Advanced Photonics Research 2024, 2400017.

[2] K. J. A. Ooi, D. K. T. Ng, T. Wang, A. K. L. Chee, S. K. Ng, Q. Wang, L. K. Ang, A. M. Agarwal, L. C. Kimerling, D. T. H. Tan, Nature Communications 2017, 8, 1 13878.

[3] D. T. H. Tan, K. J. A. Ooi, D. K. T. Ng, Photon. Res. 2018, 6, 5 B50.

[4] J. W. Choi, G. F. R. Chen, D. K. T. Ng, K. J. A. Ooi, D. T. H. Tan, Scientific Reports 2016, 6, 1 27120.

[5] Y. Cao, B.-U. Sohn, H. Gao, P. Xing, G. F. R. Chen, D. K. T. Ng, D. T. H. Tan, Scientific Reports 2022, 12, 1 9487.

[6] T. Wang, D. K. T. Ng, S.-K. Ng, Y.-T. Toh, A. K. L. Chee, G. F. R. Chen, Q. Wang, D. T. H. Tan, Laser & Photonics Reviews 2015, 9, 5 498.

[7] A. Friedman, H. Nejadriahi, R. Sharma, Y. Fainman, Opt. Lett. 2021, 46, 17 4236.

[8] G.-R. Lin, S.-P. Su, C.-L. Wu, Y.-H. Lin, B.-J. Huang, H.-Y. Wang, C.-T. Tsai, C.-I. Wu, Y.-C. Chi, Scientific Reports 2015, 5, 1 9611.

[9] C. Lacava, T. D. Bucio, A. Z. Khokhar, P. Horak, Y. Jung, F. Y. Gardes, D. J. Richardson, P. Petropoulos, F. Parmigiani, Photon. Res. 2019, 7, 6 615.

[10] H.-H. Lin, R. Sharma, A. Friedman, B. Cromey, F. Vallini, M. Puckett, K. Kieu, Y. Fainman, APL Photonics 2019, 4 036101.

[11] E. Timurdogan, C. V. Poulton, M. J. Byrd, M. R. Watts, Nature Photonics 2017, 11, 3 200.

[12] J. Peltier, W. Zhang, L. Virot, C. Lafforgue, L. Deniel, D. Marris-Morini, G. Aubin, F. Amar, D. Tran, X. Yan, C. G. Littlejohns, C. Alonso-Ramos, K. Li, D. J. Thomson, G. Reed, L. Vivien, Photon. Res. 2024, 12, 1 51.

[13] B. Zabelich, C. Lafforgue, E. Nitiss, A. Stroganov, C.-S. Brès, APL Photonics 2024, 9, 1 016101.

[14] H. Nejadriahi, A. Friedman, R. Sharma, S. Pappert, Y. Fainman, P. Yu, Opt. Express 2020, 28, 17 24951.

[15] A. Friedman, D. Belogolovskii, A. Grieco, Y. Fainman, Opt. Express 2022, 30, 25 45340.

[16] H. Nejadriahi, S. Pappert, Y. Fainman, P. Yu, Opt. Lett. 2021, 46, 18 4646.

[17] H. Nejadriahi, P. Gaur, K. Johnson, S. Pappert, Y. Fainman, P. Yu, Opt. Lett. 2023, 48, 3 807.

[18] C. Lacava, S. Stankovic, A. Z. Khokhar, T. D. Bucio, F. Y. Gardes, G. T. Reed, D. J. Richardson, P. Petropoulos, Scientific Reports 2017, 7, 1 22.

[19] B.-U. Sohn, J. W. Choi, D. K. T. Ng, D. T. H. Tan, Scientific Reports 2019, 9, 1 10364.

[20] N. Wright, D. Thomson, K. Litvinenko, W. Headley, A. Smith, A. Knights, J. Deane, F. Gardes, G. Mashanovich, R. Gwilliam, G. Reed, Opt. Express 2008, 16, 24 19779.

[21] C.-W. Chen, L. V. Nguyen, K. Wisal, S. Wei, S. C. Warren-Smith, O. Henderson-Sapir, E. P. Schartner, P. Ahmadi, H. Ebendorff-Heidepriem, A. D. Stone, D. J. Ottaway, H. Cao, Nature Communications 2023, 14, 1 7343.

[22] C. Wolff, M. J. A. Smith, B. Stiller, C. G. Poulton, J. Opt. Soc. Am. B 2021, 38, 4 1243.

[23] R. Claps, D. Dimitropoulos, V. Raghunathan, Y. Han, B. Jalali, Opt. Express 2003, 11, 15 1731.

[24] O. Boyraz, T. Indukuri, B. Jalali, Opt. Express 2004, 12, 5 829.

[25] L. Yin, G. P. Agrawal, Opt. Lett. 2007, 32, 14 2031.

[26] M. Rumi, J. W. Perry, Adv. Opt. Photon. 2010, 2, 4 451.

[27] Y. Zhang, C. Husko, S. Lefrancois, I. H. Rey, T. F. Krauss, J. Schröder, B. J. Eggleton, Opt. Express 2016, 24, 1 443.

[28] R. F. Pierret, Advanced Semiconductor Fundamentals, Prentice Hall, Upper Saddle River, NJ, 2003.

[29] D. Schroder, IEEE Transactions on Electron Devices 1997, 44, 1 160.

[30] A. Blanco-Redondo, D. Eades, J. Li, S. Lefrancois, T. F. Krauss, B. J. Eggleton, C. Husko, Optica 2014, 1, 5 299.

[31] W. He, A. Zakar, T. Roger, I. V. Yurkevich, A. Kaplan, Opt. Lett. 2015, 40, 16 3889.

[32] D. E. Hagan, M. Nedeljkovic, W. Cao, D. J. Thomson, G. Z. Mashanovich, A. P. Knights, Opt. Express 2019, 27, 1 166.

[33] D. Navarro-Urrios, A. Pitanti, N. Daldosso, F. Gourbilleau, R. Rizk, G. Pucker, L. Pavesi, Applied Physics Letters 2008, 92, 5 051101.

[34] M. Novarese, S. Romero-Garcia, J. Bovington, M. Gioannini, IEEE Photonics Technology Letters 2023, 35, 8 450.

[35] B. Davidson, G. Lucovsky, G. Parsons, R. Nemanich, A. Esser, K. Seibert, H. Kurz, Journal of Non-Crystalline Solids 1989, 114 579, proceedings of the Thirteenth International Conference on

Amorphous and Liquid Semiconductors.

[36] A. C. Turner-Foster, M. A. Foster, J. S. Levy, C. B. Poitras, R. Salem, A. L. Gaeta, M. Lipson, Opt. Express 2010, 18, 4 3582.

[37] A. Gil-Molina, I. Aldaya, J. L. Pita, L. H. Gabrielli, H. L. Fragnito, P. Dainese, Applied Physics Letters 2018, 112, 25 251104.

[38] H. Kim, J. Aziz, V. D. Chavan, D. kee Kim, Current Applied Physics 2024, 57 59.

[39] K. Andersen, W. Svendsen, T. Stimpel-Lindner, T. Sulima, H. Baumgärtner, Applied Surface Science 2005, 243, 1 401.

[40] E. S. Andrés, A. del Prado, F. L. Martínez, I. Mártil, D. Bravo, F. J. López, Journal of Applied Physics 2000, 87, 3 1187.

[41] R. Marchetti, C. Lacava, A. Khokhar, X. Chen, I. Cristiani, D. J. Richardson, G. T. Reed, P. Petropoulos, P. Minzioni, Scientific Reports 2017, 7, 1 16670.

[42] S. Habermehl, R. T. Apodaca, R. J. Kaplar, Applied Physics Letters 2009, 94, 1 012905.

[43] C. Ying, T. Ma, L. Xu, M. Rahmani, Nanomaterials 2022, 12, 14.

[44] W. S. Lau, S. J. Fonash, J. Kanicki, Journal of Applied Physics 1989, 66, 6 2765.

References for Chapter 3

[1] Belogolovskii, D., Alic, N., Grieco, A. & Fainman, Y. Silicon-Rich Nitride Refractive Index as a Degree of Freedom to Maximize Nonlinear Wave Mixing in Nanowaveguides. Adv. Photonics Res. 5, 2400017 (2024).

[2] Tan, D. T. H., Ng, D. K. T., Choi, J. W., Sahin, E., Sohn, B.-U., Chen, G. F. R., Xing, P., Gao, H., & Cao, Y. Nonlinear optics in ultra-silicon-rich nitride devices: recent developments and future outlook. Adv. Phys. X 2021, 6, 1.

[3] Belogolovskii, D., Fainman, Y. & Alic, N. Dynamics of Nonlinear Optical Losses in Silicon-Rich Nitride Nano-Waveguides. Adv. Opt. Mater. 2024, 2401299 (2024).

[4] Nejadriahi, H., Friedman, A., Sharma, R., Pappert, S., Fainman, Y. & Yu, P. Thermo-optic properties of silicon-rich silicon nitride for on-chip applications. Opt. Express 28, 24951–24960 (2020).

[5] Ooi, K. J. A., Ng, D. K. T., Wang, T., Chee, A. K. L., Ng, S. K., Wang, Q., Ang, L. K., Agarwal, A. M., Kimerling, L. C. & Tan, D. T. H. Pushing the limits of CMOS optical parametric amplifiers with USRN:Si7N3 above the two-photon absorption edge. Nat. Commun. 2017, 8, 13878.

[6] Friedman, A., Nejadriahi, H., Sharma, R. & Fainman, Y. Demonstration of the DC-Kerr effect in silicon-rich nitride. Opt. Lett. 46, 4236–4239 (2021).

[7] Lin, G.-R., Su, S.-P., Wu, C.-L., Lin, Y.-H., Huang, B.-J., Wang, H.-Y., Tsai, C.-T., Wu, C.-I. & Chi, Y.-C. Si-rich SiNx based Kerr switch enables optical data conversion up to 12 Gbit/s. Sci. Rep. 2015, 5, 9611.

[8] Lin, H. H., Sharma, R., Friedman, A., Cromey, B. M., Vallini, F., Puckett, M. W., Kieu, K. & Fainman, Y. On the observation of dispersion in tunable second-order nonlinearities of silicon-rich nitride thin films. APL Photonics 4, 036101 (2019).

[9] Lacava, C., Dominguez Bucio, T., Khokhar, A. Z., Horak, P., Jung, Y., Gardes, F. Y., Richardson, D. J., Petropoulos, P. & Parmigiani, F. Intermodal frequency generation in silicon-rich silicon nitride waveguides. Photon. Res. 7, 615–621 (2019).

[10] Choi, J. W., Chen, G. F. R., Ng, D. K. T., Ooi, K. J. A. & Tan, D. T. H. Wideband nonlinear spectral broadening in ultra-short ultra-silicon-rich nitride waveguides. Sci. Rep. 2016, 6, 27120.

[11] Friedman, A., Belogolovskii, D., Grieco, A. & Fainman, Y. Optical bistability in PECVD silicon-rich nitride. Opt. Express 30, 45340–45349 (2022).

[12] Nejadriahi, H., Pappert, S., Fainman, Y. & Yu, P. Efficient and compact thermo-optic phase shifter in silicon-rich silicon nitride. Opt. Lett. 46, 4646–4649 (2021).

[13] Lu, Z., Jhoja, J., Klein, J., Wang, X., Liu, A., Flueckiger, J., Pond, J. & Chrostowski, L. Performance prediction for silicon photonics integrated circuits with layout-dependent correlated manufacturing variability. Opt. Express 25, 9712–9733 (2017).

[14] Boning, D. S., El-Henawy, S. I. & Zhang, Z. Variation-aware methods and models for silicon photonic design-for-manufacturability. J. Lightwave Technol. 40, 1776–1783 (2022).

[15] Zortman, W. A., Trotter, D. C. & Watts, M. R. Silicon photonics manufacturing. Opt. Express 18, 23598–23607 (2010).

[16] Hill, K. O., Fujii, Y., Johnson, D. C. & Kawasaki, B. S. Photosensitivity in optical fiber waveguides: application to reflection filter fabrication. Appl. Phys. Lett. 32, 647–649 (1978).

[17] Suzuki, S., Hatakeyama, Y., Kokubun, Y. & Chu, S. T. Precise control of wavelength channel spacing of microring resonator add-drop filter array. J. Lightwave Technol. 20, 745–(2002).

[18] Haeiwa, H., Naganawa, T. & Kokubun, Y. Wide range center wavelength trimming of vertically coupled microring resonator filter by direct UV irradiation to SiN ring core. IEEE Photonics Technol. Lett. 16, 135–137 (2004).

[19] Canciamilla, A., Morichetti, F., Grillanda, S., Velha, P., Sorel, M., Singh, V., Agarwal, A., Kimerling, L. C. & Melloni, A. Photo-induced trimming of chalcogenide-assisted silicon waveguides. Opt. Express 20, 15807–15817 (2012).

[20] Guo, T., Zhang, M., Yin, Y. & Dai, D. A laser-trimming-assist wavelength-alignment technique for silicon microdonut resonators. IEEE Photonics Technol. Lett. 29, 419–422 (2017).

[21] Zheng, J., Khanolkar, A., Xu, P., Colburn, S., Deshmukh, S., Myers, J., Frantz, J., Pop, E., Hendrickson, J., Doylend, J., Boechler, N. & Majumdar, A. GST-on-silicon hybrid nanophotonic integrated circuits: a non-volatile quasi-continuously reprogrammable platform. Opt. Mater. Express 8, 1551–1561 (2018).

[22] Chen, C. J., Zheng, J., Gu, T., McMillan, J. F., Yu, M., Lo, G.-Q., Kwong, D.-L. & Wong, C. W. Selective tuning of high-Q silicon photonic crystal nanocavities via laser-assisted local oxidation. Opt. Express 19, 12480–12489 (2011).

[23] Bachman, D., Chen, Z., Prabhu, A. M., Fedosejevs, R., Tsui, Y. Y. & Van, V. Femtosecond laser tuning of silicon microring resonators. Opt. Lett. 36, 4695–4697 (2011).

[24] Schrauwen, J., Van Thourhout, D. & Baets, R. Trimming of silicon ring resonator by electron beam induced compaction and strain. Opt. Express 16, 3738–3743 (2008).

[25] Prorok, S., Petrov, A. Y., Eich, M., Luo, J. & Jen, A. K.-Y. Trimming of high-Q-factor silicon ring resonators by electron beam bleaching. Opt. Lett. 37, 3114–3116 (2012).

[26] Spector, S., Knecht, J. M. & Juodawlkis, P. W. Localized in situ cladding annealing for post-fabrication trimming of silicon photonic integrated circuits. Opt. Express 24, 5996–6003 (2016).

[27] Hagan, D. E., Torres-Kulik, B. & Knights, A. P. Post-fabrication trimming of silicon ring resonators via integrated annealing. IEEE Photonics Technol. Lett. 31, 1373–1376 (2019).

[28] Yu, X., Chen, X., Milosevic, M. M., Yan, X., Saito, S. & Reed, G. T. Ion implantation and electrical annealing for trimming silicon MZIs and facilitating one-time programmable photonic circuits. IEEE 16th International Conference on Group IV Photonics 2019, 1–2 (2019).

[29] Yu, X., Chen, X., Milosevic, M. M., Yan, X., Saito, S. & Reed, G. T. Electrical annealing for Ge ion-implanted directional couplers. Proc. SPIE 11285, 1128512 (2020).

[30] Jayatilleka, H., Frish, H., Kumar, R., Heck, J., Ma, C., Sakib, M. N., Huang, D. & Rong, H. Post-fabrication trimming of silicon photonic ring resonators at wafer-scale. J. Lightwave Technol. 39, 5083–5088 (2021).

[31] Xie, Y., Frankis, H. C., Bradley, J. D. B. & Knights, A. P. Post-fabrication resonance trimming of Si3_33N4_44 photonic circuits via localized thermal annealing of a sputter-deposited SiO2_22 cladding. Opt. Mater. Express 11, 2401–2412 (2021).

[32] Lambert, S., De Cort, W., Beeckman, J., Neyts, K. & Baets, R. Trimming of silicon-on-insulator ring resonators with a polymerizable liquid crystal cladding. Opt. Lett. 37, 1475–1477 (2012).

[33] Selvaraja, S. K., Rosseel, E., Fernandez, L., Tabat, M., Bogaerts, W., Hautala, J. & Absil, P. SOI thickness uniformity improvement using corrective etching for silicon nano-photonic device. Proc. IEEE Int. Conf. Group IV Photonics 2011, 71–73.

[34] Ackert, J. J., Doylend, J. K., Logan, D. F., Jessop, P. E., Vafaei, R., Chrostowski, L. & Knights, A. P. Defect-mediated resonance shift of silicon-on-insulator racetrack resonators. Opt. Express 19, 11969–11976 (2011).

[35] Lipka, T., Kiepsch, M., Trieu, H. K. & Müller, J. Hydrogenated amorphous silicon photonic device trimming by UV-irradiation. Opt. Express 22, 12122–12132 (2014).

[36] Milosevic, M. M., Chen, X., Cao, W., Runge, A. F. J., Franz, Y., Littlejohns, C. G., Mailis, S., Peacock, A. C., Thomson, D. J. & Reed, G. T. Ion implantation in silicon for trimming the operating wavelength of ring resonators. IEEE J. Sel. Top. Quantum Electron. 2018, 24, 1–7.

[37] De Paoli, G., Jantzen, S. L., Dominguez Bucio, T., Skandalos, I., Holmes, C., Smith, P. G. R., Milosevic, M. M. & Gardes, F. Y. Laser trimming of the operating wavelength of silicon nitride racetrack resonators. Photon. Res. 8, 677–683 (2020).

[38] He, S. S. & Shannon, V. L. Hydrogen diffusion and redistribution in PECVD Si-rich silicon nitride during rapid thermal annealing. *Proc. 4th Int. Conf. Solid-State IC Technol.* 269–271 (1995).

[39] Martínez, F. L., del Prado, A., Mártíl, I., González-Díaz, G., Bohne, W., Fuhs, W., Röhrich, J., Selle, B. & Sieber, I. Molecular models and activation energies for bonding rearrangement in plasma-deposited a−SiNx:H dielectric thin films treated by rapid thermal annealing. *Phys. Rev. B* **2001**, *63*, 245320.

[40] Dani, P., Tuchen, M., Meli, B. E., Franz, J. & Knoch, J. Release of hydrogen gas from PECVD silicon nitride thin films in cavities of MEMS sensors. *Micro Nano Eng.* 2024, 100291 (2024).